History and current processes of the Martian polar layered deposits

Thesis by

Shane Byrne

In Partial Fulfillment of the Requirements

for the Degree of

Doctor of Philosophy

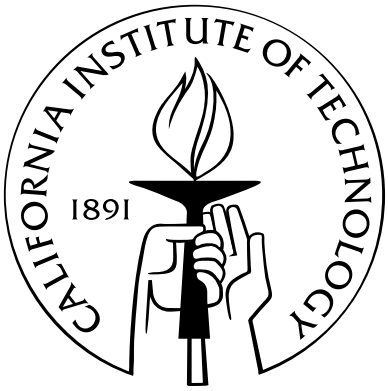

California Institute of Technology

Pasadena, California

2003

(Defended May 27, 2003)

Science is built up of facts, as a house is with stones.

But a collection of facts is no more a science than a heap of stones is a house.

Jules-Henri Poincare

Acknowledgements

I have been incredibly lucky; there is really no other way to describe it. I've been personally lucky to have been surrounded at all times by people who wish only the best for me, and I've been professionally lucky to have walked through the doors of graduate school just as a deluge of fresh data from the planet Mars was arriving after a twenty year drought. There are many people who I owe a great deal to (some of whom I don't even realize how much). I firstly thank my parents, Jerry and Deirdre, who sacrificed a lot because they believed that I should get a first-rate education. I thank them for encouragement and understanding when I decided to go study astrophysics as an undergrad, despite their misgivings about future employment :), I would never have made it half as far were it not for them. My study here at Caltech would not have been possible without the support and love of my wife, Roni, her encouragement kept my spirits up and my cynicism at bay. I am grateful beyond expression for our life together and it is to her that this thesis is dedicated.

Research advice has come from many people. I am especially grateful to Bruce Murray and Andy Ingersoll, my two advisors on the work contained in this thesis. Both of them contributed endlessly with very different advising styles. I am additionally indebted to Bruce for initially getting me interested in Mars. He opened my eyes to a world that I will never be able to turn away from. I want to say a special additional thank you to Andy for his remarkable patience with me while I was endlessly distracted with other things. I also got plenty of advice and learned a lot about things Martian from Mark Richardson. I finally want to thank my undergraduate advisor Michael Edmunds for helping me discover that scientific research was something that I would want to do for the rest of my life.

I received help from many directions while working here. I am very grateful to Anthony Toigo and Antonin Bouchez for IDL programming language help. Latex help came again from Antonin and also Henry Roe. Everything is so much easier when you can speak the local language. I learned an enormous amount about Mars, spacecraft and many other things (I think more than they realize) from former students Anton Ivanov and Ashwin Vasavada. More than anyone else these two people were role models for me. I got plenty of invaluable GIS help and inspiration from Lori Fenton, Joanne Giberson, Tony Soeller and especially Trent Hare of the USGS. Shawn Ewald and Zane Crawford gave me great technical help on a wide variety of problems.

I have had many office mates during my stay here, I overlapped with them anywhere from a few months to almost five years but I gained something from all of them. They are (in order of appearance) Albert Yen, Yuan Tie Lee, Zhiming Kuang, Ben Weiss, Tanja Bosak, Sebastien Lefranc, Damian Kraemer, Dave Camp, Jiafang Xiao, and Shabari Basu. I can only hope that I am not what is responsible for the high turnover of office mates.

The planetary science office staff has helped me in innumerable situations; they are Irma Black, Leticia Calderon, Nora Oshima, Loretta Young and Ulrika Terrones. I certainly cannot imagine life here without them. A huge thank you goes to Michael Black, our system administrator, the stealth hero of Caltech planetary science. He is probably responsible for more research getting done than any other individual here.

Abstract

The Martian polar layered deposits constitute a detailed record of geologically recent environmental conditions. In this thesis I examine processes that have affected this history over timescales ranging from $\approx 10^2$ to $\approx 10^7$ Martian years. To complete the work in this thesis I developed a geographic database of the Martian polar regions to enable comparisons of different datasets spread over different missions.

I report on the discovery of a large sand rich unit underlying the northern polar layered deposits. The presence of this unit suggests there once existed a radically different polar environment where there was no polar cap. A major new question now arises of where that water went during this time period and how the old polar cap (if there was one) was removed.

I describe analysis and modeling of evolving landforms on the southern residual CO_2 cap. This modeling suggests that these landforms are underlain by a water ice layer. THEMIS observations were used to confirm this hypothesis. This limits the size of the residual CO_2 cap reservoir to no more than 5% of the current atmosphere, which puts an important constraint on models of atmospheric evolution. Analysis of the size distribution coupled with this modeling indicates a uniform age for a large group of these features, implying some environmental change on the order of Martian centuries ago.

I examined geomorphologic evidence for flow processes at the margin of the south polar layered deposits. Indications of multiple episodes of previous flow are seen. However much evidence of brittle processes such as faulting, slumping and landsliding is also present. This leads to the conclusion that, during some periods, flow of the layered deposits is incapable of relieving the gravitationally generated stresses within

the ice sheet. The evidence suggests that periods where flow was possible occurred intermittently and were separated by periods in which sublimation-based retreat of the ice dominated.

Contents

List of Figures

List of Acronyms

GIS Geographic Information System

GRS Gamma Ray Spectrometer

IAU International Astronomical Union

L_s Solar longitude, angular measure of season.

MGS Mars Global Surveyor

MOC Mars Orbiter Camera

MOLA Mars Orbiter Laser Altimeter

NPLD Nouth Polar Layered Deposits

SPLD South Polar Layered Deposits

TES Thermal Emission Spectrometer

THEMIS THermal EMission Infrared Spectrometer

Chapter 1

Introduction

1.1 Rationale for studying the Martian polar regions

The Martian polar layered deposits are an enigmatic geologic formation that have excited and motivated generations of planetary scientists. It is likely they contain a historical record that is rivaled in detail and variety only by terrestrial ice and deep sea cores. More than thirty years have passed since *Murray et al.* (1972) first reported the existence of what they termed *"Laminated Terrain"* at the Martian south pole. These polar layered deposits (as they later became known) were first imaged by Mariner 7 (Figure 1.1) and have been studied as part of every Mars orbiting mission since. At the time of their discovery they were immediately seized upon as a possible record of Martian climate (*Cutts*, 1973b; *Ward*, 1973; *Cutts and Lewis*, 1982). These sediments are commonly interpreted as being composed of varying proportions of atmospherically deposited ice and dust. This thesis is focused on using the new MGS (and to a lesser extent Mars Odyssey) data to examine both contemporary processes and the historical record contained within the polar layered deposits.

The opportunity to study what is effectively a summary of the recent history of Mars is too good to pass over. However, it has proven very difficult to extract information from the record that is obviously present in the polar layered deposits. In the last three decades hundreds of papers have been published attempting to

decipher some part of the polar puzzle. Much work has been done on describing the layered deposits, but the overall paradigm of dusty water ice has remained roughly the same. There are several major questions still to be answered: What is their exact composition? Are they currently forming? Do the ice caps flow? What are the details of layer formation? What is the relationship between the northern and southern deposits?

With the advent of the Mars Global Surveyor (MGS) and Mars Odyssey missions there are opportunities for new discoveries and so there has been a new surge of interest in the polar areas. This is in part due to the fortunate polar orbit of the spacecraft which ensures that the volume of data collected over the polar regions is disproportionately large compared to their area.

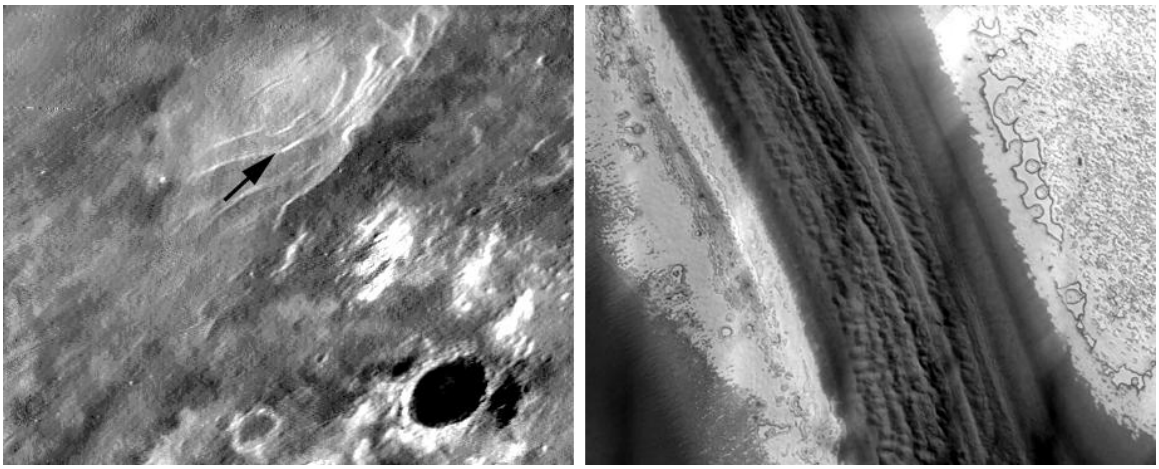

Figure 1.1: The left frame is the first view of the Martian polar layered deposits taken by Mariner 7 (image 17, processing by M. Robertson, Northwestern university) in the summer of 1969. View is looking toward the south pole along the 30°E meridian. The dark crater at the bottom right is 100 km across although the scale changes throughout the image due to the large emission angle. The arrow denotes the position of the right hand image (THEMIS frame V00910003) which was taken in February 2002 and shows that polar scarp in detail. The available data have improved considerably during the last 34 years.

Many polar processes have operated on widely varying timescales throughout Mars' history. Each chapter in this thesis examines processes (and their resultant

history) over a different timescale. All of these processes may be considered *recent* in the broader context of the history of the entire planet, but their timescales are extremely diverse. This introduction provides an overview of the Martian polar layered deposits and describes the contribution my research has made to this picture. In Chapter 2 I detail the discovery of a distinct division within the stratigraphy of the north polar layered deposits. The lower unit was determined to be primarily sand, which differs radically from that of the overlying dust-ice mixture. This indicates that there was a period in Mars' history where there was no northern polar cap. In Chapter 3 I describe modeling of the erosion of the southern residual CO_2 cap by expanding flat floored pits. In this work we accomplished two major things. We placed an upper limit on the size of the solid CO_2 reservoir which rendered it insignificant even compared to the present atmosphere. The other finding is the recognition of a distinct population of these features which were all initiated close together in time. This indicates a changing polar environment on timescales of $\approx 10^2$ years. In Chapter 4 I explore the possibility of a changing polar environment which causes flow processes to start and stop repeatedly. These changes are probably coupled to variations in orbital parameters. These findings of these chapters are summarized in more detail in Section 1.4.

1.2 Description of the Martian polar regions

The south polar region of Mars was first imaged by Mariner 7 (*Sharp et al.*, 1972); however, the layered deposits were first recognized from Mariner 9 imagery by *Murray et al.* (1972). The southern layered deposits have a mapped extent of about $1.3 \times 10^6 \text{km}^2$ (*Tanaka and Scott*, 1987) and sit unconformably on top of the heavily cratered southern highlands. They are capped by a much smaller, $8.8 \times 10^4 \text{km}^2$, (*Thomas et al.*, 1992), residual cap of CO_2 ice. This residual CO_2 deposit is draped over the highest area of the southern layered deposits and is offset from the rotational pole by about 180 km in the direction of 330°E. The layered deposits themselves are not symmetric about the pole and extend much further in the 180°E direction, perhaps

due to melting and asymmetric retreat of a formally larger ice sheet (*Head and Pratt*, 2001).

The northern layered deposits were speculated to exist by *Murray et al.* (1972) based on the relatively poor imagery available in that location from Mariner 9. Confirmation of their layered nature was provided by the Viking mission (*Cutts et al.*, 1976). The northern polar layered deposits are near circular, centered on the pole and roughly 1000 km across. They are almost completely covered by the northern residual cap which is a thin, high albedo, water ice layer (*Kieffer et al.*, 1976). Surrounding the northern polar layered deposits is a large circumpolar sand sea (*Dial*, 1984; *Tanaka and Scott*, 1987) which is the largest continuous sand deposit on the planet.

Topographic data acquired by the MOLA instrument have shown that the layered deposits in both hemispheres are broadly dome shaped (*Smith et al.*, 1999) (Figure 1.2). Although they are at very different elevations, the thickness of both the northern and southern deposits are similar (≈3 km). Both polar deposits have their internal layering exposed in many troughs and scarps (Figure 1.3).

Both polar caps are covered annually by 1-2 meters of seasonal CO_2 frost during their respective winters (*Leighton and Murray*, 1966; *Smith et al.*, 2001a). These seasonal caps extend as far equatorward as 55° N/S (*James et al.*, 1992). The high resolution visual appearance of the layers themselves differ considerably between the northern and southern deposits (Figure 1.3). The southern layers are expressed as staircase topography suggesting differing mechanical properties for each layer. The northern layers more usually outcrop on smooth slopes and differ in albedo. The southern layers appear much more degraded than the northern ones which is consistent with estimates of their ages from crater counting.

The surfaces of both polar layered deposits are extremely smooth at large length scales (*Aharonson et al.*, 2001) but have considerable texture at higher resolution. They are sparsely cratered (*Koutnik et al.*, 2002; *Herkenhoff and Plaut*, 2000) being one of the youngest surfaces on Mars. In particular the surface of the northern polar deposits has almost no impact craters and so is too young to be reliably dated. The

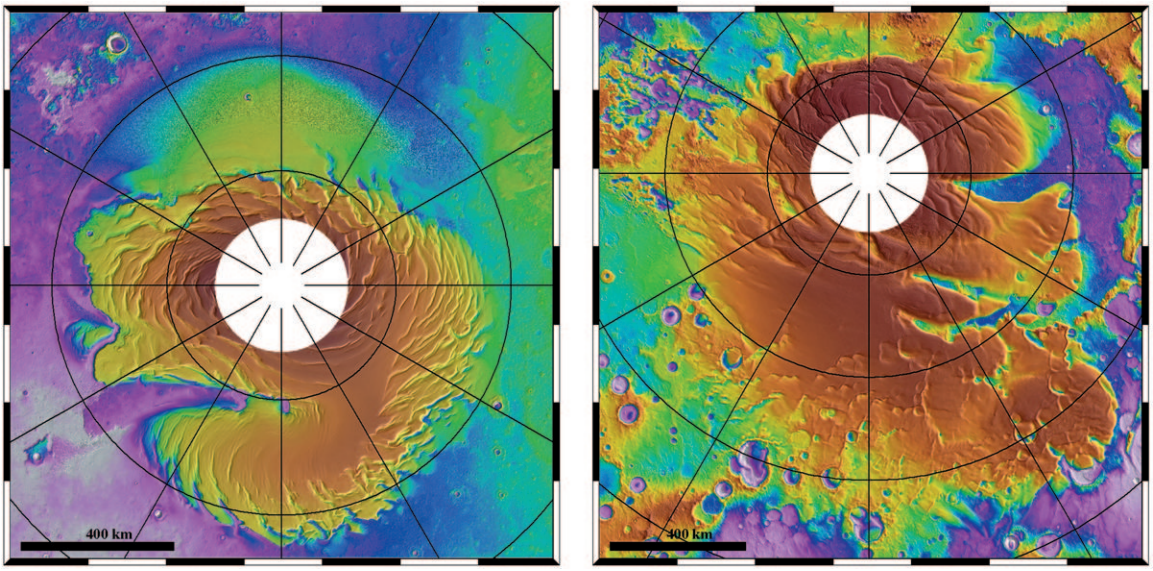

Figure 1.2: Shaded topography in polar stereographic projection of the northern (right) and southern (left) polar layered deposits. The southern deposits cover a larger area, both have similar relief. The color represents elevation but has been stretched in nonlinear way to better show elevation differences. Elevation ranges on the left from -6443 m (purple) to -2261 m (brown), and on the right from -326 m (purple) to 4798 m (brown). Note differing horizontal scales in each frame. Topography data from Greg Neumann of the MOLA team.

most recent crater counts, of impact structures >1 km diameter, on the southern deposits indicate a surface age of 30-100 Myr (*Koutnik et al.*, 2002). These craters exhibit anomalously low depth to diameter ratios (*Koutnik et al.*, 2002) which may be due to differing physics for impacts into ice, or to subsequent blanketing (*Plaut et al.*, 1988; *Herkenhoff and Plaut*, 2000), or to viscous relaxation (*Pathare et al.*, 2003), or to some combination of all three. These craters were also found to still have significant rims indicating that the viscous relaxation mechanism suggested by *Pathare et al.* (2003) is perhaps the most likely explanation for their shallow depths. Interpretation of these crater count data must be handled with some degree of care. In *Koutnik et al.* (2002), we found that a much younger surface age ($\approx 10^5$ years) was suggested by the smaller craters (<500m diameter). Reconciling these ages has proven difficult but the data are consistent with a resurfacing event $\approx 10^5$ years ago which was effective enough to remove all previous craters in the small size range but leave the larger craters (>1 km diameter) intact.

Herkenhoff and Murray (1990a) examined the color and albedo of the southern layered deposits and found that they closely match bright reddish dust seen elsewhere on Mars. They found no significant color or albedo boundary where the layered deposits transition to the southern highlands. *Paige and Keegan* (1994) derived thermal inertias and Lambert albedos for the southern layered deposits and also found no significant change in these properties at the edge of the layered deposits. *Hofstadter and Murray* (1990) showed that any exposed water ice at this location would quickly acquire a protective sublimation lag. Thus it appears from both observations and theory that the southern layered deposits and surrounding highland material are blanketed with at least a few centimeters of fine material which is well consolidated enough to be stable on significant slopes and resist erosion by seasonal winds (*Herkenhoff and Murray*, 1990b; *Vasavada et al.*, 2000).

The size, shape and icy composition of the polar layered deposits are analogous to terrestrial ice sheets such at that found in Greenland which also contains layering. The degree to which the Martian deposits behave like terrestrial ice sheets is still an open question. Much recent debate has centered around the question of whether the

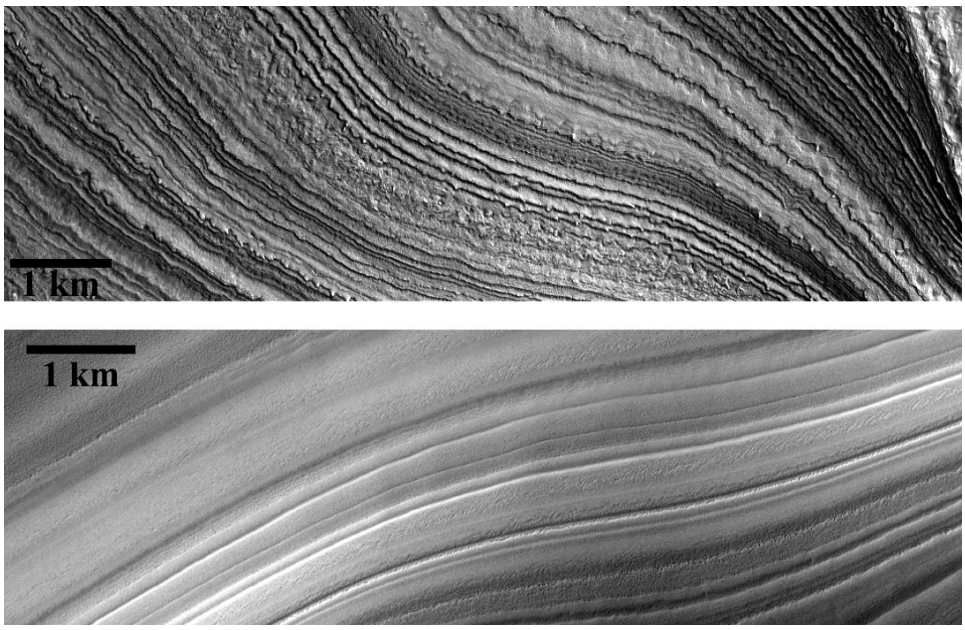

Figure 1.3: Southern (top panel) and northern (bottom panel) layering compared. Layering in the southern polar layered deposits shows staircase topography indicating differing material strengths between layers. In contrast, layering in the north usually outcrops on smooth slopes. Both these scarps are roughly equatorward facing with the downhill direction from top to bottom. Top panel is a subframe of MOC narrow-angle image E11/03053 at 86.2°S, 173°E, L_s 293°, illumination from the upper right. Bottom panel is a subframe of MOC narrow-angle image M18/01897 at 86.2°N, 233°E, L_s 43°, illumination from the lower right.

ice caps (particularly in the north) are currently flowing. The possibility of flow has been proposed by several authors (*Head*, 2001; *Nye*, 2000); conversely brittle fracture and sublimation have been proposed to dominate over flow by others (*Ivanov and Muhleman*, 2000; *Murray et al.*, 2001).

1.3 Tools and data used in this thesis

1.3.1 Mars Global Surveyor and Mars Odyssey

This thesis has been made possible by data from the ongoing *Mars Global Surveyor* and *Mars Odyssey* missions. It has been my good fortune to be at graduate school when data from these missions began to become available. In Appendix C, I discuss the timeline of events during these missions and show when different data have been acquired.

The orbits chosen for the two spacecraft are especially fortunate for polar studies. Both Mars global surveyor and Mars Odyssey are in near polar orbits ($\approx 93^\circ$ inclination) with periods of about 2 hours. This means that they pass over both north and south poles (at a latitude of 87°) 12 times each day, with each pass spaced almost evenly in longitude. A consequence of this orbit is that there is a ring at a latitude of 87° N/S that is extremely well covered (known as the "polar ring" or "3° ring"). It was the blanket coverage of this area by the MOC camera that discovered the Swiss-cheese landforms which are the subject of Chapter 3. The concentration of orbital tracks in the polar regions also made possible the generation of gridded products such as MOLA elevations models and TES albedo maps at a much higher spatial resolution than anywhere else on the planet by at least an order of magnitude. A less welcome consequence is that because all instruments are nadir pointing, the areas between latitudes of 87° and 90° in both hemispheres are not covered at all. To gain some coverage of these areas the spacecraft was rolled to the side as it passes the polar ring; this was rarely done (on $< 1\%$ of orbits).

The studies in this thesis have utilized a variety of instruments, some more heav-

ily than others. For completeness a brief description of the instruments themselves follows.

The Mars Orbiter Camera (*Malin et al.*, 1992; *Malin and Edgett*, 2001) consists of a two wide-angle cameras (one at blue wavelengths and one at red) and a narrow-angle camera. The wide-angle cameras take both daily global images at resolutions of several km/pixel and context images for the narrow-angle frames at resolutions of 230 m/pixel. The narrow-angle camera resolution can range from 1.4 to 12 m/pixel depending on the selected internal editing. All three cameras of MOC are a 'pushb-room' system where data is acquired one line at a time by a single row of pixels. The orbital motion of the spacecraft sweeps this linear CCD array across the observed scene.

The Mars Orbiter Laser Altimeter (MOLA) (*Zuber et al.*, 1992; *Smith et al.*, 2001b) measures time of flight of laser pulses to the surface and back thereby get-ting the range from the spacecraft to the surface. Accurate orbital information is necessary to convert this range measurement to a planetary radius at a specific longi-tude and latitude. Knowledge of the Martian geoid (Aeroid) is necessary to convert this planetary radius to topography. Modeling of data from the radio science exper-iment (*Tyler et al.*, 2001; *Lemoine et al.*, 2001) has provided the orbital information and gravity fields necessary to convert MOLA measurements to topography. MOLA height measurements are extremely accurate in the vertical direction (errors <1m), the positional accuracy of the individual laser shots is accurate to a few 10's of meters due to the crossover correction (*Neumann et al.*, 2001) which is described in more de-tail as part of Appendix A.3. The MOLA laser fires at approximately 10 Hz, making the sample spacing roughly 300m on the ground. The surface size of the laser shot varies somewhat with topography (Mars has ≈30 km of relief) but is about 150m across.

The Thermal Emission Spectrometer (TES) (*Christensen et al.*, 1992, 2001) has six sensors each of which takes a spectra of a 6×3 km patch of the surface every 2 seconds. The spectral resolution can be either 5 or 10 cm^{-1} and the wavelength range covered is roughly $6 \rightarrow 50\ \mu m$. Also part of the TES instrument are a broadband

infrared bolometer and a shortwave radiometer to measure reflected sunlight.

The THermal EMission Infrared Spectrometer (THEMIS) (*Christensen et al.*, 2003) consists of two cameras, infrared (IR) and visible (VIS). The THEMIS IR camera has 10 spectral bands ranging from $6.8 \rightarrow 14.9\ \mu m$ and a spatial resolution of 100 m/pixel. The THEMIS VIS camera has 5 spectral bands ranging from $0.43 \rightarrow 0.86\ \mu m$ and a spatial resolution of 18 m/pixel. Both cameras acquire all their bands simultaneously using a pushbroom method similar to MOC.

1.3.2 Development of Martian Geographic Information Systems and other tools

With so much available data it is possible to look at many problems in a new coordinated way; this however requires a convenient way to co-register different datasets, both to each other and to the actual Martian surface. Geographic information systems are used commonly on the Earth to this end. We began developing such a system here at Caltech, based on the *Arcview* software, originally to support the landing site selection of the Mars Polar Lander mission. We have subsequently improved the accuracy and usefulness of the system. Many of the results discussed in this thesis have only been possible because of our ability to accurately overlay differing datasets. A short discussion of how this system was developed has been included in Appendix A.1. Some examples of the usefulness of this system from studies in which I have played a role are discussed below.

In one such work we mapped a particular landform (informally named 'spiders') in the south polar layered terrain and showed it occurred only in regions that displayed *'cryptic'* behavior. *'Cryptic'* terrain are areas that show evidence that the seasonal frost layer has sintered into a transparent slab and was first documented by *Kieffer et al.* (2000). The transparency of the ice allows the lower albedo substrate to show through. The study necessitated the identification of which terrain was cryptic and thus meant combining albedo and temperature data to find out what areas were simultaneously dark and cold. In addition the MOC narrow-angle images from which

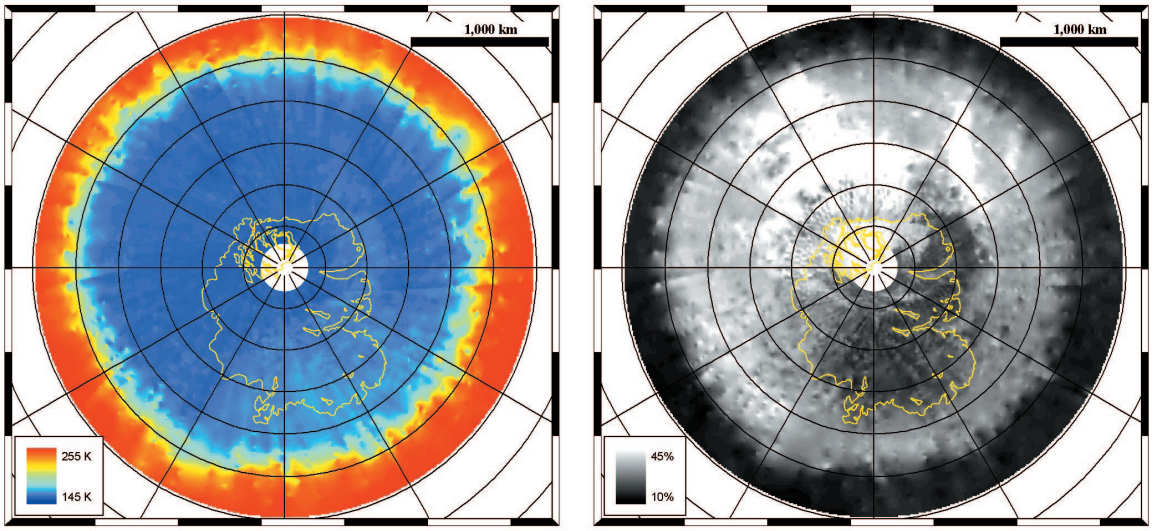

Figure 1.4: Left panel shows TES derived surface temperature (scale in kelvin) at $L_s 215° \rightarrow 220°$ (parallels marked every 5°). Right panel shows visual albedo also derived from the TES instrument for the same time period. Yellow line demarks the edge of the layered deposits (*Tanaka and Scott*, 1987). Areas that are covered in seasonal frost are cold and mostly bright, however there is one *'cryptic'* region that is both dark and cold (*Kieffer et al.*, 2000). The CO_2 ice here is thought to be transparent causing the lower albedo of the underlying material to show through.

we mapped the feature distribution must be well located within the thermal and albedo datasets. An example of the cryptic region at one particular time is shown in Figure 1.4. This work has been published as *Piqueux et al.* (2003).

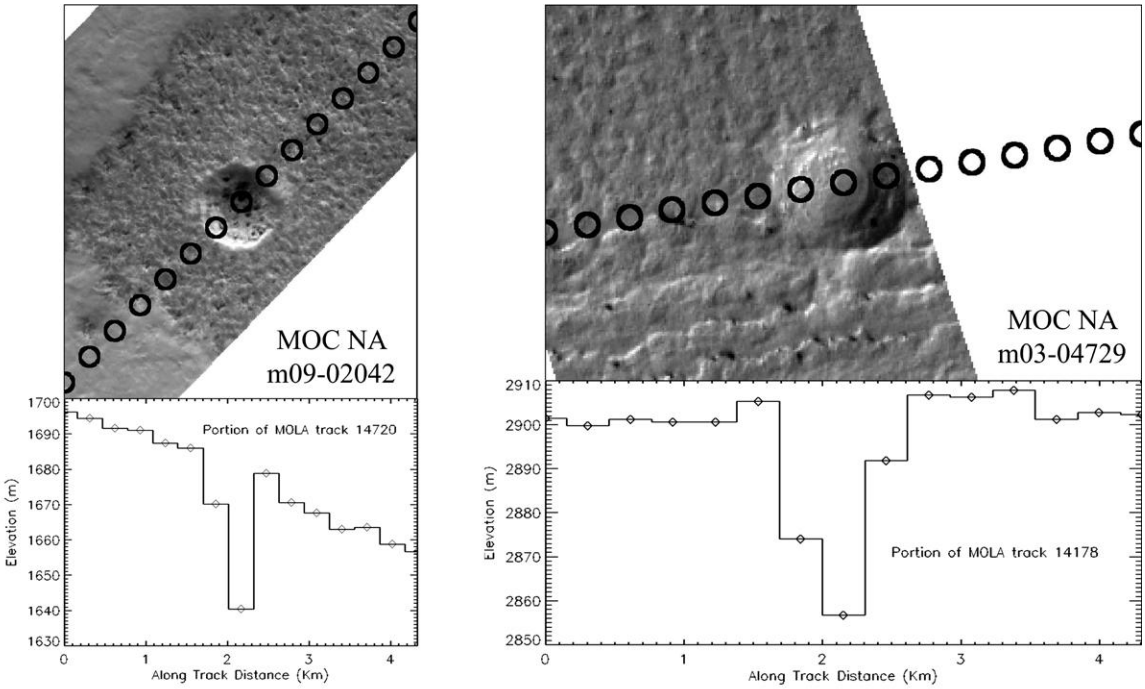

Figure 1.5: Two examples of co-registered MOC and MOLA data (left at 82°S, 67°E, illumination from upper right; right at 86°S, 210°E, illumination from lower right). The circles superposed on the MOC narrow-angle images represent the size and position of individual MOLA laser shots.

In another study utilizing large volumes of co-registered data we conducted crater counts which led to a significant revision of the age of the south polar layered deposits. Part of this study dealt with the analysis of the shape of identified craters from MOLA data. In this case it was necessary to have very accurately registered image data relative to the available topography profiles. Figure 1.5 shows these techniques applied to two particular craters. This work has been published as *Koutnik et al.* (2002).

Prior to this we had developed our own image processing tools to improve the

positioning of MOC narrow-angle images. MOLA data taken simultaneously with a MOC image was used to project and position that MOC image, rather than using traditional techniques that utilize camera pointing angles. This led to an order of magnitude reduction in the positional errors of the MOC narrow-angle images. MOLA data is much more accurately registered to the planet's surface than MOC data due to its crossover correction. Due to its accuracy and quality MOLA data has become the standard which we register all other data to. This process is described in more detail in Appendix A.3.

1.4 The relevance of this work to the larger picture

1.4.1 North polar stratigraphy

In Chapter 2 we present evidence of a distinct change in the layering style that exists at a definite stratigraphic horizon near the base of the north polar layered deposits. By investigating the three dimensional distribution of outcrops of the lower unit we have characterized its extent and shape beneath the majority of the polar layered deposits. Our results indicate that this unit makes up perhaps 20% of the volume of the entire topographic dome of the north polar layered deposits.

In addition this basal unit has very different characteristics from the overlying layered deposits. We have showed that it is this unit that is the source of the large circumpolar sand sea which surrounds the northern polar cap.

These conclusions solve some old mysteries but provoke some new questions. It was always a problem to have sand sized particles weathering out of the layered deposits as they cannot be deposited there by atmospheric means. In the past it had been suggested that the saltating particles may be dust aggregates. However their fragile nature and inconsistent Viking color data always made this a problematic solution. In this work we remove these difficulties by having the sand weather out of a different unit which predates the north polar layered deposits. The new mystery

concerns the formation of this large sand deposit. The fact that it underlies the rest of the layered deposits indicates that there was a important episode in Martian history when there was no northern polar layered deposits. Instead the sedimentary environment supported the accumulation of a thick sand body. There are about $10^6 km^3$ of water ice currently in the northern polar layered deposits. Where this water was during that period is unknown. We offer some speculations at the end of Chapter 2 and in the concluding Chapter 5.

1.4.2 Southern residual cap geomorphology

In Chapter 3 we describe a new class of features which were not known before the MGS mission. They have been dubbed Swiss-cheese features and occur only on the southern residual CO_2 cap. They are steep walled, flat floored pits and have been observed to grow outward (but not downward) at rates of a few meters per year. To investigate their formation and evolution we have modeled the growth of pits embedded in CO_2 ice with and without an underlying substrate of water ice.

We find two situations in which we can reproduce the observed morphology and growth rates. Both involve an active dirty CO_2 slab with an increasing concentration of impurities (most likely atmospherically deposited dust) with depth. We found that underlying substrates of water ice and extremely clean CO_2 both work equally well in reproducing the flat floors. We used thermal emission data from the THEMIS instrument to distinguish between these two situations and confirmed by their temperatures that these features are underlain by a water ice substrate. This limits the thickness of the CO_2 residual cap to about 10 m and so limits the quantity of CO_2 stored there to the equivalent of $\approx$ 0.4 millibar of atmospheric pressure ($\approx$ 5% of the current atmosphere) thus placing an important constraint on the evolution of the Martian atmosphere.

We use our model results to examine the history of a population of Swiss-cheese features near the highest elevation of the residual cap. We find a narrow size distribution that indicates a common formation time and a finite period during which

new features were forming. Some change in environmental conditions occurred during this period, which we date at several Martian decades to centuries ago depending on modeled growth rates. This is exceptionally recent from a geologic point of view. We speculate on what change in environmental conditions may have started this period of Swiss-cheese formation. Environmental change on these timescales is much too short to be associated with changes in Mars orbital parameters, the atmosphere has no memory even on an annual timescale and Mars has no oceans with which it could store energy over longer periods. Larger features outside our study area have their underlying water ice exposed only near their outer walls, perhaps indicating that conditions conducive to growth may switch on and off with characteristic timescales of Martian centuries

1.4.3 Flow vs. brittle processes at the margins of the southern layered deposits

In Chapter 4 I examine features at the edge of the southern layered deposits for evidence for and against flow.

A series of craters close to the mapped edge of the south polar layered deposits contain large mounds of layered deposit material. Many of these mounds show geomorphic evidence of flow at some point during their history. I detail observations of features interpreted as compressional ridges in the ice and possible terminal moraines caused by advance and retreat of the layered deposits. Some of these crater deposits appear to be multiple superposed mounds indicating that there has been more than one period where the layered deposits have advanced and subsequently retreated in this way.

In contrast other locations in the same region show features such as brittle fracture, large-scale slumping and slope failure by landsliding. These features indicate that flow is not currently fast enough to accommodate the driving stress which caused these them.

I reconcile these contradictory observations by suggesting that there have been

alternating episodes of glacial advance and sublimation-based retreat. If the polar layered deposits wax and wane in thickness in response to variations in Mars' orbital parameters then glacial activity at its margins would also respond to the increased pressure and driving force of the thicker ice sheet.

Chapter 2

North polar stratigraphy and the paleo-erg of Mars

2.1 Abstract

An accurate self-consistent way of co-registering the imaging and topographic datasets of the Mars Global Surveyor mission was developed and used to begin a stratigraphic analysis of the northern polar region. A distinct change in the layering style exists at a definite stratigraphic horizon near the base of the north polar layered deposits. Occurrences of the contact between two distinct layered units can be mapped hundreds of kilometers apart at nearly the same MOLA elevation. The lower layered unit has a consistent association with sand dunes leading to the conclusion that it is an eroding sand rich deposit that predates most of the overlying north polar layered deposits, which exhibits the expected features of a dust-ice mixture. These results suggest that an areally extensive erg was in existence before the present ice-cap and that the present circumpolar erg is likely composed of material reworked from this older deposit. The volume of this lower unit is estimated to be on the order of 10^5 km^3. The presence of this deposit implies that there existed a period in Mars' Amazonian history when there was no icy northern polar cap. A dramatic climatic change leading to the deposition of the upper layered (icy) unit in the present day polar layered deposits represents a major event in Mars' history. However, due to uncertainties in

[1]This chapter has been published as Byrne, S., and B.C. Murray, **North polar stratigraphy and the paleo-erg of Mars**, *J. Geophys. Res., 107*(E6), 2002.

the mechanics of layered deposits formation, such an event cannot be dated at this time.

2.2 Introduction

The polar layered deposits on Mars have long been thought to contain a detailed climatic record (*Murray et al.*, 1972; *Cutts*, 1973b). The structural model commonly accepted is that of ice with varying admixtures of dust forming layers with distinct albedo and mechanical strength (*Thomas et al.*, 1992; *Toon et al.*, 1980; *Cutts et al.*, 1979; *Squyres*, 1979; *Cutts*, 1973b). Variations in Mars' orbital parameters, such as changes in obliquity and eccentricity are thought to drive climate change, which in turn gives rise to the varied depositional environments needed for distinctive layer formation (*Toon et al.*, 1980; *Ward and Rudy*, 1991).

The northern polar layered deposits are additionally complicated by the large sand sea encircling them (*Tsoar et al.*, 1979; *Dial*, 1984; *Tanaka and Scott*, 1987) which is mostly composed of the Olympia Planitia dunefield. Many authors have noted that erosion of the layered deposits may be a source of the dark sand-sized material (*Breed et al.*, 1979; *Thomas*, 1982; *Blasius et al.*, 1982; *Lancaster and Greeley*, 1990; *Thomas and Weitz*, 1989) which makes up the circumpolar erg. This would seem to pose a problem for the accepted formation scenario of layered deposits, which relies on aeolian deposition of fine dust in accumulating ice. Sand is not expected in the layered deposits because the polar cap rises over a kilometer above the surrounding plains and sand sized particles (at least in the present atmosphere) cannot be carried by suspension. It has been suggested that the dark saltating material could be composed of dust aggregates originating in the polar layered deposits (*Greeley*, 1979; *Saunders et al.*, 1985; *Saunders and Blewett*, 1987). However, *Thomas and Weitz* (1989) noted that the Viking colour and albedo values derived for the north polar dunes do not differ significantly from dark dunes anywhere else on the planet. In contrast Viking-based thermal inertia results suggest that the circumpolar erg has a lower bulk density than dunefields at lower latitudes (*Herkenhoff and Vasavada*, 1999; *Paige et al.*, 1994)

which lends support to the idea that the dunes are composed of dust aggregates or perhaps unweathered, basaltic fragments.

The northern cap complex, comprised of the northern polar layered deposits and a partial covering of residual water ice, is nearly centered on the rotational pole and sits near the lowest point of a large hemispheric depression (*Zuber et al.*, 1998; *Smith et al.*, 1998), which extends over much of the northern hemisphere. In many recent publications the ensemble structure of the polar layered deposits and the thin residual cap has been referred to simply as 'the cap', this is the convention which we will also adopt for this paper. Figure 2.1(a) shows the topographic situation of the cap. The cap contains many spiral troughs which have been attributed to the action of aeolian erosion (*Cutts*, 1973a; *Howard*, 2000), sublimation (*Ivanov and Muhleman*, 2000) or to glacial flow (*Fisher*, 1993). Chasma Boreale is a large radial chasm also cut into the cap that may have been formed through ablation, aeolian erosion (*Cutts*, 1973a; *Howard*, 2000) or some kind of catastrophic groundwater outburst (*Baker and Milton*, 1974; *Clifford*, 1980; *Clifford*, 1987; *Benito et al.*, 1997). Exposures of the layered deposits can be seen within both the spiral troughs and Chasma Boreale, as well as several arcuate scarps in the vicinity of 180°E at the cap edge. These exposures have been the subject of stratigraphic study using Viking and Mariner data (*Howard et al.*, 1982; *Blasius et al.*, 1982; *Fenton and Herkenhoff*, 2000). Work in the general area of Mars polar stratigraphy, using new Mars Global Surveyor data has also been undertaken (*Herkenhoff*, 1998; *Edgett and Malin*, 2000; *Herkenhoff and Kirk*, 2000; *Murray et al.*, 2001; *Tanaka and Kolb*, 2001; *Kolb and Tanaka*, 2001). The northern cap and its extensive set of deposits have been mapped by *Dial* (1984); *Tanaka and Scott* (1987); *Greeley et al.* (1992); *Fishbaugh and Head* (2000).

The Mars Global Surveyor (MGS) spacecraft has been in polar mapping orbit since March of 1999 (*Albee et al.*, 1998, 2001). Instruments on board used in this study are the Mars Orbiter Camera (MOC) (*Malin et al.*, 1992) and the Mars Orbiter Laser Altimeter (*Zuber et al.*, 1992). Over a year's worth of topography measurements and acquired images had been released to the public when this work was completed. Due to the spacecraft's near-polar orbit, both the imaging coverage and the topographic

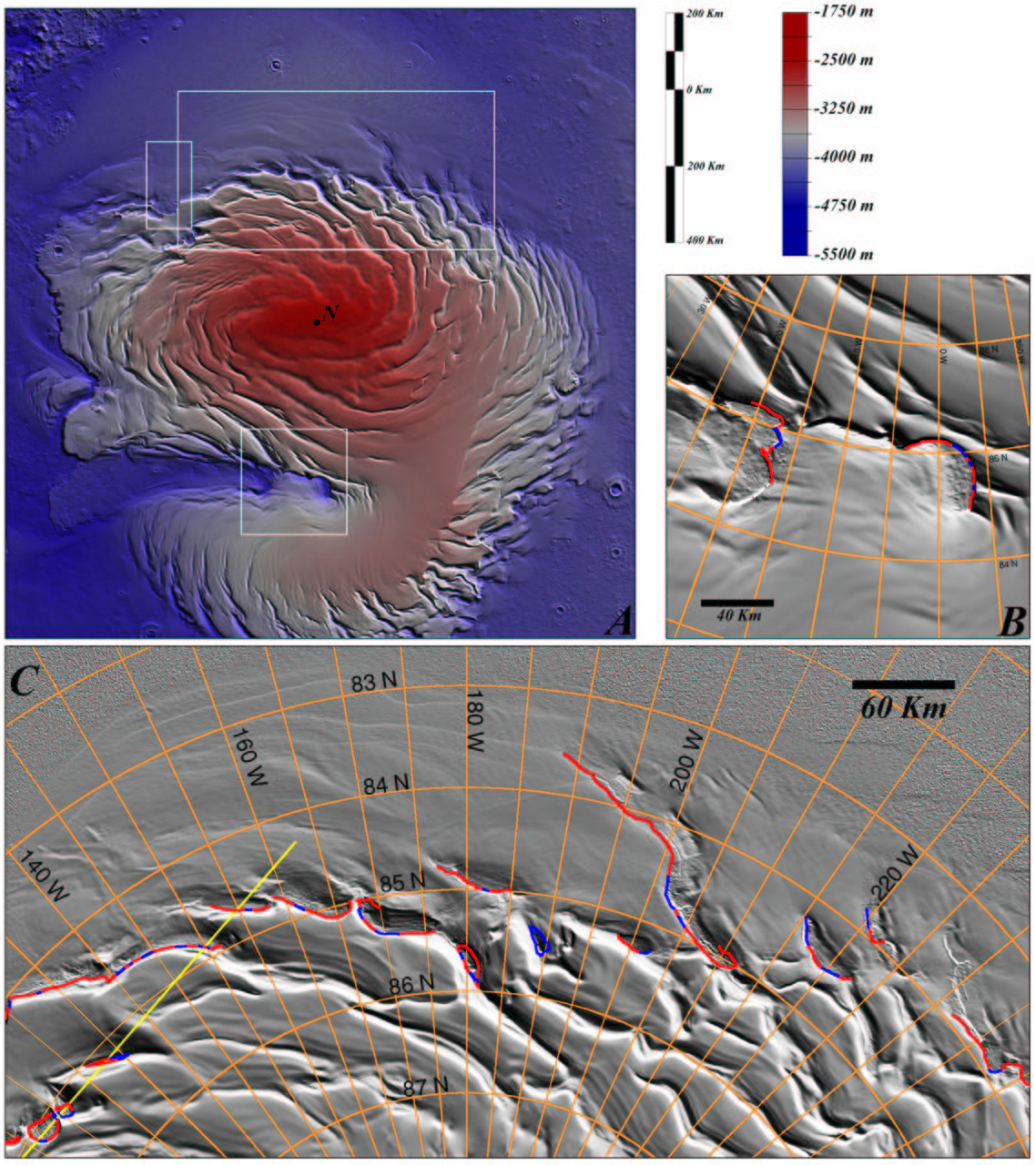

Figure 2.1: a) Digital Elevation Model constructed from approximately 28 million altimetry measurements made by MOLA. Vertical and horizontal scales are in the upper right. The DEM extends to fully include the 80th parallel and is artificially illuminated from the upper right. White boxes indicate the positions of other sub-frames in Figures 2.1 and 2.7. b) Derived shaded relief image of the region containing the head of Chasma Boreale is shown. Colored lines indicate where the contact between the finely and platy units can be mapped from the shaded relief map (red) and confirmed with MOC narrow-angle frames (blue). c) Derived shaded relief image showing area of residual cap edge centered on 180°E. Red and blue lines have the same meaning as in (b). Yellow line in lower left indicates the position of the topographic profile shown in Figure 2.3.

measurements are most dense in the polar regions. The combination of this new topographic knowledge and the ability to accurately locate high-resolution images relative to that topography makes possible for the first time a more detailed stratigraphic analysis of the stack of layers which makes up the polar deposits at both poles. Here, a surprising result, which was apparent once the technical hurdles of precisely co-registering these datasets were resolved, is reported.

The focus of this paper is to document a distinct change in the style of layering exposed in the many troughs and chasms within the northern cap at a consistent elevation. Layers above this horizon have the expected features of the canonical dust-ice mixture (*Thomas et al.*, 1992; *Toon et al.*, 1980; *Cutts et al.*, 1979; *Squyres*, 1979; *Cutts*, 1973b). Layers below this horizon differ markedly in albedo, morphology and in resistance to erosion from those above. A strong association of exposures of this lower section with occurrences of dune material is demonstrated leading to the conclusion that it is this specific section within the north polar layered deposits that is the source of the material comprising the current circumpolar erg.

2.3 Data preparation

To facilitate this and future work, high-resolution digital elevation models (DEM) of both polar regions were constructed following the method of *Neumann et al.* (2001) using the Generic Mapping Tools package (*Wessel and Smith*, 1998). The northern DEM was constructed by fitting a continuous curvature surface to approximately 28 million independent MOLA altimetry measurements. Preprocessing of the data helped reduce the volume of points to be fit and short-scale aliasing problems. Data points were initially selected to satisfy certain quality requirements (G. Neumann, MIT, personal communication, 2001) judged by parameters such as along and across track shift and crossover residuals. Off-Nadir tracks were excluded, leaving no topography information within about 180 km of the pole (poleward of 87°N); this region was separately dealt with. The spatial resolution was chosen to be 200 meters and the region covered is roughly 1200 × 1200 km centered on the pole. Tracks visibly

offset from their surroundings were removed and the surface regenerated.

The derived shaded relief map, at 200 meters per pixel, has a higher resolution than either the MOC wide-angle camera or USGS MDIMS. In addition shaded relief has advantages over visible imaging in that there is little pixel to pixel smearing, no changind seasonal frost and lighting and atmospheric effects are not an issue. For these reasons this shaded relief product was chosen as our basemap, although individual MOC wide-angle images continue to be used for albedo information where needed.

MOLA points acquired simultaneously with a MOC narrow-angle image can be located within the image by line and sample number using spacecraft time and information on the co-alignment of the MOC narrow-angle CCD and MOLA boresight (S. Anderson, A. Ivanov, JPL, personal communication, 2000). Similarly those line and sample positions can be related to MOLA derived latitude and longitude points, which are superior to those obtained from normal spacecraft orbital information since they include the MOLA crossover correction (*Neumann et al.*, 2001). This allows the MOC narrow-angle image to be map projected in a best-fit way to ensure that those MOLA points project to the correct position on the MOLA derived basemap. In this way MOC images can be placed relative to each other and their surroundings in an accurate self-consistent way. Where narrow-angle images overlap the mutual offset is commonly observed to be a few tens of meters. Radiometric calibration of the MOC narrow-angle images was performed with the USGS ISIS software package.

The imaging and topographic datasets were combined in a geographic information system package (Arcview, by ESRI) modified by us for use in the Martian polar regions. This makes spatial relationships between images (in 3 dimensions) clear, allows different data products to be overlain and permits easier distinction of topographic and albedo effects.

2.4 Change in layering style

Sections of the layered sequence within the cap and layered deposits are exposed in the many troughs and arcuate scarps both at the cap edge and in the interior. The purpose of this paper is to document a clear division of this layered sequence into two parts at a definite stratigraphic horizon. The upper, younger sequence is finely layered with smooth outcrops showing individual layers visible down to the limit of the camera resolution (hereafter referred to as the finely layered unit). The lower, older sequence is distinctly different in layer morphology, albedo and material properties. It has a characteristic irregular thick-plate-like structure in exposures, such that individual layers are less uniform both vertically and laterally (it is hereafter referred to as the platy unit). This section has lower albedo than the overlying finely layered section. Layers in both sections appear to be close to flat lying; however this is less certain in the platy unit due to the more confusing morphology. Hereafter the two sections of the northern polar layered deposits described will be referred to as distinct geologic units. This division of the polar layered deposits was noted by Malin and Edgett *Malin and Edgett* (2001) in their review of the first year of MOC observations.

The transition between these units is sharp and distinct. Figure 2.2(a) shows some examples of the contact between the units discussed in MOC narrow-angle images. Figure 2.2(b) shows how this contact is identifiable in MOLA derived shaded relief maps, the lower unit protrudes out of the bottom of scarps as a prominent step. We used the shaded relief images to map the contact between available narrow-angle MOC frames. This contact is visible over a large area; Figure 2.1(c) shows where the contact can be mapped from a combination of MOC narrow-angle frames and the MOLA shaded relief map in the 120°E - 240°E region of the cap. Figure 2.1(b) shows occurrences of this contact can be found as far away as the head of Chasma Boreale over 600 km distant. The minimum area of a circle needed to enclose all the mapped occurrences of this contact is roughly 0.4 million km^2, so assuming that the lower unit is continuous and has a near-circular shape it is at least that extensive.

Significantly, wherever this contact is visible in the 120°E - 240°E region it is

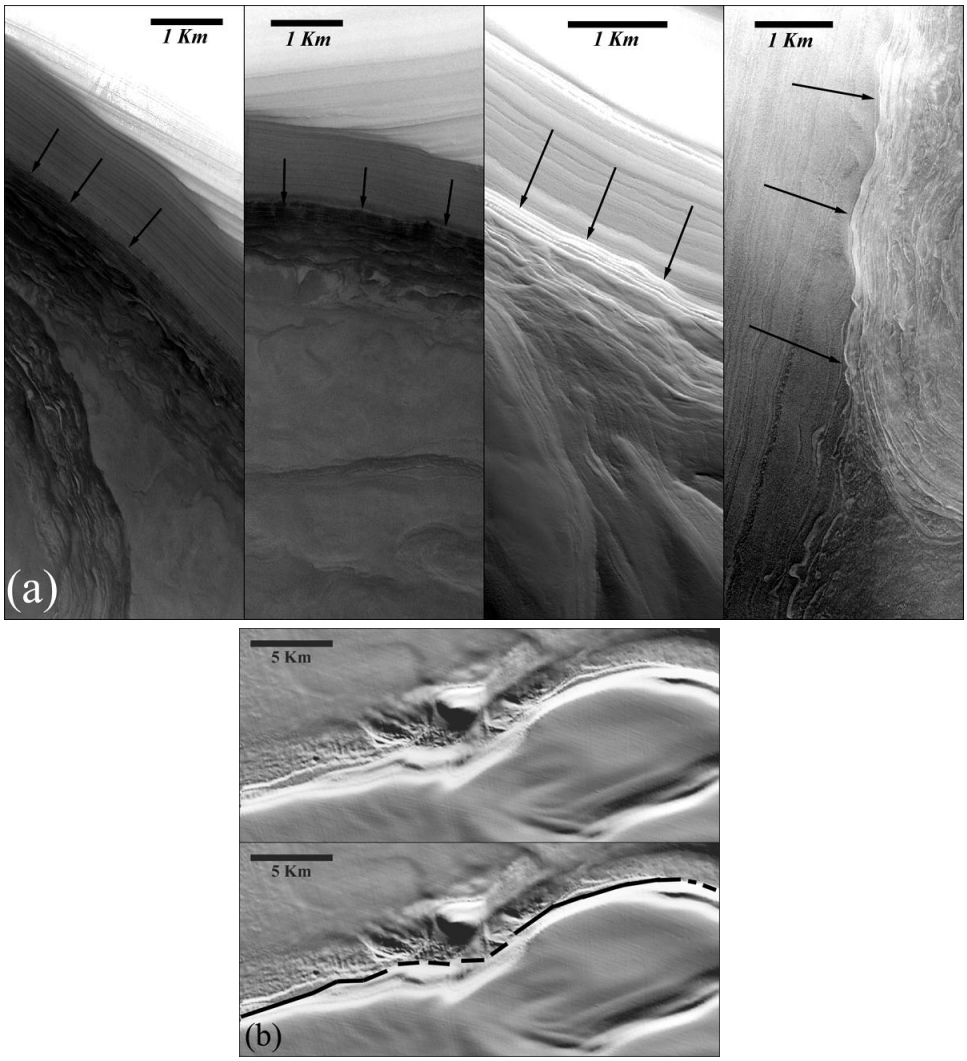

Figure 2.2: (a) Examples of the contact between the fine and platy layered units. MOC narrow-angle frames (from left to right) M02/00817 (85.1°N 192°E, sun from upper right), M03/01653 (84.9°N 199°E, sun from upper right), M17/01021 (84.7°N 217°E, sun from lower left) and M16/00329 (85.5°N 170°E, sun from upper right). The morphological difference in appearance between these two units is easily visible. The lower albedo of the platy unit is visible in the two left images; the two right images are still covered in seasonal frost, which masks the albedo contrast. The arrows indicate the downhill direction with the arrow heads pointing to the contact where the finely layered unit ends and the platy unit begins. (b) Section of MOLA derived shaded relief map with illumination from the upper right. The panels are identical except the top shows and unobstructed view of where we mapped the contact (heavy line on lower panel). The lower unit is visible as a protruding layer at the base of the scarp. Narrow angle images are used to confirm the presence of the contact at intervals along this mapped line.

observed to occur in the elevation range from -4400 to -4200 meters. The large horizontal distances and narrow vertical distribution of instances of this contact lends credence to the interpretation that it is a widespread and definite change in deposition style and material composition contained within the stratigraphic record rather than isolated patches of unusual layering with no relevance to each other. Figure 2.3 shows a topographic profile taken from the DEM along the line indicated on Figure 2.1(c). This line was chosen as it crosses a number of locations where the surface intersects the elevation range mentioned and also because at these locations narrow-angle MOC frames are available to test for the continued presence of the contact. In each case the contact appears at the expected elevation.

The lower platy unit also seems to have differing material properties to the overlying finely layered unit. On scarps where both units are exposed, breaks in slope are commonly observed at the contact, as illustrated in Figure 2.4. In other instances the lower platy unit is observed to protrude from the base of the scarp as a step, see for example Figure 2.5. In all cases a different composition for the lower platy unit, which is more resistant to mechanical or thermal erosion, can be inferred.

The differences in resistance to erosion, morphological appearance and albedo strongly indicate that the lower unit differs both in composition and deposition style. The sharp appearance of the contact could indicate that this change was rapid at least compared to the timescale of layer formation or that there may be an erosional unconformity separating the two units, representing an unknown amount of time.

No exposures of the platy unit at the cap edge in the longitude range of 290°E - 360°E and 0°E - 135°E are seen, although Chasma Boreale contains exposures within these ranges. The quality of the current MOC narrow-angle coverage was unfortunately adversely affected by a dust storm, which occurred during the M02 and M03 mapping phase (H. Wang, Caltech, personal communication, 2001). Many of the MOC narrow-angles acquired in this period contain very little surface information. Imaging conditions for the next Martian year were much clearer and this data was examined for exposures of the contact where it had not previously been seen. No new exposures were located.

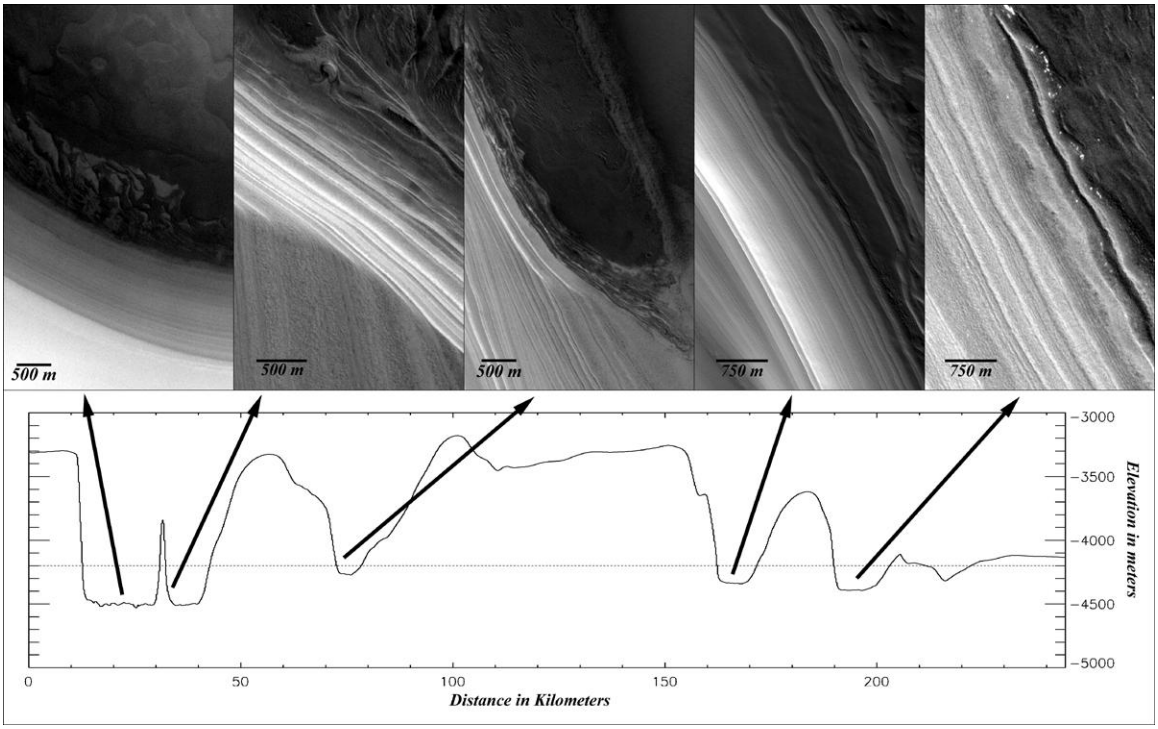

Figure 2.3: Topographic profile measured from DEM, location of which is marked on Figure 2.1(c) as yellow line. The surface intersects the level of the contact in several depressions. Example narrow-angles (which are located on the profile) from each depression are shown (from left to right) M03/02389 (85.1°N 239°E, sun from lower left), M02/00088 (85.2°N 235°E, sun from upper right), M03/04603 (85.3°N 225°E, sun from upper right), M17/00869 (84.8°N 212°E, sun from upper right) and FHA/01488 (84.8°N 203°E, sun from upper right). The elevation of the contact in each case is -4300 m, -4150 m, -4150 m, -4170 m, -4200 m, which is remarkably consistent considering the length scales involved. The downhill direction in each image is from bottom left to upper right.

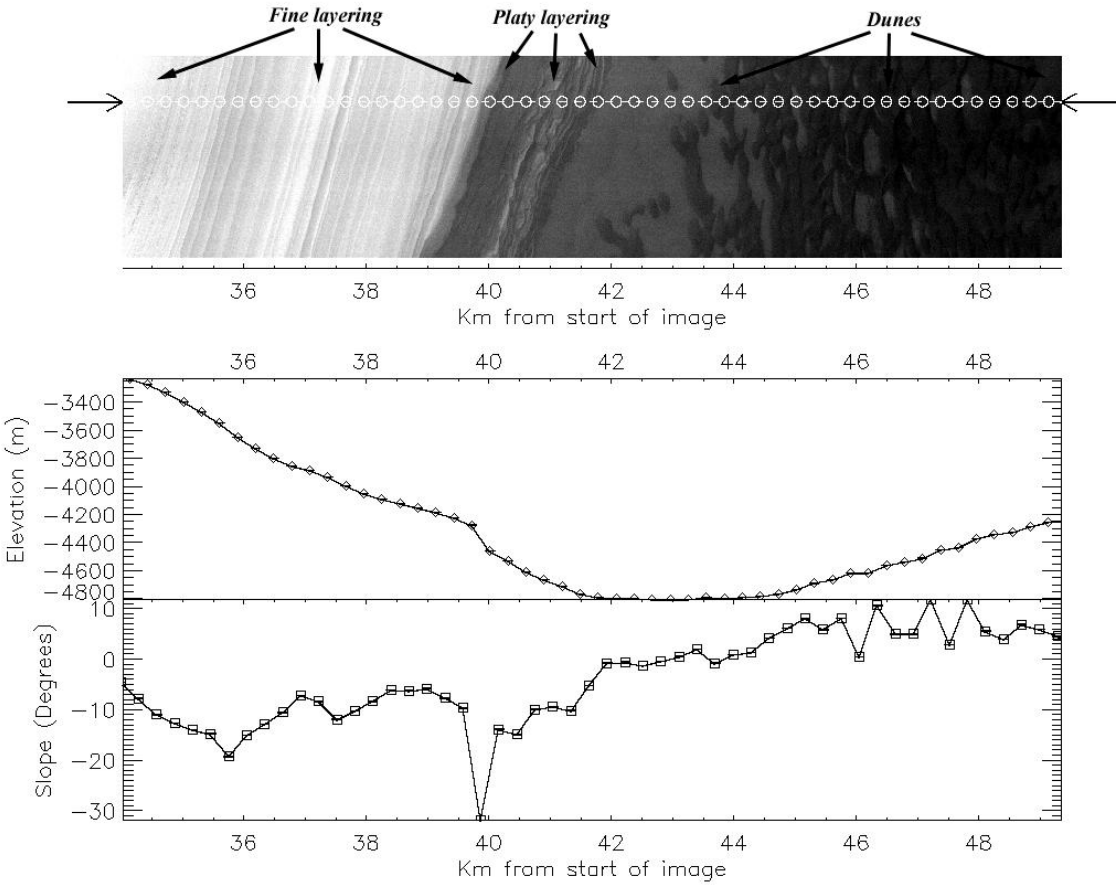

Figure 2.4: MOC narrow-angle image M03/05887 (84.7°N 172°E, sun from upper left in this orientation) along with its simultaneously acquired MOLA track. The circles on the image represent the size and location of individual MOLA shots. The shape of the scarp is clear along with the break in slope where the transition in layering style occurs. The elevation of the contact (roughly -4200 m) agrees closely with elevations recorded elsewhere (see Figure 2.3) in this region.

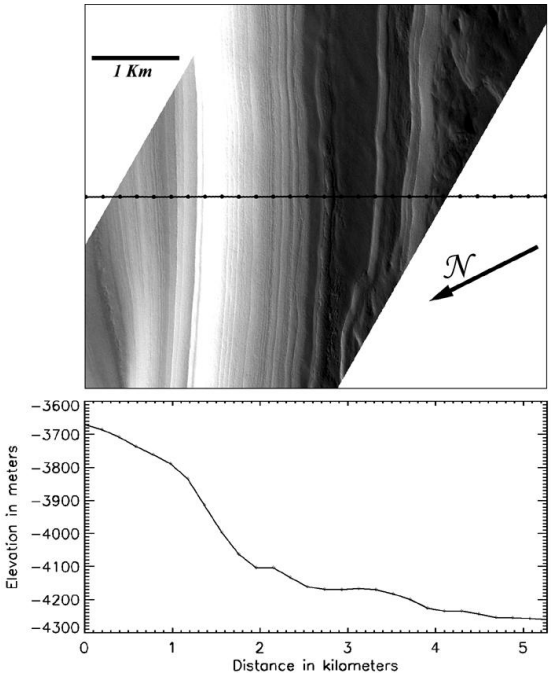

Figure 2.5: Section of MOC narrow-angle image M17/00869 (84.8°N 212°E, sun is from the right in this orientation), along with a topographic profile measured off the DEM. Here the platy unit protrudes from the bottom of the scarp by roughly 1 km; a break in slope is also visible at the contact.

2.5 Correlation with duneforms

One of the most important observations of the lower platy unit is the fact that exposures of this unit are highly correlated with the nearby occurrence of dune bedforms. Dunes require saltating particles to form, which usually implies sand-sized material but conceivably could also be sand-sized aggregates of dust (*Greeley*, 1979; *Saunders et al.*, 1985; *Saunders and Blewett*, 1987). The dunes observed here will be referred to as sand dunes however the possibility that sand-sized dust aggregates may play a role will be left open.

Many of the exposures of the contact between the two units discussed in the last section, in the longitude range 120°E - 220°E and at the cap edge, occur in closed depressions next to arcuate scarps. Although these closed depressions are 'uphill' from, and their bases are higher in elevation than, the main circumpolar erg, deposits of dune forming material are present. There is no evidence of dunes in the region between these depressions and the main erg, which would have implied poleward or

equatorward transport of dune material. Thus it appears that the dune material was derived in situ. Figure 2.6 shows some examples of dune material located adjacent to exposures of the lower platy unit. Dunes are also visible in Figures 2.4, 2.9 and 2.10 next to the exposed platy unit. *Thomas and Weitz* (1989) also noted that dunes appear to have restricted sources within the polar layered deposits. Although with Viking imagery they were unable to see the platy unit, they realized that the sources of dune material are probably in the stratigraphically older deposits.

In another area of the cap edge at roughly 235°E (illustrated in Figure 2.7) there is a large reentrant with an associated train of dunes, which are migrating southwest toward, and eventually join, the main circumpolar erg. If formed from the material eroded at the scarp, these dunes have traveled from at least where the scarp edge used to be at the time of erosion to the edge of the erg, a minimum distance of 130 km. This large minimum distance, their dark color and the inherently violent nature of the saltation process casts doubt on the possibility of these dunes being composed of sand-sized dust aggregates which may not be strong enough to survive intact. *Saunders et al.* (1985, 1986) have suggested that dust aggregates can survive saltation up to a few 10's of Km and that they can acquire their dark color by gathering carbonaceous meteoritic dust as they saltate. In this case however the minimum saltation distance exceeds their quoted survivability distance and the amount of dark carbonaceous meteoritic dust must be low since this material saltates over an otherwise high-albedo surface. The thermal inertia results (*Herkenhoff and Vasavada*, 1999; *Paige et al.*, 1994), combined with the above discussion, lend support to the idea that the dunes are composed of unweathered basaltic fragments. However, it remains unclear as to the applicability of these thermal inertia results. High local slopes within dunefields have been ignored in all thermal models and the high emission angle of the Viking observations in this area makes it likely that thermal measurements have been dominated by the 'hot' (equatorward) side of these dunes. These two facts combined could possibly lead investigators to infer an incorrect value of thermal inertia.

Although in general dune bedforms are not resolved by the MOLA data, dunefields are easily identifiable from the derived shaded relief images as areas of apparently

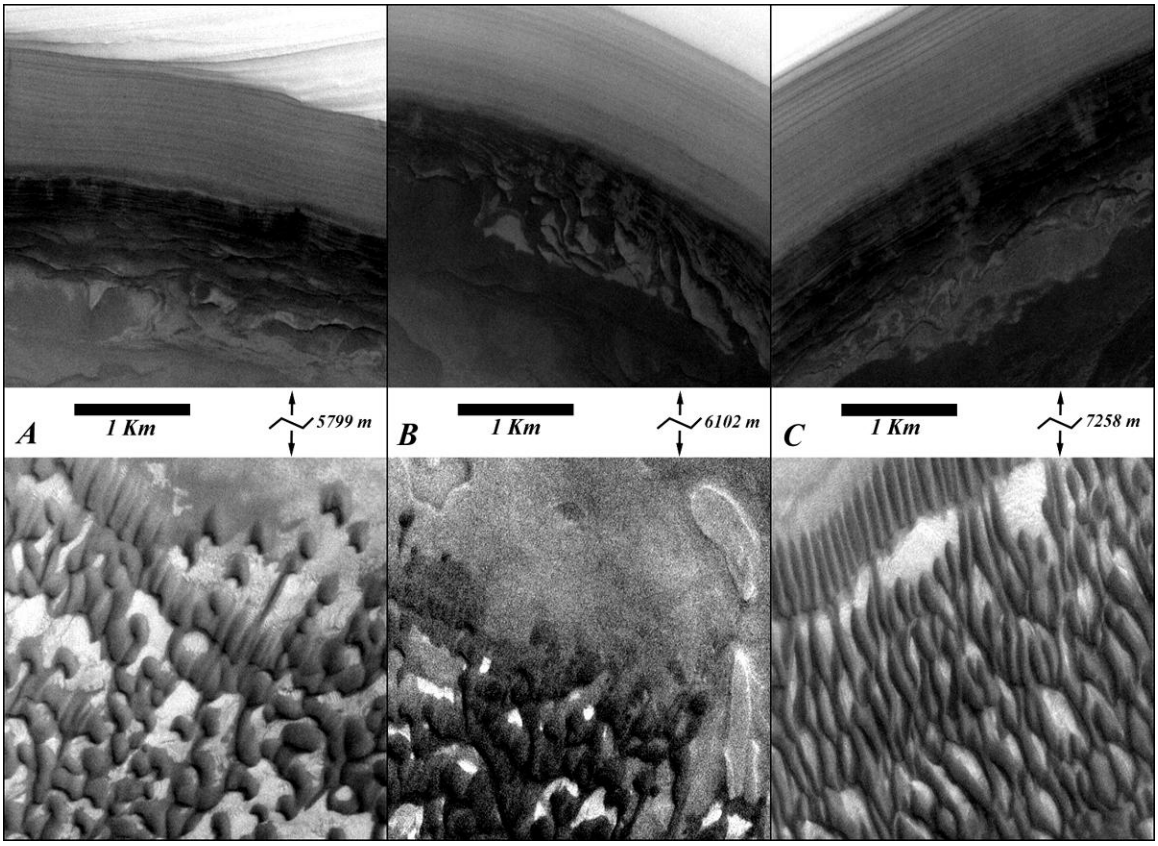

Figure 2.6: Examples of the association of dunes with exposures of the platy unit. These three MOC narrow-angle frames are from three separate closed depressions at the cap edge (a and c) and interior (b). From left to right M03/01653 (84.9°N 199°E, sun from upper right), M03/02389 (85.1°N 239°E, sun from upper right) and M03/00596 (85.4°N 190°E, sun from upper right). The images have had their center portions cropped out; the amount of missing image length is indicated between the two sections of each. The downhill direction in the upper panels is from top to bottom.

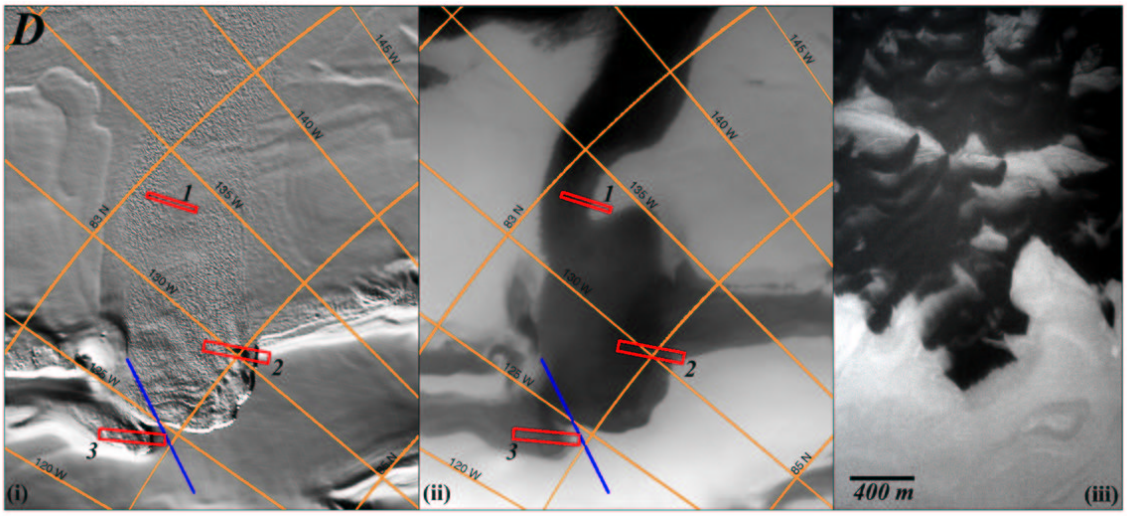

Figure 2.7: Area of cap edge at 230°E shown in i) shaded relief ii) MOC wide-angle M01/01617. This shows the correspondence of rough texture in shaded relief to dark albedo regions in the visible images, commonly associated with sand dunes. Blue line indicated on (i) and (ii) represents position of the MOLA profile shown in Figure 2.8. MOC narrow-angle outlines 1, 2 and 3 represent positions of Figure 2.7(iii), Figure 2.9 and Figure 2.10 respectively. iii) Section of MOC narrow-angle image M03/01003 (illumination from the upper right) showing the contact between dark/light, textured/smooth areas confirming the transition from a dune to non-dune area. The outline of this image is shown as 1 on Figures 2.7(i) and 2.7(ii).

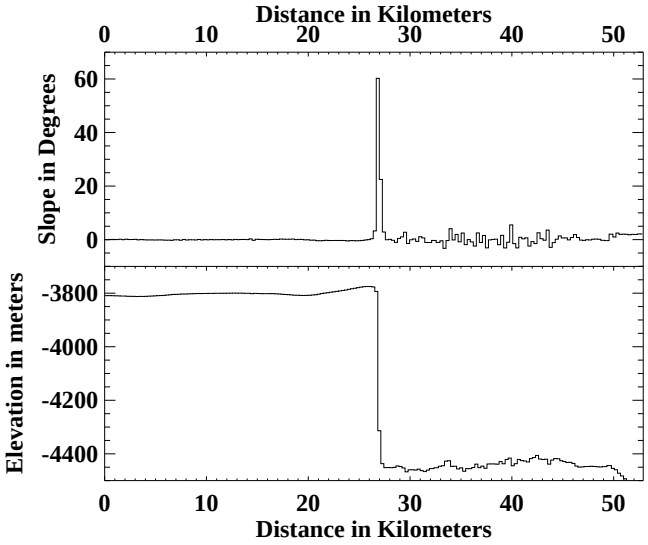

Figure 2.8: Section of MOLA profile 13387 the position of which is marked on Figure 2.7. Slope maximum at the scarp is 60.2°. When corrected to account for the non-perpendicular strike of the profile to the scarp a slope of over 67° in the downhill direction is inferred.

rough texture. Figure 2.7 shows the correspondence of rough texture in shaded relief maps to dark albedo regions in MOC wide-angle images commonly associated with dunes. Where higher resolution MOC narrow-angle images exist, they confirm that the dune covered areas can be correctly identified from the MOLA data as illustrated in Figure 2.7(iii).

A section of MOLA profile 13387 over the steepest portion of the scarp is shown in Figure 2.8, its position relative to the scarp is shown on Figure 2.7. The maximum scarp slope along the MOLA track is 60.2°. When this is adjusted to take into account the non-perpendicular strike of the MOLA trace to the scarp, then a 67.4° downhill slope is inferred. Even higher slopes may be possible over length scales shorter than the 300-meter altimeter shot separation. The extremely steep slopes, arcuate shape and interior ridges, which parallel the scarp edge and are visible in Figure 2.7(i), of the main reentrant strongly indicate an origin through successive landsliding. We interpret these interior parallel ridges to be remains of the lobate deposits expected of landslides. Why landslides should have occurred in this area is unclear to us. However given the sharpness of the scarp and the possibility of glacial-like flow or at least relaxation discussed by many authors (*Nye*, 2000; *Fisher*, 1993; *Zuber et al.*, 1998), it seems likely that at least the last of these landslides was a recent occurrence.

Figure 2.9 shows a fortuitously placed MOC narrow-angle frame, whose position is also marked on Figure 2.7(i). Although this image is taken in poor illumination and atmospheric conditions, the platy unit can clearly be seen protruding from the base of the scarp. Also of interest and perhaps more clearly visible in the Figure 2.7(i) context image is the 6.4 km crater immediately adjacent to the scarp which appears to have been uncovered recently by its retreat. Either an impact or some endogenic process may have formed the crater. The size of the feature lends support to the theory that a long period of time may be represented by an unconformity between the finely layered and platy units. In the wall of this crater is a clearly visible exposure of the platy unit. Dunes cover the eastern part of the crater providing yet another example of the correlation between contemporary dunes and the platy unit.

Immediately to the northeast of the main reentrant is another arcuate scarp and

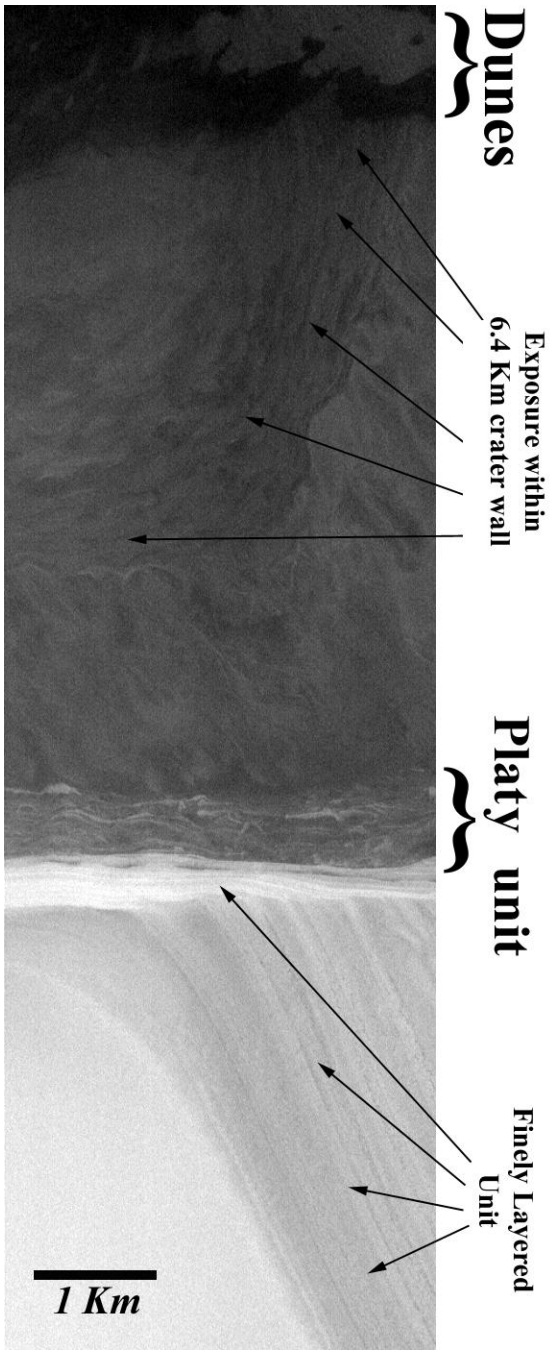

Figure 2.9: Section of MOC narrow-angle image M04/01575 (84°N 230°E, sun from upper right) showing edge of reentrant. The outline of this image is shown as No.2 in Figure 2.7. The contact between the platy and finely layered units is also visible here along with an exposure of the platy unit in the crater just below the scarp.

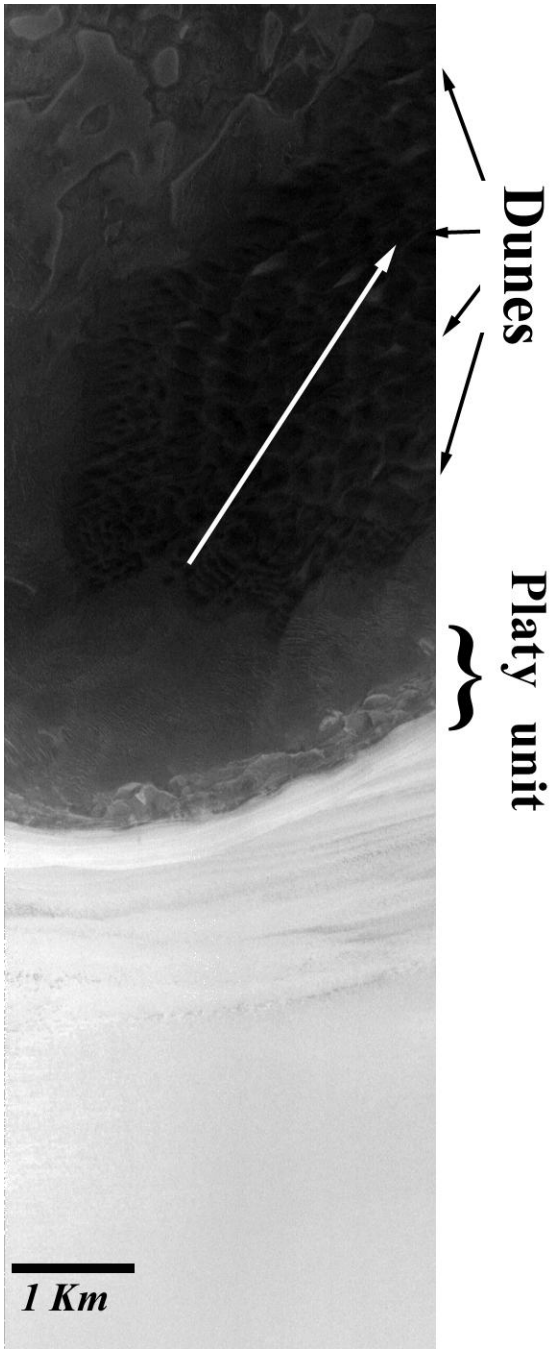

Figure 2.10: Section of MOC narrow-angle image M03/05954 (83.8°N 236°E, sun from upper right) showing another contact example and dunes climbing over ridge. The outline of this image is shown as No.3 in Figure 2.7. The direction of dune travel (which can be confirmed by observing the orientation of the slip faces of the dunes), which is transporting sand up a ridge, is indicated by the white arrow. The ridge is more clearly visible on the shaded relief image 2.7(i).

again the platy unit is visible along with associated dunes, see Figure 2.10 (outline of this image is also marked on Figure 2.7). The dunes have collected in one corner of the depression. There is a ridge approximately 100 meters high separating this depression from the main reentrant. However there is a route where slopes are low enough so that the dunes derived from the material within this depression can climb up on top of this ridge and escape down the other side into the main reentrant and ultimately the circumpolar erg. The morphology of the dunes is consistent with saltation in this direction. Although this ridge is only a few pixels wide in the MOLA shaded relief image, it has the heavily textured appearance associated with dune cover in other locations. Wide-angle views of the same location also show a thin dark streak connecting the two areas.

Chasma Boreale provides an exposure of over a kilometer of relief, cutting directly into the polar cap. It intersects the level at which one would expect to find the contact between the platy and finely layered units. Figure 2.11(a) shows the contact at the eastern head scarp of the chasma, occurring close to the expected elevation hundreds of kilometers away from the previous examples and the other side of the rotational pole. The elevation of the contact in this one image can be seen in Figure 2.11(a) to be roughly -4600 meters. This is at a lower elevation than exposures at the cap edge in the vicinity of 180°E. It could either be that the platy unit is thinner here or that the basement topography is lower. Chasma Boreale provides an opportunity to probe the location of the bottom of the platy unit. Figures 2.11(a) and 2.11(b) show the platy unit continuing down to the bottom of the chasma at -4900 meters leaving the question of how deep this layer extends unresolved. Dunes fill the chasma at many locations and while it is difficult to argue that these dunes must have been derived in-situ it is certainly consistent. The chasma contains two distinct heads (see Figure 2.1(b)); the eastern head scarp of the chasma at the higher elevation contains the contact (Figure 2.11(a)). The western head scarp also shows an exposure of the platy unit (Figure 2.11(b)); however it appears that the upper finely layered unit has been completely stripped off in this location. The eastern head scarp is cut off from the rest of the chasm by the western head scarp, a sharp cliff with slopes well above the

angle of repose, so it is reasonable to assume that the dune material in the portion of the chasma between the eastern and western head scarps must have been derived in-situ and have not have migrated in from the outside.

Troughs further poleward are higher in the stratigraphic sequence of layers and so the lower platy unit is not exposed. These toughs do not have any associated dunes and so the finely layered unit has been ruled out as a significant source of dark sand-sized material.

2.6 Discussion and conclusions

Observations of a distinct change in layering style that is evident over at least half the northern polar cap at a nearly constant elevation have been presented. Exposures of the lower platy unit are associated with the presence of nearby dune fields. This leads to the conclusion that the dune material is being derived from the erosion of the lower platy unit.

The elevation of the lowest observed outcrop of the platy unit is -4900 meters, although it may extend deeper. This is only about 200 meters above the lowest terrain surrounding the polar cap. The basement topography under the cap is largely dependent on whether the cap is compensated or not (*Johnson et al.*, 2000). However it is likely that the basement cannot be more than a few hundred meters below the lowest observed occurrence of the platy unit. The highest observed occurrence of this unit in the same region (head of Chasma Boreale) is at -4600 meters elevation, implying the platy unit is at least a few hundred meters thick in this locality.

We are of the opinion that this unit is rich in, and perhaps entirely composed of frozen sand. Due to the difficulties in co-depositing an ice-dust mixture with large amounts of sand (*Herkenhoff and Murray*, 1990a) it seems likely that this unit was deposited in a very different environment than that needed to deposit the upper unit or that of present day Mars. The Olympia Planitia dunefield, which sits atop the Olympia lobe, ranges in elevation from roughly -4200 to -4700 meters. This is the same elevation range over which exposures of the sand rich deposit are seen. We

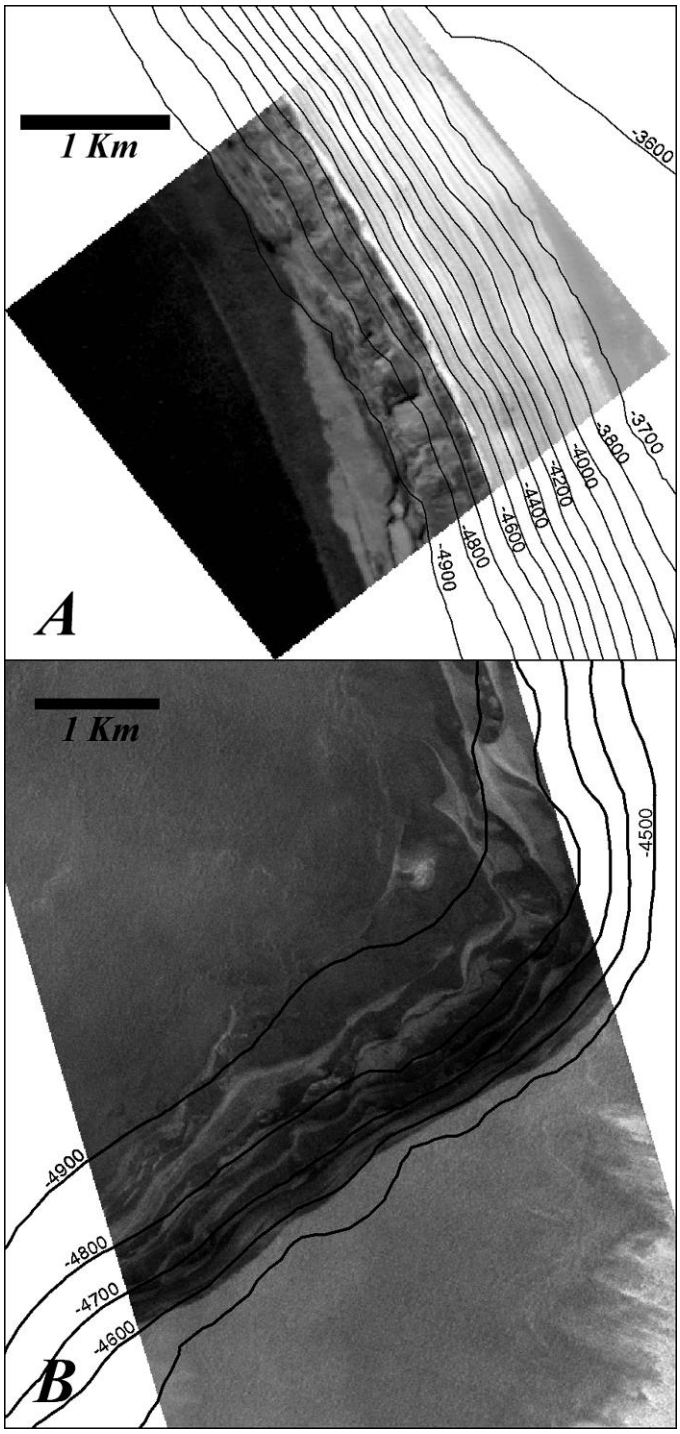

Figure 2.11: a) MOC narrow-angle image M01/01410 (84.9°N 3°E, sun from bottom in this orientation) with overlain MOLA elevation contours showing the contact between fine and platy layered units at the eastern head scarp of Chasma Boreale. Contact elevation in this locality can be seen to be roughly -4600 m. b) MOC narrow-angle image M03/03107 (84.8°N 344°E, sun from bottom in this orientation) also overlain with MOLA elevation contours showing an exposure of the platy unit continuing down to -4900 m at the western head scarp of Chasma Boreale. Here it appears the finely layered unit has been completely removed as the scarp top is at -4600 m.

suggest that the Olympia lobe is composed of the same sand-rich, platy unit which extends under the north polar layered deposits. The Olympia Planitia dunefield and the rest of the circumpolar erg could then be composed of material eroded from this platy unit. This would vastly increase the minimum size of the platy unit initially estimated in section 3.

A possible geologic history is outlined in Figure 2.12, which represents a cross-section through the polar deposits from 75°N, 0°E (left) through the pole to 75°N, 180°E (right). A large sand or sand-rich deposit is postulated to have formed before the existence of the present day north polar cap. It may be that sand-sized particles migrated to this locality through aeolian action from elsewhere on the planet and the broad topographic low centered roughly on the north pole seemingly served as an effective sink for this material. From mapping the contact elevations in Chasma Boreale and the arcuate scarps at the cap edge, the center (thickest part) of the deposit is interpreted to be offset from the rotational pole along the 180°E meridian. This interpretation is dependent on having reasonably flat basement topography. A shift in environmental or climatic conditions caused the present ice-cap to begin forming. This may be related to some climatic change triggered by a chaotic obliquity swing (*Touma and Wisdom*, 1993) or perhaps even to the end of large-scale volcanism on the planet. The accepted mechanism of deposition of ice with varying concentrations of dust could create the finely layered ice-cap. This icy cap may have been much larger in the past and only more recently retreated to its current extent (*Fishbaugh and Head*, 2000). This climatic shift need not have been sudden; a relatively shallow covering of ice could stabilize any dunes thus allowing the rest of the cap some time before starting to form. Finally at some point in the past Chasma Boreale and the spiral troughs formed, cutting through the cap into the platy deposit underneath (where the cap is thin enough). A highly porous sand deposit could have stored the large amounts of groundwater needed for the catastrophic outburst theorized to have formed Chasma Boreale. Groundwater in the platy unit would not be liquid under present conditions and so this mechanism would require some form of heat injection such as that theorized by *Benito et al.* (1997) or much higher planetary heat flow

in the past. In this scenario, since the icy portion of the cap formed symmetrically about the rotational pole, the upper finely-layered unit drapes completely over the lower unit in the vicinity of 0°E (left side of Figure 2.12). For this reason no exposures of the platy unit are expected to be observed at the edge of the cap in this region.

Accumulation of the platy unit may have occurred over a considerable period of time with many episodes of dune migration involved. Modest obliquity changes could have mildly affected polar climate and insured that each episode of dune deposition could contain differing quantities of ice leading to stratigraphic variations in erosional resistance. Incorporation of bright dust in such units can be ruled out however as saltating particles would kick dust back into suspension (*Herkenhoff and Murray*, 1990a). The irregular outcrops of the platy unit are consistent with laterally-variable resistance to erosion, perhaps due to variable dune thickness. A large enduring change in mean obliquity, as modeled by *Touma and Wisdom* (1993), could have ended this depositional period, and begun that of the overlying ice-dust mixture of the northern polar layered deposits.

If Figure 2.12 is an accurate representation of the current situation, the volume of material contained within the platy unit can be approximated. Taking it to be a section of a sphere with a radius of 540 km and height of 600 m the volume occupied is 0.27 million cubic kilometers. For comparison the volume of the total north polar cap is 1.2 to 1.7 million cubic kilometers (*Zuber et al.*, 1998) and the volume of sand in the present day erg has been estimated at 1158 cubic kilometers (*Lancaster and Greeley*, 1990). Even assuming a large percentage of pore space (which is presumably filled with ice), e.g., 50%, the volume of rock eroded to produce this material is on the order of 10^5 km^3.

At the cap edge in the vicinity of 180°E (right side of Figure 2.12) the Olympia Planitia dunefield could have once extended further equatorward. However since it lacks the protective cover of the ice-cap it would have been subject to erosion and would have possibly liberated large quantities of sand. This sand could be that which forms the remainder of the circumpolar erg. It is difficult to estimate a timescale over which this process would occur since it is an open question as to how much of the year

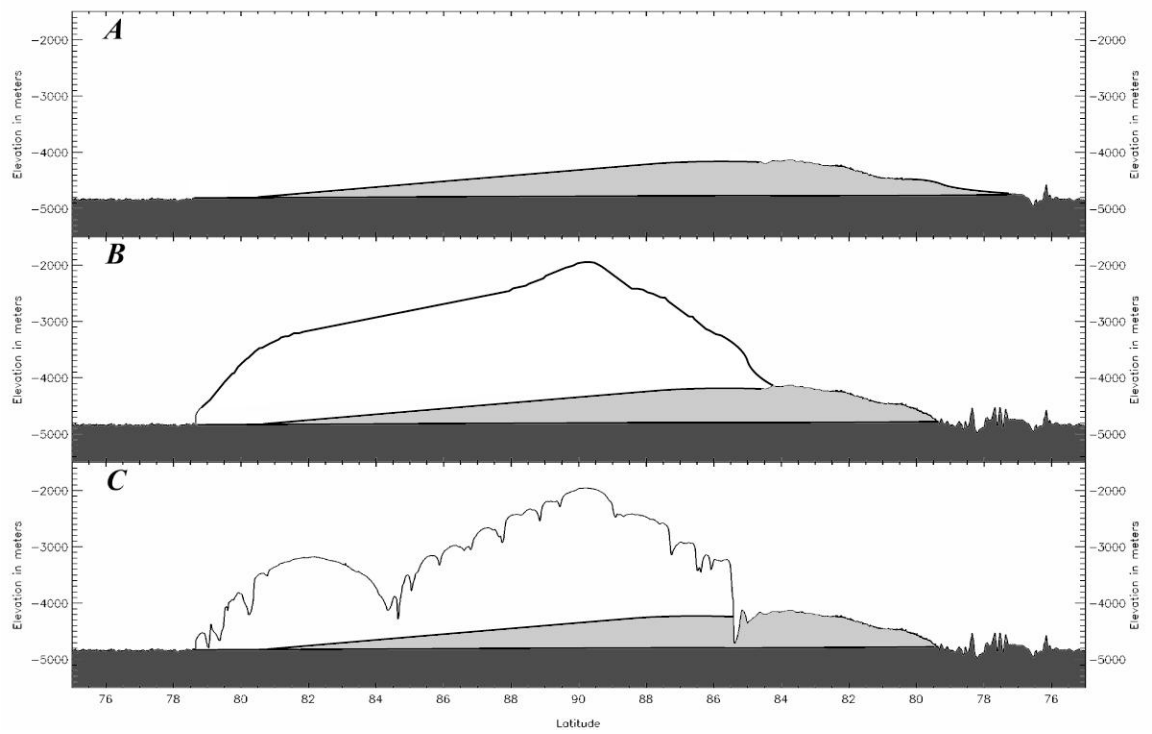

Figure 2.12: Possible geologic sequence of events, vertical exaggeration of 100: a) The northern hemisphere acts like a large depression centered on the pole. A large erg collects there from sand derived elsewhere on the planet. b) A dramatic change in climate results in the formation of an icecap. Deposition of ice centered on the pole with varying concentrations of dust, perhaps modulated by obliquity cycles, produces the finely layered unit. The exposed section of the paleo-erg is eroded back perhaps releasing the sand found in the present day circumpolar erg. c) Formation of Chasma Boreale and the spiral troughs which incise the cap, some of which cut into the lower sand unit. Present day MOLA profile 11734.

these dunes are free to saltate (*Ward and Doyle*, 1983). Previous wind regime studies (*Thomas and Gierasch*, 1995) concluded that the current circumpolar erg is confined to a narrow latitude band by winds created in part by its own low albedo. Thus this dark, sand-sized material would not be expected to have been re-distributed over a large fraction of the planet.

The major implication of this newly-recognized deposit is climatic in nature. The fact that the icy part of the northern polar cap was absent at some point indicates a much warmer polar environment than present. The northern cap is also the largest known reservoir of water on the planet. Where this water was in the past if not locked up in the polar cap is a puzzling mystery. It is possible that the water was concentrated at lower latitudes filling craters and is responsible for the apparent sedimentary exposures reported by *Malin and Edgett* (2000). A secondary implication is that no exotic polar dust aggregates are needed to explain how sand can possibly be weathering out of the current layered deposits. The low thermal inertia results (*Herkenhoff and Vasavada*, 1999; *Paige et al.*, 1994) still prove to be an unresolved issue though.

2.7 Acknowledgements

I am especially grateful to the MOLA and MOC teams for providing their high-quality data in such a prompt manner. I would like to especially thank Anton Ivanov (master of all things MOLA) for his help in acquiring MOLA data in an accessible form and Lori Fenton for her help in understanding dunes and all the cool stuff they can do. I would also like to thank Arden Albee, Andrew Ingersoll, Mark Richardson and Ashwin Vasavada for their comments (and encouragement). Finally I'd like to thank Ken Herkenhoff for his comments as a reviewer when this work was published; the paper was very much improved as a result.

Chapter 3

Analysis and modeling of south polar geomorphology

3.1 Abstract

Flat-floored, quasi-circular depressions on the southern residual cap of Mars have been observed to expand rapidly. We have developed a model to explain their formation and evolution. The model computes the energy balance of CO_2 frost within an arbitrarily shaped depression including all orders of scattering of solar and infrared radiation as well as heat storage in a water substrate. Due to their observed lateral expansion rate of 1-3 m/yr, these depressions must form in a CO_2 medium. However, it was found necessary to include a less-volatile layer within the polar cap to ensure the modeled depressions develop their observed flat floors. This less-volatile layer could either be water ice or clean CO_2. Above this less-volatile layer lies an active slab of low-albedo CO_2 which is consistent with the late summer appearance of the depression walls. We found it necessary to include an albedo gradient within this active CO_2 slab to encourage the modeled depressions to develop steep walls. This gradient could represent an increasing concentration of impurities with depth. Our derived expansion rates range from 0.5-2.5 m/yr, which agrees well with observations.

THEMIS data were used to distinguish between the two possible substrate mate-

[1]Material in this chapter includes Byrne, S., and A.P. Ingersoll, **A sublimation model for Martian south polar ice features**, *Science, 299*, 1051-1053, 2003. and Byrne, S., and A.P. Ingersoll, **Martian climatic events on timescales of centuries: Evidence from feature morphology in the residual south polar cap**, *Geophys. Res. Lett, In press*, 2003.

rials. These observations show that water ice makes up the floors of these features. This fact combined with the observed shallow depths of these depressions places limits on the contribution of the entire residual cap to the global reservoir of CO_2. This contribution is found to be extremely small, and would total only ≈ 0.4 millibar of equivalent atmospheric pressure if totally sublimed.

Analysis of the size distribution combined with modeling of the growth process yields information about the ages of these features. We report on properties of a population of these features within a selected study area. We find a narrow size distribution that indicates a common formation time and a finite period during which new features were forming. Some change in environmental conditions occurred during this period, which we date at several Martian decades to centuries ago depending on modeled growth rates. Some features in other areas may record more than one growth phase, indicating that conditions condusive to growth may switch on and off with characteristic timescales of Martian centuries.

3.2 Introduction

The nature of the southern residual CO_2 cap and the reasons behind its year-round existence have been the subject of a long-running debate. *Leighton and Murray* (1966) first suggested that the polar caps constitute a large permanent reservoir of CO_2, much larger than the atmospheric reservoir, whose vapor pressure determines the CO_2 partial pressure on Mars. *Murray and Malin* (1973) argued that the permanent reservoir would reside in the north because its lower elevation allows the CO_2 ice to equilibrate with the atmosphere at a higher temperature and pressure than in the south. *Ingersoll* (1974) pointed out that the rapid retreat of the seasonal polar cap and the high abundance of water vapor are incompatible with a permanent CO_2 cold trap. Nevertheless, the Leighton and Murray model became the paradigm for the climate of Mars because it explained the atmospheric pressure and accounted for any extra (non-atmospheric) CO_2 in the system.

On the basis of Viking observations *Kieffer et al.* (1976) showed that the CO_2

in the north disappeared during the summer, uncovering a residual cap composed of water ice. *Kieffer* (1979) showed that the southern residual cap retained a covering of CO_2 all year. It has been argued that the reason behind the survival of the south's CO_2 covering was the increase in albedo observed in response to increased insolation (*Paige*, 1985; *James et al.*, 1992). *Jakosky and Haberle* (1990) suggested from model results that both residual caps could switch between two states, one of which was permanently covered with CO_2 (present day south pole situation), the other in which the CO_2 could disappear at the end of each summer season (present day north pole situation), exposing a darker substrate. They used these findings to attempt to explain the 1969 telescopic observation of dramatically increased water vapor concentrations above the southern pole (*Barker et al.*, 1970). Sublimation of such quantities of water ice would only be possible if its temperature were increased far above the CO_2 condensation temperature, indicating that all CO_2 had already sublimed. A conclusion such as this would indicate the residual cap is thin enough to almost entirely disappear in certain years, perhaps in response to episodically vigorous dust storm activity.

Smith et al. (1999) and *Nye et al.* (2000) showed, using results of recent creep experiments on CO_2 ice (*Durham et al.*, 1999) that the present day south polar cap could not possibly support its own weight over long timescales if it were wholly composed of frozen carbon dioxide. The consensus emerging is that of a large topographic dome of dust and water ice, which is topped with a thin skin of CO_2 ice of unknown thickness (*Albee et al.*, 2001). The thickness of this residual CO_2 layer bears directly on the question of the global inventory of this important volatile.

More recent observations conducted with the Mars Orbiter Camera (MOC) have revealed this residual CO_2 deposit to contain a wide range of landforms (*Thomas et al.*, 2000). Among the most interesting and populous are flat-floored quasi-circular pits with steep walls (Figure 3.1), which have been dubbed Swiss-cheese features. In the next section we fully describe these features and their observed characteristics. We will describe the model that we have developed to explain their formation and growth. By modeling sublimation and conduction processes we investigate the

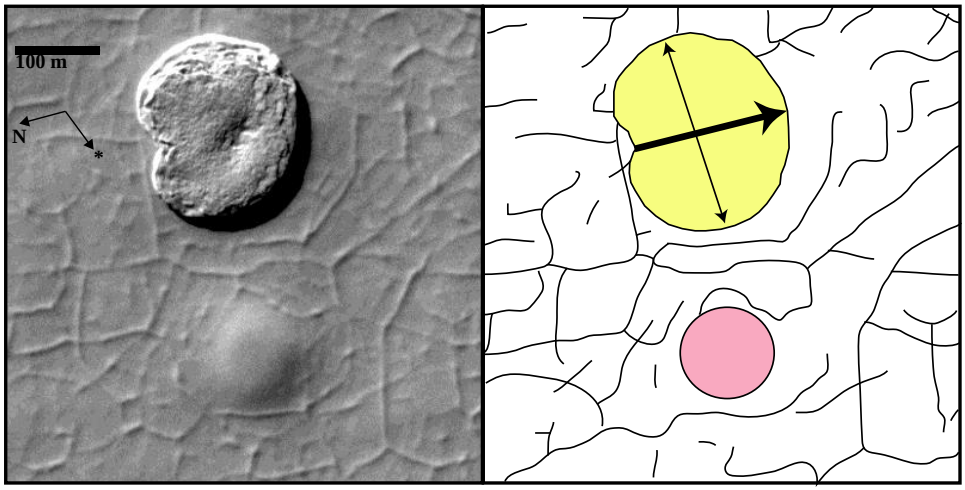

Figure 3.1: High-resolution view of a typical Swiss-cheese feature. Most of the salient features of the Swiss-cheese features are visible here, including steep walls, flat floors, and a slight asymmetry in the north-south direction. Illumination is from the lower-right. Just below and to the right is a slight depression which may be the progenitor of a future Swiss-cheese feature. The grooved appearance of the surrounding terrain is commonly observed near these features. In this and subsequent figures arrows denote the direction to the sun (*) and north (N). The thick arrow in the associated cartoon shows how the azimuth of these features were mapped (see Section 3.8) and the thinner double headed arrow shows a typical size measurement. Sub-frame of MOC narrow-angle image M09/00609, taken at 87°S, 353°E, L_s 237°.

evolution and formation of depressions embedded in CO_2 ice with and without an underlying layer of water ice. Our modeling of these features suggests two possible stratigraphic configurations; an active low-albedo slab of CO_2 underlain by either water ice or clean CO_2. We will use thermal data to distinguish between these two possibilities. Finally we select a region of interest on the south residual cap (see Figure 3.21) and use our model to infer the history of the population of Swiss-cheese features found there.

3.3 Feature description

Swiss-cheese features were first identified by *Thomas et al.* (2000) using Mars Orbiter Camera (MOC) narrow-angle imagery. There are two types of Swiss-cheese features being discussed in this work; archetypes of both are illustrated in figures 3.1 and 3.2. Many of the following characteristics were noted in *Thomas et al.* (2000).

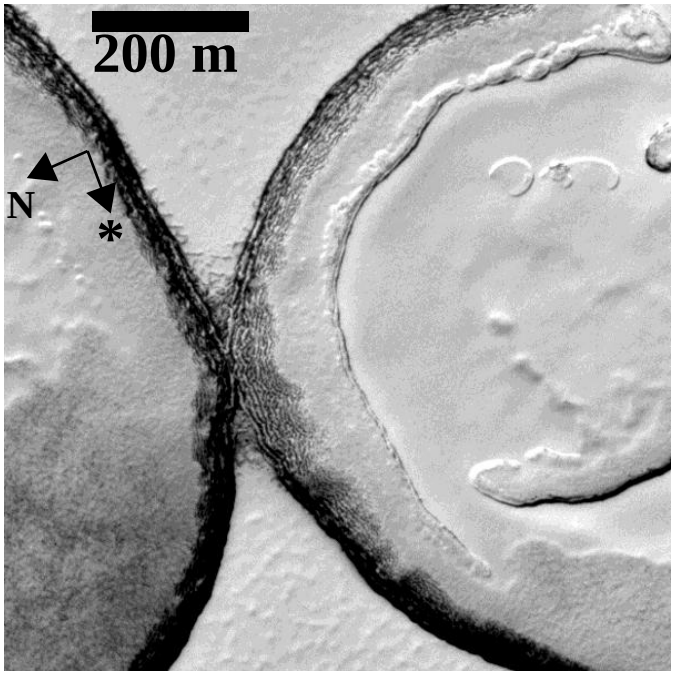

Figure 3.2: Larger Swiss-cheese feature showing characteristic moats around inner edge of walls. Also illustrated here are layers in the walls of the Swiss-cheese features. In some places only two main layers can be seen, in this case up to 15 closely spaced layers are visible. Sub-frame of MOC narrow-angle image M12/01995, taken at 86.9°S, 17°E, L_s 305°.

The first type (see Figure 3.1) is common within our study area (see Figure 3.21). They are a few hundred meters across and have a small spread in size range. All shadow measurements to date indicate a consistent depth of 8-10 m. They vary from

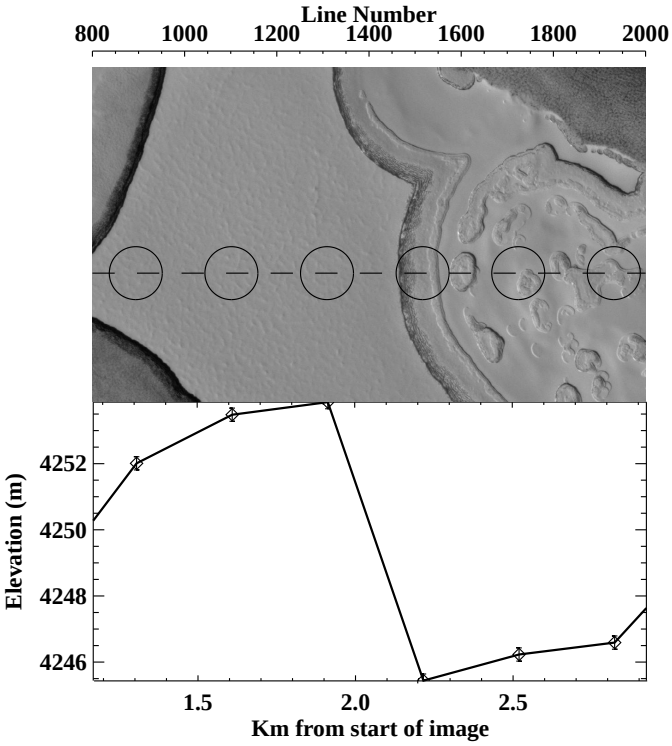

Figure 3.3: Sub-frame of MOC narrow-angle image M12/01995, taken at 86.9°S, 17°E, L_s 305°, along with simultaneously acquired MOLA topography data. The circles superposed on the image show the location and size of the MOLA laser shots. The plot underneath shows how height varies from point to point. The relief over this scarp appears to be slightly greater than 8 meters once the regional slope is removed.

heart shaped to almost circular, with a clear symmetry axis that is aligned north-south (see Figure 3.22). This combination of characteristics has not been observed in Swiss-cheese features elsewhere on the residual cap.

The second type (see Figure 3.2) occurs more widely on the residual cap and is not confined to any particular region. The defining characteristic of this type of Swiss-cheese features is an interior moat running around the inside of the walls with the central floor being slightly elevated (by about two meters). They tend to be larger, with diameters of up to 1-2 km. The walls are generally less steep; the equatorward facing walls tend to be steeper than poleward facing walls. Depth measurements are possible from the Mars Orbiter Laser altimeter (MOLA) and are again consistently 8-10 m (see Figure 3.3).

Where the walls are shallowly sloping it can be seen that the medium in which the Swiss-cheese features are embedded is composed of several layers (see Figure 3.2). Swiss-cheese features change their appearance toward the latter part of the summer as the seasonal frost disappears. Their walls and moats appear to darken considerably

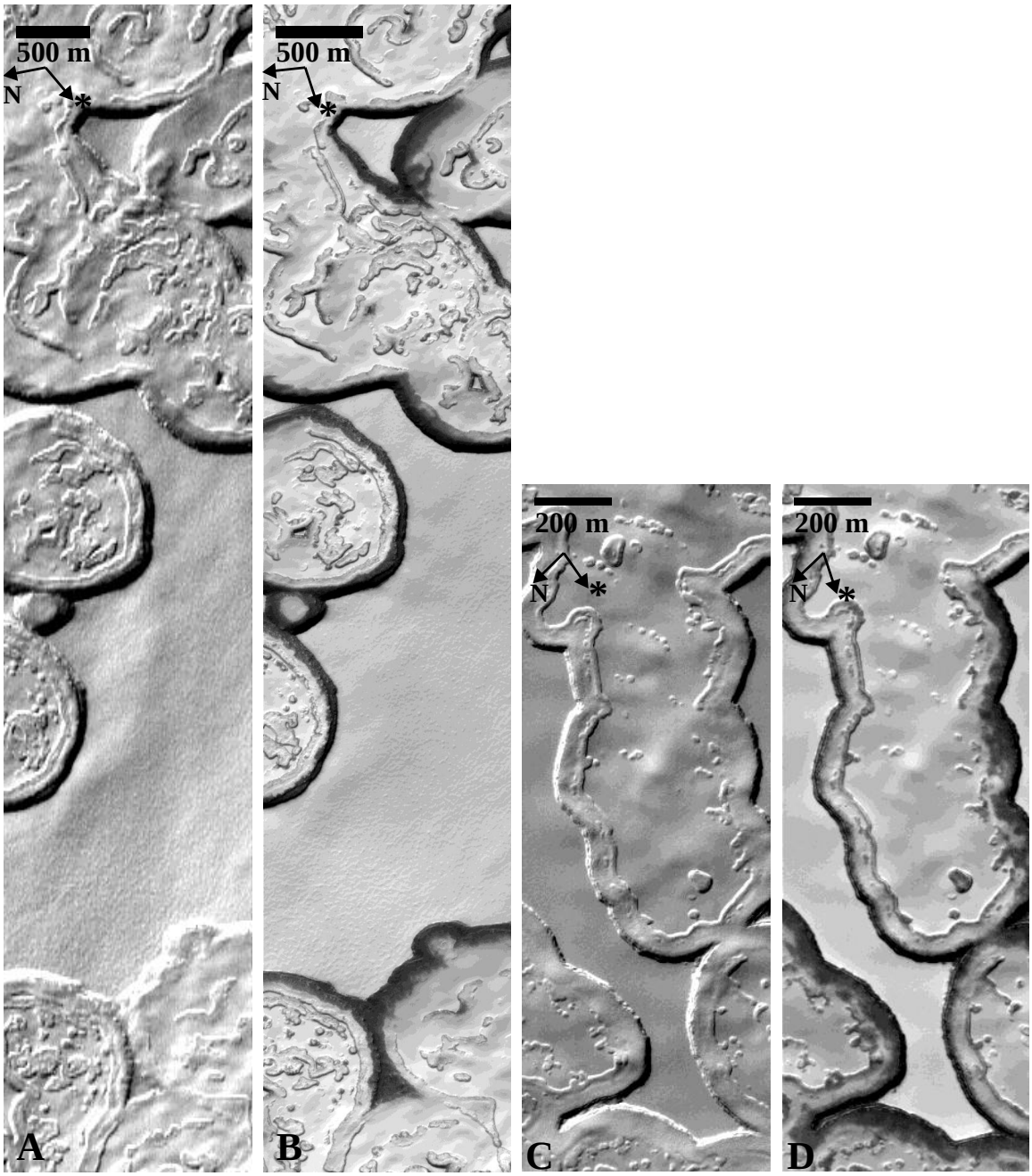

Figure 3.4: Albedo changes as the seasonal CO_2 cover is removed and the true residual CO_2 cap is exposed. The walls and interior moats of the features become darker than the surrounding surface. Shown here are two areas at 87.1°S, 18°E (A and B) and 86°S, 11°E (C and D). A and B are sub-frames of E05/02028 and M13/02199 at L_s of 182° and 328° respectively. C and D are sub-frames of M09/04708 and M13/02177 at L_s of 246° and 327°, respectively.

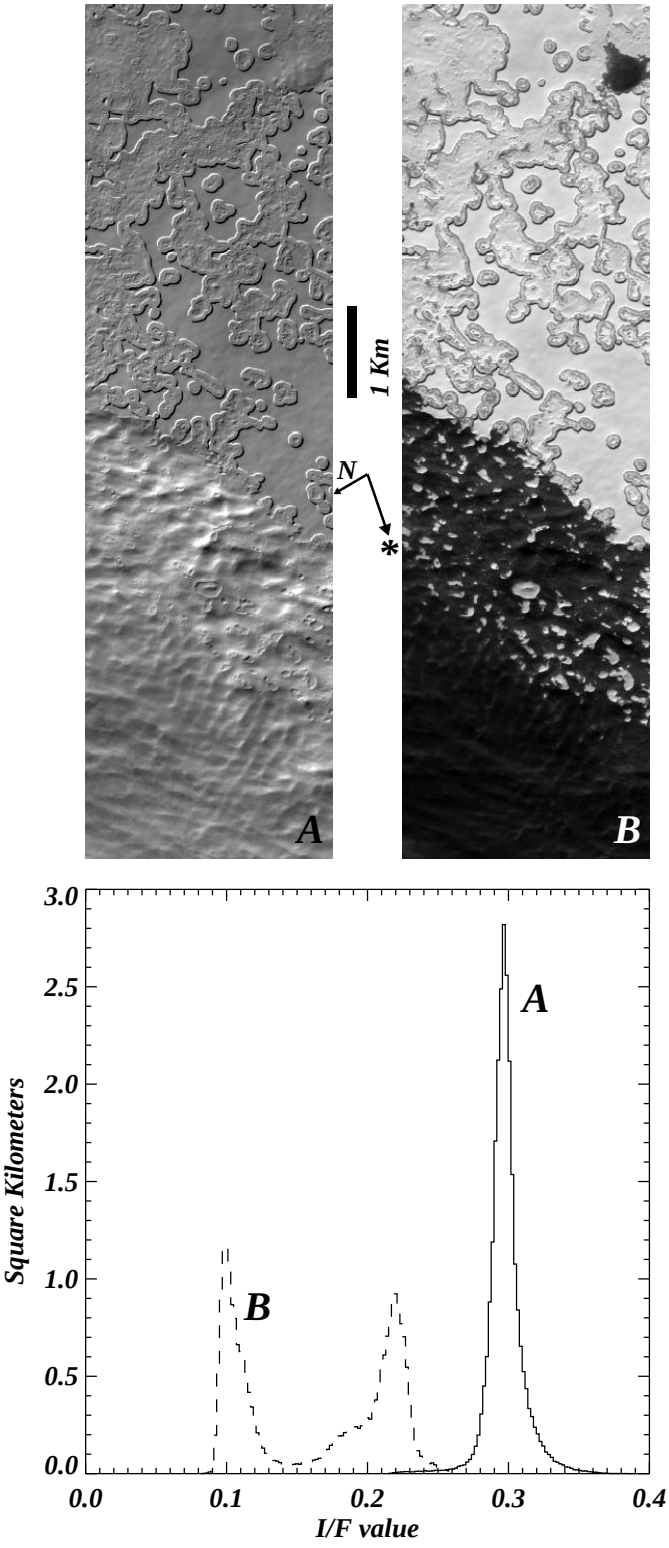

Figure 3.5: Example of the defrosting cap edge at 87°S, 30°E between L_s 235° (MOC image A, M08/07803) and L_s 321° (MOC image B, M13/01301). Swiss-cheese features can be seen to be present right up until the border of the residual cap indicating that the residual CO_2 deposit in this area is extremely thin. The associated histograms show I/F distributions (equivalent to Lambert albedo for normal viewing and assuming no atmosphere) for the two scenes.

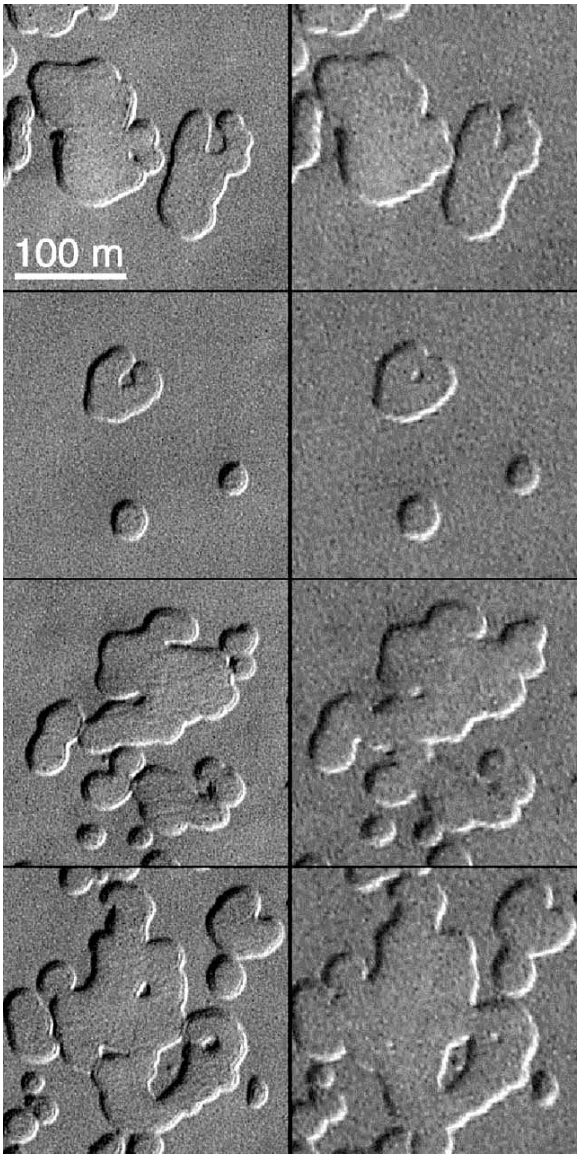

Figure 3.6: Inter-annual expansion of Swiss-cheese features. The walls have retreated by an estimated 3 meters and some small features have disappeared entirely. Left Panels are from M08/04518 (incorrectly labeled as M08/04516 in original paper), taken at L_s 227°, right panels are from E07/01565, taken at L_s 219°. Location is 87°S, 253°E. From *Malin et al.* (2001).

relative to the surrounding terrain (*Malin and Edgett*, 2001). The surrounding flat upper surfaces and raised central islands do not to change in this way (see Figure 3.4).

These features occur throughout the residual cap, in most cases right up to the edge of the residual CO_2 deposit as can be seen in Figure 3.5. The fact that these depressions are strictly confined to the residual cap indicates that the medium in which they form is dominated by CO_2 ice and also that the CO_2 covering of the residual is at least as deep as the relief of these depressions (about 8 m in most cases). *Malin et al.* (2001) showed, using images separated by 1 full Mars year, that the walls of these depressions are retreating at the rate of 1-3 meters per year (see Figure 3.6, taken from that article). Such a rate of retreat is only possible if the medium in which they are embedded is highly volatile, i.e., CO_2 ice.

3.4 Model description

We have created a model to investigate the growth of arbitrarily shaped cylindrically symmetric depressions in CO_2 ice. The depressions are represented by a series of facets, which are free to move due to sublimation or condensation of carbon dioxide and are assumed to be Lambert scatterers. The temperature of each facet is fixed at the sublimation point of CO_2. The model accounts for incident short-wave radiation (including shadowing), emitted thermal radiation and all orders of scattered long and short wave radiation. The energy balance of each facet is calculated independently and its position is updated to take account of any condensation or sublimation of CO_2 that has taken place. In this way the shape of the modeled depression is constantly changing. Appendix B gives details of this calculation. Following *Vasavada et al.* (1999) we use a matrix inversion approach ("radiosity") to calculate all orders of scattering.

We assume cylindrical symmetry, which is valid only for a circular feature exactly at the south pole. However cylindrical symmetry provides a good approximation since the observed depressions are roughly circular and the Sun circles each day at almost

the same elevation at 87°S. This situation is analytically tractable in the special case when the depressions are sections of spheres (*Ingersoll et al.*, 1992). Our numerical model was tested against the analytic solution for these cases and found to deviate only slightly. Figure 3.7 illustrates a comparison between the analytic solution and model for a range of circumstances.

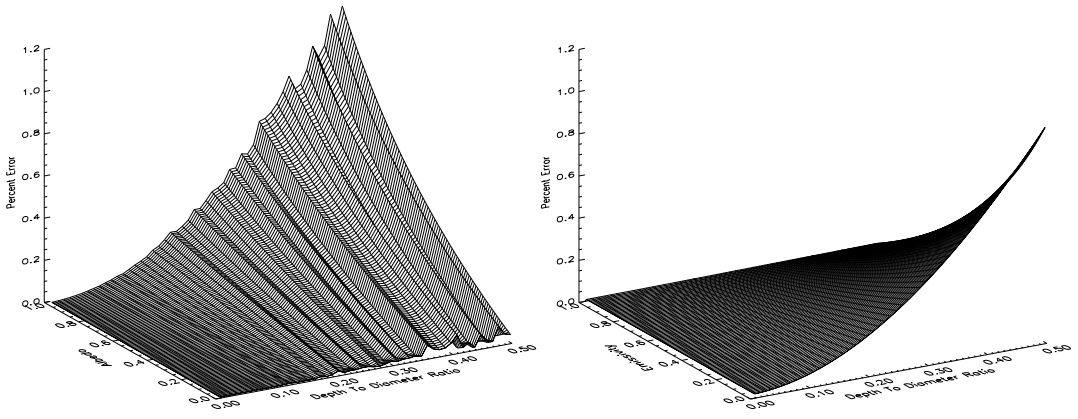

Figure 3.7: The numerical model typically deviates from the analytic solution by less than 1%. The left and right panels show this deviation for short and long wave radiation respectively. The deviation is larger for more highly curved surfaces (higher curvature is less well represented by a series of linear facets) and for more reflective surfaces (higher albedo or lower emmissivity).

The albedo of the CO_2 can be a function of depth. In some model runs we assume that brighter CO_2 underlies a slab of lower-albedo CO_2. We also can assign higher albedos to new CO_2 frost, which formed over the previous winter, than to old frost that was present for more than one year.

The CO_2 ice in which the depression is embedded is assumed to be underlain by water ice. The depth to this water ice layer is adjustable. For some model runs pure CO_2 was simulated by placing the water ice at large depth where it will never be uncovered. When water ice is exposed to insolation (i.e., all overlying CO_2 has sublimated) it is free to warm up and conduct heat into the subsurface. This heat

will partially offset condensation the following winter. Sublimation of the water ice itself is assumed to be negligible at these temperatures and timescales.

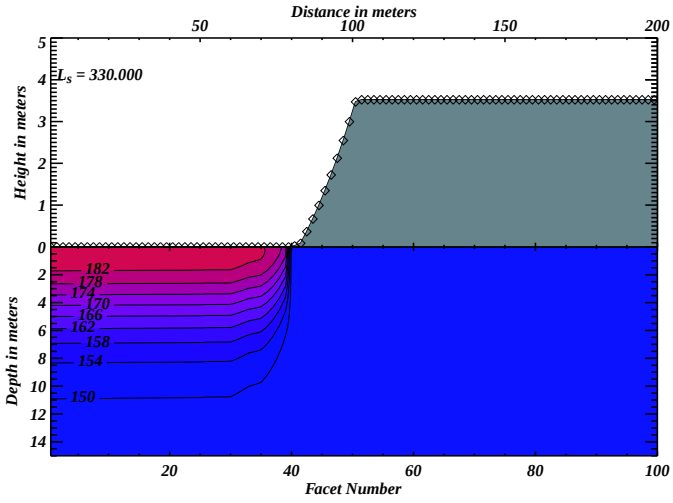

Figure 3.8: Sample model output showing the situation both above and below the water ice surface giving a cross-sectional view from the center of the depression outward. The gray shaded upper deposit is CO_2 ice, whereas the lower deposit is water ice. Temperature contours indicate where the water ice has heated up due to insolation and conduction into the subsurface. Note differing vertical scales for each section of the plot.

The model steps forward in time changing the shape of the depression and updating subsurface temperatures in the water ice at the end of each step. The time step is 1 degree of L_s, generally about 2 days, and we follow the evolution of the features for 10-100's of years. Atmospheric effects have been ignored but we have followed the example of *Jakosky and Haberle* (1990) in assigning an effective emissivity of 0.9 to mimic the contribution of down-welling infrared flux. Figure 3.8 shows an example of the output of one time-step of the model. The limitations of this modeling approach are that the depressions must be cylindrically symmetric and more seriously all facets must be visible from all points within the depression, i.e., no internal shadowing of one facet by another.

3.5 Model results

3.5.1 CO_2 only cases

We first simulate CO_2 ice only cases by placing the water layer at great depth where it will not be uncovered. We experiment with many combinations of albedo and emissivity, which are detailed below. In all cases the albedo and emissivity were chosen so that flat surfaces would return to the same elevation at the beginning of each year.

3.5.1.1 Case 1-Uniform albedo

For the first case we set the albedo and emissivity to the same uniform value for all the facets and the surrounding flat surface. We investigated all physically possible combinations of albedo and emissivity for which the flat surface returned to the same elevation after one full Martian year and varied the initial size and shape of our starting depression. One example of this family of cases is illustrated in Figure 3.9. The initial size and shape of the depression was found to be utterly unimportant to the ultimate fate of the modeled features. The differing combinations of albedo and emissivity affected the rate of change but did not change the behavior of the depression. In all cases the depressions disappeared into the surrounding terrain, i.e., their depth to diameter ratio shrank. This was both due to infilling of the depression by ice and lateral expansion by the depression walls.

3.5.1.2 Case 2-Insolation-dependent albedo

The albedo of the residual cap has been observed to increase during the summer season in response to the increased insolation (*Paige*, 1985; *James et al.*, 1992). We varied the albedo by fitting the observations with a linear relationship, from 0.51 during the polar night to 0.76 at the time of maximum insolation of about 305 W m^{-2}. This range allowed the flat surface to return to its original level when integrated over an entire year. Inside the depression, however, each facet receives a different amount of

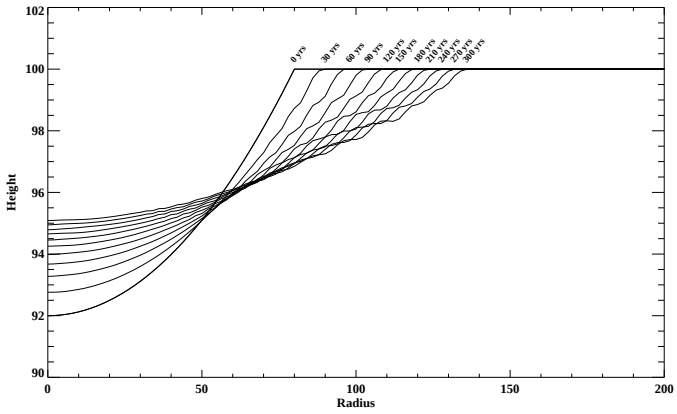

Figure 3.9: Model output for the simplest possible case where the water ice layer is placed at an unreachable depth (100m), albedo is constant for all places within the depression and the surrounding flat surface. Solid lines indicate the starting position and subsequent depression shapes every 30 Martian years. This particular run was started with an exaggerated vertical size to illustrate the point more clearly. In this family of cases features lose definition (become progressively broader and shallower) eventually becoming indistinguishable from their surrounding flat surface.

sunlight and so has a different albedo at different times of the year. Again we found that starting shapes and sizes had a negligible effect on the outcome. The eventual fate of this family of cases is the same as the previous example; the depressions disappeared into the surrounding terrain although this time the rate at which they disappeared was higher.

3.5.1.3 Case 3-Residual frost with low albedo

High resolution MOC imaging shows that the walls of these depressions become extremely dark as the summer season nears its end (*Malin and Edgett*, 2001); examples of this darkening can be seen in Figure 3.4. We varied the albedo so that it became dark after the seasonally deposited layer was removed. Figure 3.10 shows an example where the bright albedo has been set to 0.7 and the dark albedo has been set to 0.5. The depression rapidly expands until the center portion no longer receives much radiation from the walls. The depression continues to expand uniformly; however it keeps its bowl shape and does not develop the flat floor, which is an important distinguishing characteristic of the observed Swiss-cheese features. Varying the initial size and shape in these cases again produced no noticeable effect on the evolution of the modeled depression.

3.5.1.4 Case 4-Low albedo slab with a high albedo substrate

To produce results with flat floors we found it necessary to include a lower volatility substrate. We varied the albedo with depth such that any facets below a certain elevation were constrained to have bright ($\approx$0.7) albedos at all times. Above this elevation is a low-albedo slab whose thickness we varied from 4 to 20 meters and whose albedo we varied from 0.4 to 0.65. The modeled depression was again started from a small surface indentation on the top of the CO_2 layer. Once the bright seasonal frost has been removed the darker albedo ice is exposed to insolation causing this initial indentation to grow toward the clean CO_2 layer in a similar way to that discussed in the previous section. This growth proceeds until the depression encounters the clean CO_2 layer, after which the floor remains flat and the walls continue to move outward.

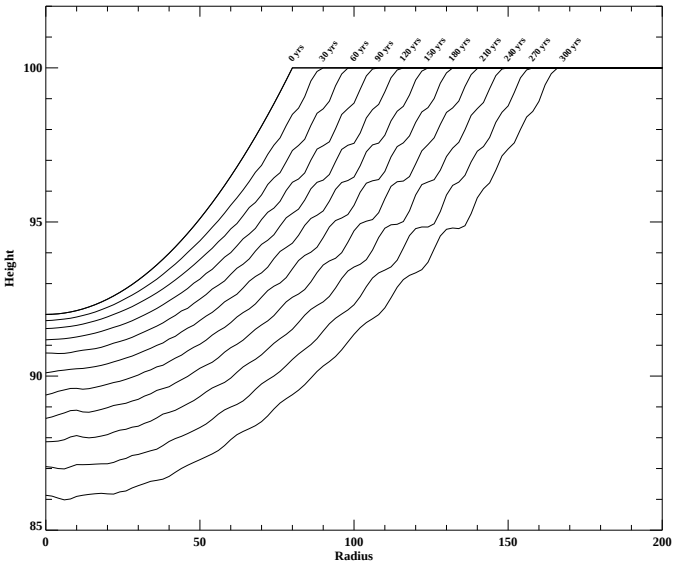

Figure 3.10: Model behavior with condition of dark residual frost. In this case we simulate the observed darkening late in summer by giving the residual frost a lower albedo than the seasonally deposited layer. For the model run shown here the residual ice has an albedo 0.5 and the seasonal frost has an albedo of 0.7. The depressions can now grow in size but they cannot develop the flat floors and steep walls exhibited by Swiss-cheese features.

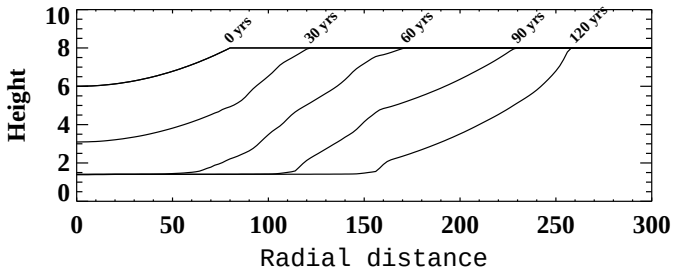

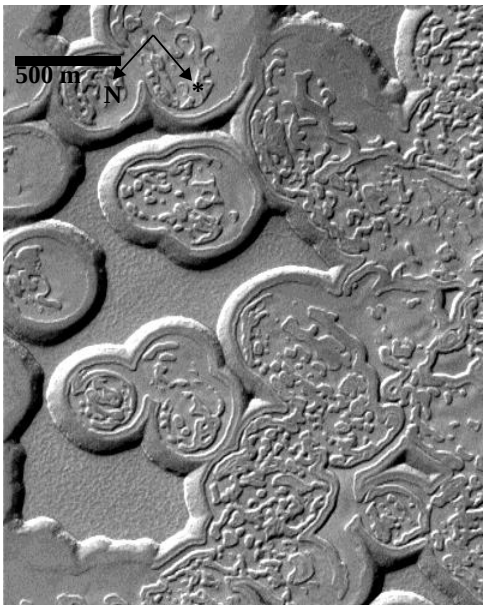

Figure 3.11: a) Model output for the same case as illustrated in Figure 3.10 except that a clean CO_2 substrate is now placed 8 m below the surface. The depression initially grows as before. It develops a flat floor, but it does not develop the steep sides characteristic of the majority of Swiss-cheese features. After 80 Martian years the walls have a slope of only about 3°. b) Sub-frame of MOC narrow-angle image M03/06646, taken at 85.6°S, 284°E, L_s 181°, showing Swiss-cheese features with shallow sloping walls. MOLA height and MOC narrow-angle distance measurements indicate that the poleward facing walls have slopes of about 3°. These shallow slopes are uncharacteristic of the majority of Swiss-cheese features but can also be modeled with this approach.

Figure 3.11(a) shows an example of how a depression grows in these circumstances. The shape more closely resembles observed Swiss-cheese features in that it is flat floored; however the walls maintain their shallow slopes. There are cases (e.g., Figure 3.11(b)) where Swiss-cheese features occur with extremely shallow sloping walls. The walls in this particular location have slopes of about 3° (determined from MOLA height and MOC/NA distance measurements) which match the model results in this case. These walls will eventually steepen to slopes of about 10°.

A single value of residual CO_2 albedo does not appear to be able to mimic all characteristics of Swiss-cheese features. In some limited cases it matches the observations quite well and it may be that the CO_2 slab in these areas is uniform in albedo with depth. However the majority of these features appear to have steeply sloping walls, which in most cases appear to be within the range of 20° to 40°. We will now describe the effects of introducing albedo gradients within the CO_2 slab.

3.5.1.5 Case 5-Decreasing albedo with depth and a high albedo substrate

To simulate the majority of cases where the walls are steeper than 20° we include an albedo gradient within the low-albedo slab of CO_2 ice. Instead of having a single value for the dark albedo of the residual ice it is now a linear function of depth, with its darkest value at the interface between the low-albedo CO_2 slab and the high-albedo CO_2 substrate. The brightest value of the residual albedo is at the level of the surrounding mesa top and its value is set to be equivalent to that of the clean seasonal frost. This albedo gradient could represent an increasing concentration of impurities with depth or perhaps changes in grain size. Figure 3.12(a) shows how albedo varies with depth in this case. The high CO_2 albedo of the seasonal frost was set to a value which insured the surrounding flat surface returned to the same height at the end of each year.

We experimented with various albedo gradients and also varied the thickness of the overlying low-albedo CO_2 slab. Overall the modeled depressions have two life-stages. First the depression grows down to the clean CO_2 substrate as an expanding

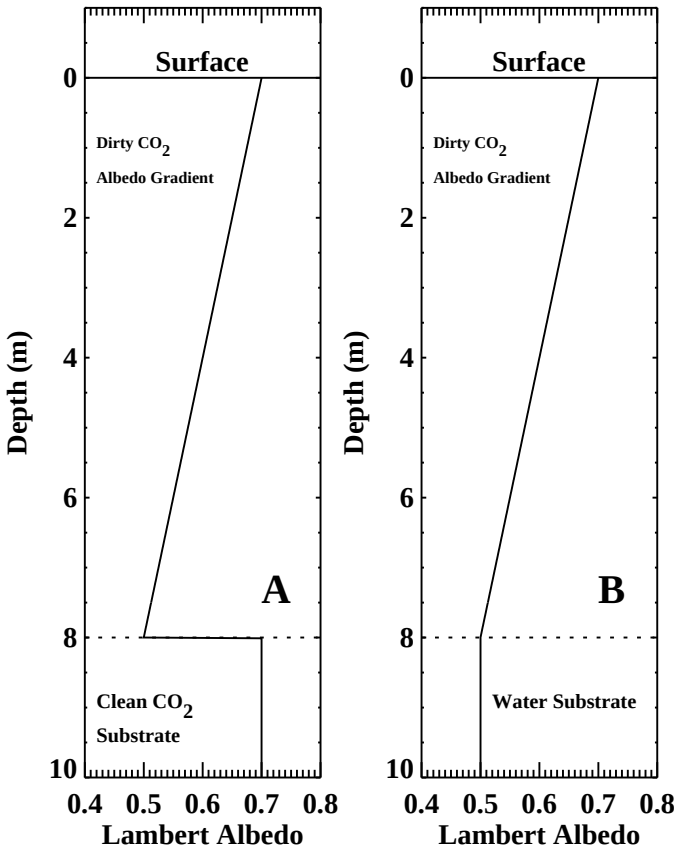

Figure 3.12: Illustration of albedo versus depth for two cases which from which we can successfully reproduce Swiss-cheese features. A) Example of cases discussed in Section 3.5.1.5 with a 'dirty' slab of CO_2 with albedo decreasing with depth, which is underlain by a bright CO_2 layer. B) Example of cases discussed in Section 3.5.2 with a 'dirty' slab of CO_2 with albedo decreasing with depth, which is underlain by water ice layer with no albedo discontinuity.

bowl-shaped feature. The albedo gradient means that the walls grow steeper during this phase. After contact with the clean CO_2 substrate the downward growth stops and the walls continue to steepen as they move outward. During the second stage the walls reach their steepest form and continue to move out at a steady pace. We refer to these two stages as the ramp-up and linear growth stages.

The length of time the depressions spend in the ramp-up phase is directly related to the thickness of the low-albedo CO_2 ice slab. When the slab is 4 meters thick the depressions reach the linear growth phase within 30 Martian years; at the other extreme when the low-albedo CO_2 slab is 20 meters thick the depressions still have not completely reached the linear growth phase after 300 Martian years.

The growth rate observed in the linear growth phase is directly related to the value chosen for the dark albedo. The differing thickness of the overlying CO_2 we experimented with had little effect on this property. Outward growth rates of the walls have a narrow range of 0.5-2.5 meters per year.

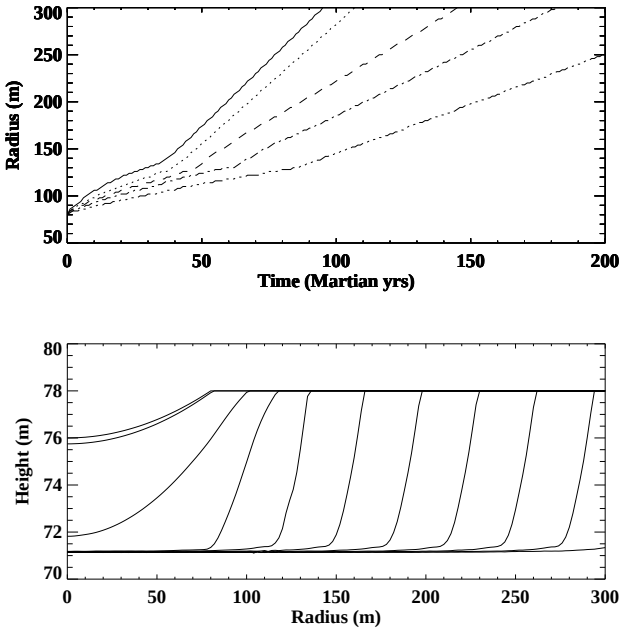

Figure 3.13: Model output for a family of cases with clean CO_2 substrate. Lower panel shows a specific run with dark albedo set to 0.6 and CO_2 slab thickness set to eight meters. Evolution of the depression is shown in cross-sectional view. The ramp-up and linear growth phases are clearly visible. The upper panel shows radius versus time for a family of cases all of which have a CO_2 slab thickness set to eight meters but whose dark albedos range from 0.4 to 0.6. As intutitivily expected darker albedos cause faster expansion.

Figure 3.13 shows a specific example of modeled depressions with an eight meter

slab of low-albedo CO_2 ice above bright CO_2 basement. Shown on the bottom panel are the results from one particular case plotted every 30 Martian years. After 90 years the depression has acquired its final form and has completed what we have termed the ramp-up phase. The rest of the history of the depression is quite mundane as it enters a linear growth phase expanding in radius at an average rate of $\approx$1 m/yr. The top panel shows the increase in radius as a function of time for a family of such cases. In each case the CO_2 slab is 8 m thick. The different lines represent values of the albedo of the upper slab at the interface with the lower (bright) CO_2. Darker albedos lead to faster expansion.

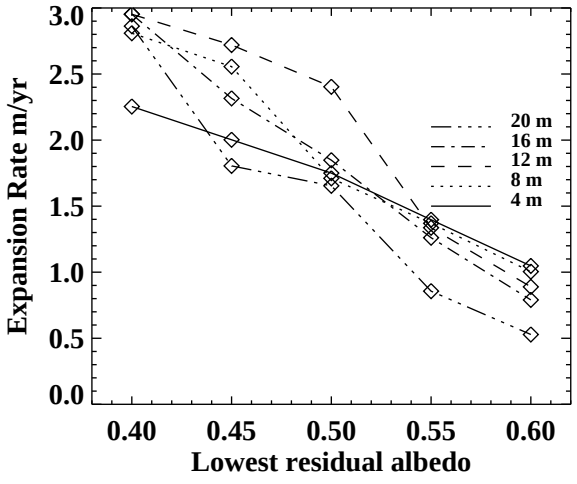

Figure 3.14: Retreat rates for the walls of Swiss-cheese features, as a function of the darkest residual frost albedo. The range of wall retreat rates deduced from this modeling is quite narrow with most values falling between 0.5-2.5 meters per year. The darkest albedo is the albedo of the CO_2 ice where it is in contact with the clean CO_2 substrate. The CO_2 ice albedo increases linearly with height to 0.7 at the upper level surface as described in the text. The trend of higher expansion rates with lower albedo is easily visible.

Figure 3.14 illustrates the dependence of the linear wall recession rate upon the albedo of the CO_2 ice. The albedo in this plot corresponds to the albedo where the low-albedo CO_2 ice meets the high-albedo CO_2 substrate (i.e., the darkest albedo). This albedo value determines the albedo of all facets using the linear scaling described above. The trend of higher expansion rates with darker albedos is obvious although the actual range of expansion rates is quite small. The actual numbers range from 0.5

to 2.5 m/yr which agrees with previous observations by *Malin et al.* (2001) in most cases.

In summary, through a somewhat elaborate variation of albedo with depth, we can reproduce the flat floors and steep walls, the late summertime darkening, and the observed expansion of the Swiss-cheese features. This situation requires a slab of CO_2 getting progressively dirtier with depth but which is underlain by a bright CO_2 substrate. Another method of reproducing these observations is to replace the bright CO_2 substrate with a non-volatile layer of water ice, which we describe in the next subsection.

3.5.2 Cases with a water ice base

We experimented with replacing the bright CO_2 substrate with water ice. The albedo of the water ice substrate was set to the darkest residual CO_2 albedo, so unlike the previous example there was no albedo discontinuity at the contact between the two substances. The behavior of the depressions in this situation is remarkably similar to the bright CO_2 substrate case described above. As before, situations where there is no albedo gradient within the upper slab of CO_2 produce flat floors and shallowly sloping walls. It was necessary therefore to retain the condition of decreasing albedo with depth. For clarity the albedo profile with depth is illustrated in Figure 3.12(b). We experimented with various albedo gradients and also varied the thickness of the overlying CO_2 slab.

Figure 3.15 shows a specific example of modeled depressions with an eight meter slab of CO_2 ice above a water ice substrate. Comparing figures 3.13 and 3.15, we can see differences in how long it takes depressions to begin linear expansion, with the case of a water ice base taking longer.

As before the length of time the depressions spend in the ramp-up phase is directly related to the thickness of the CO_2 ice slab and the growth rate is directly related to the value chosen for the darkest CO_2 albedo, which is shown in Figure 3.16. In general the growth rates are smaller than the clean CO_2 substrate case. The rates

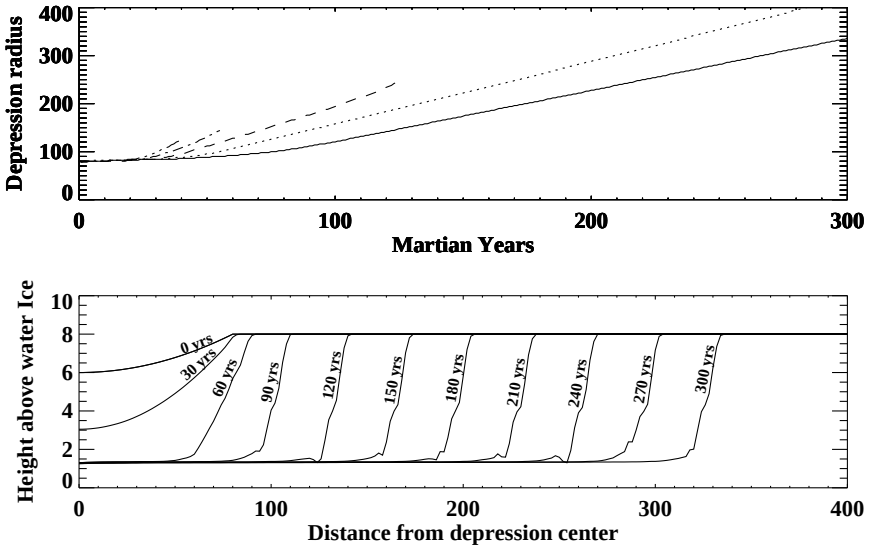

Figure 3.15: Model output for a family of cases with water ice substrate. Lower panel shows a specific run with dark albedo set to 0.6 and CO_2 slab thickness set to eight meters. Evolution of the depression is shown in cross-sectional view. The ramp-up and linear growth phases are clearly visible. The upper panel shows radius versus time for a family of cases all of which have a CO_2 slab thickness set to eight meters but whose dark albedos range from 0.4 to 0.6. Model runs were truncated at 300 Martian years but some runs failed before this point due to instabilities in the model. In all cases the depressions progressed to the linear growth phase and their behavior was well established before the model run ended.

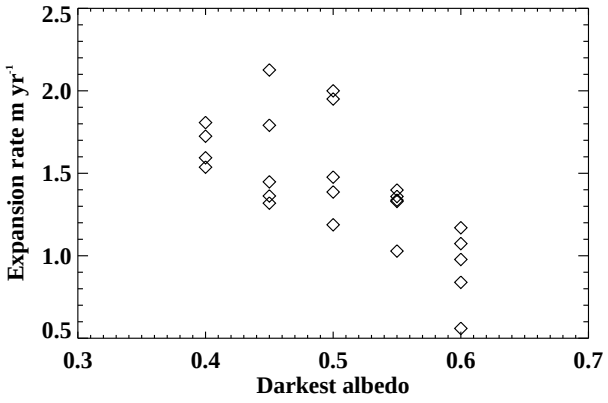

Figure 3.16: Retreat rates for walls of Swiss-cheese features, as a function of the darkest residual frost albedo in the case of a water ice substrate. Similarly to Figure 3.14, retreat rates are found to depend on the darkest albedo values within the dirty CO_2 slab. The overall range of values is narrower that the clean CO_2 only case.

from both cases are close enough however that it would be very difficult to distinguish between them using MOC narrow-angle imaging. The clean CO_2 substrate produces higher expansion rates due to the extra visible light reflected from the bright floor. This can more than compensate for the extra infrared flux produced by the warmer water ice substrate.

3.6 Thermal observations from TES and THEMIS

To distinguish between a water or CO_2 ice substrate, one needs to observe the temperature of the floors of the depressions. CO_2 ice will always remain at the sublimation temperature because it is in contact with the atmosphere. At the pressures on top of the south polar cap, this temperature is ≈ 142 K. Water ice is not subject to this constraint, and when it is exposed in late summer ($310^\circ \leq L_s \leq 350^\circ$), its temperature will rise. The maximum brightness temperature occurs at L_s 320°. We can predict the temperature fluctuation of an unresolved thermal measurement by assuming a fraction of the field of view that is occupied by warm floors verus the cold surrounding upper surface.

This predicted temperature fluctuation for the case of an unresolved thermal measurement is modest and is illustrated on the top panel of Figure 3.17. We have

examined the TES data for mapping year 1 of a region on the south residual cap, 86.5°-87.0°S and 345°-360°E (See Figure 3.17). In general we see large swings in the reported surface temperature due to atmospheric dust loading. The temperatures observed allow for warmer areas on the residual cap; however, they may also be totally due to radiation from the dust suspended above the polar cap. It is very difficult to retrieve surface temperatures when the surface is colder than the overlying atmosphere. The TES data do not rule out the formation of small warm spots on the residual cap surface. The pixel size of TES pre-mapping data or Viking IRTM data is very much larger than that of the TES mapping data and seeing any temperature increase in those datasets would be unlikely.

The thermal emission and imaging system (THEMIS), (Christensen et al., 2002) has pixel sizes of 100 meters and should be able to directly observe the temperature difference between the floors of the Swiss-cheese features and the surrounding upper surface. Unfortunately THEMIS began acquiring data only about $L_s \approx 330°$, whereas we predict maximum surface temperatures at L_s 320°. Figure 3.18 shows the THEMIS coverage accquired before the onset of southern winter. The number of frames which include the residual cap is small (four) and some are so noisy that they can only be used to demark the edge of the CO_2 deposit. In addition there were problems of thermal drift within the instrument which cause the reported temperature to drift to higher values even over isothermal surfaces and a correction for the contribution of the atmosphere has not yet been effectively done. Despite these problems the THEMIS data (in the frames where signal to noise is high enough) are reliable in distinguishing relative temperature differences. The absolute temperature calibration remains suspect however.

Figure 3.19 shows the earliest available (closest to maximum thermal contrast) THEMIS image with a MOC image of the same area. The blue (cold) area at the bottom is the edge of the residual CO_2 ice cap. The red area is too warm to be CO_2 ice. The MOC image shows that the cold arc in the middle of the warm area is an extended mesa top, with the characteristic scalloped sides where the circular depressions have eaten into the walls. In this place, at least, one has a set of circular

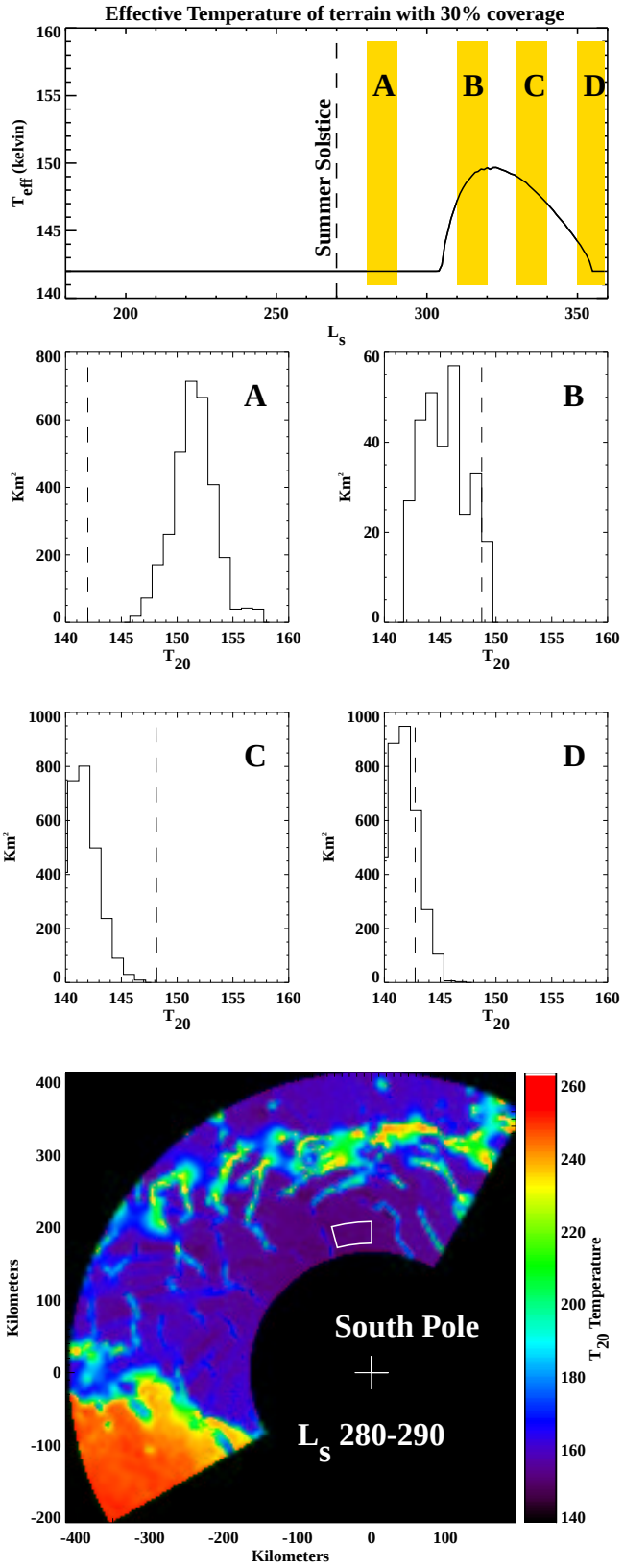

Figure 3.17: Simulated TES temperatures compared with actual data. The top panel shows the expected temperature that a thermal instrument which does not resolve individual depressions would be expected to make. The yellow bars highlight time periods which are examined in subplots below. We examined temperature data in the region 86.5°-87.0°S and 345°-360°E. Histograms of temperature are shown for each time period. The vertical dashed line on each subplot shows the mean predicted temperature for that period. The bottom panel shows the temperatures over the entire residual cap at one particular time period with the examined area indicated by the white outline.

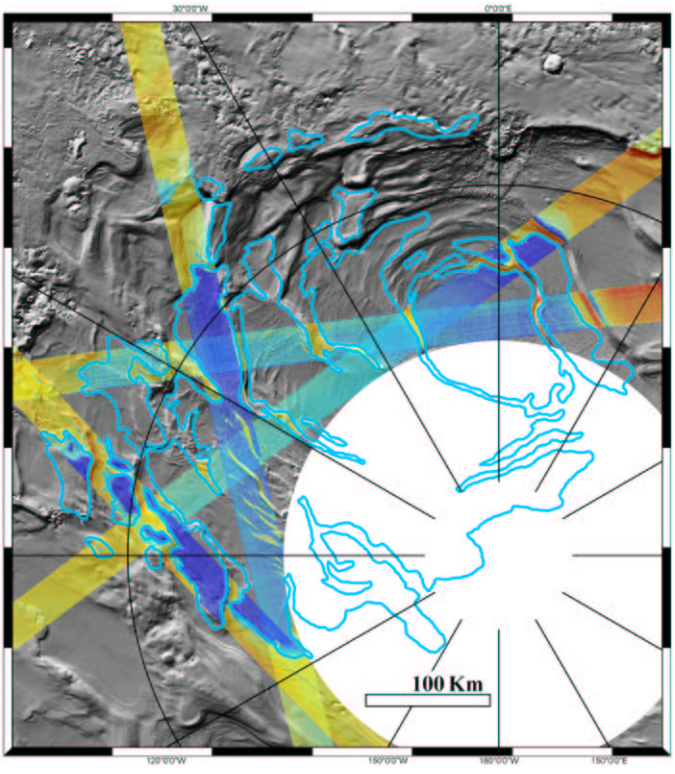

Figure 3.18: Due to the season of arrival of the Mars Odyssey spacecraft, the THEMIS instrument was able to acquire only 4 infrared frames covering the residual cap before the begining of southern winter. Image numbers are I00826006 (L_s 330°), I00910002 (L_s 334°), I01162002 (L_s 345°), and I01246004 (L_s 349°). The residual cap as mapped by *Tanaka and Scott* (1987) is outlined here in blue.

depressions whose floors cannot be CO_2 ice, due to their elevated temperatures, and whose mesa tops almost certainly are CO_2 ice. These observations favor the model of a substrate of water ice beneath a thin (≈10 m) slab of CO_2 ice. We consider it unlikely that there is a buried CO_2 ice reservoir beneath the water ice, as heat conducted down through the water ice will cause buried CO_2 to sublime (*Ingersoll*, 1974).

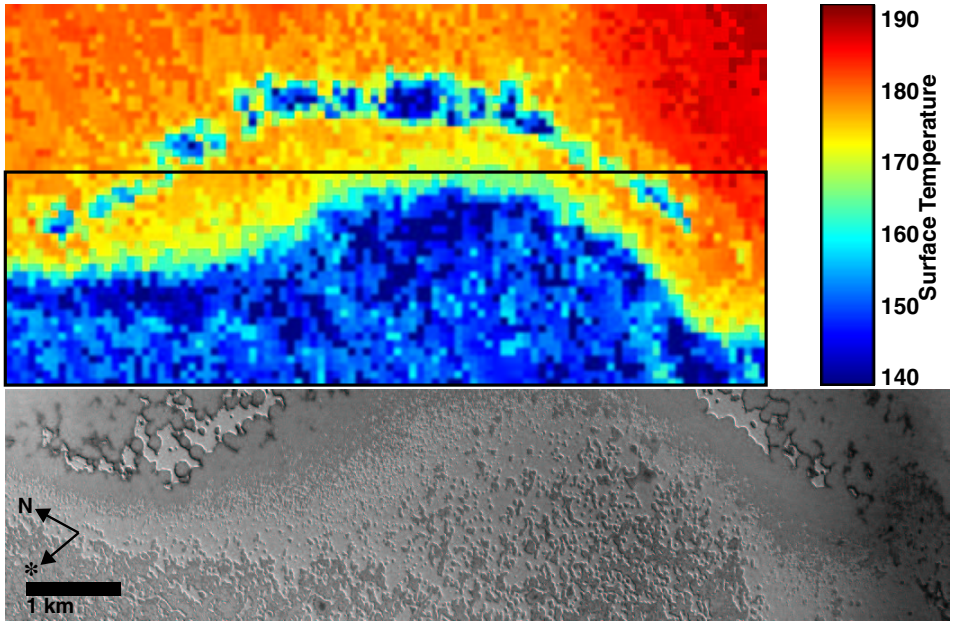

Figure 3.19: Example of these features observed by THEMIS (I00826006) at the cap edge near 84° S, 283° E, L_s 330°. Top panel shows temperatures derived from THEMIS radiance measurements in a 10x5 km area. Boxed area corresponds to subframe of MOC narrow-angle image M03/04994, shown in the bottom panel. Cold material corresponds to the CO_2 mesa-tops, and warm material corresponds to terrain surrounding the mesas and making up the floors of the depressions. These data rule out clean CO_2 ice as the substrate in this area.

In most of the residual cap only isolated remnants of an 8 m thick layer are visible in the process of being eroded by Swiss-cheese features. Most of these Swiss-cheese features belong to the second class of features described in Section 3.3, i.e., displaying the moats and raised central island evident in Figure 3.2. Figure 3.20 shows one isolated 8 m thick section being eroded by members of this class of Swiss-cheese features. The associated THEMIS temperature data show the moats penetrating to

an underlying warmer layer, which because of its elevated temperature cannot be CO_2 ice. We interpret this layer to be water ice. These THEMIS data show that they are similar to other Swiss-cheese features in that a non-CO_2 layer also underlies them. Figure 3.20 shows that the water ice is exposed mostly on the southern parts of the moats, which are the parts that receive the most sunlight. This could be because the southern walls lose CO_2 faster or because the flat floors adjacent to these walls accumulate CO_2 more slowly (since these walls are equatorward facing and steeper they reflect more sunlight towards their moats). In Section 3.9 we speculate on reasons behind the central CO_2 island.

Much of the rest of the residual cap appears to be covered in a relatively thinner CO_2 layer about 2 m thick. This thin layer is itself being eroded by smaller Swiss-cheese features.

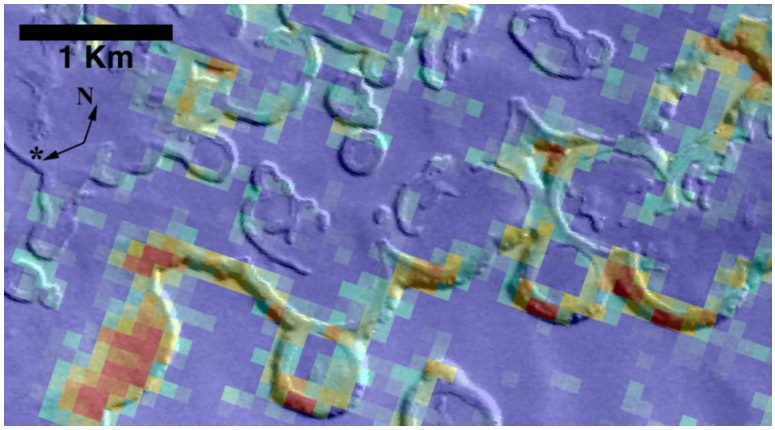

Figure 3.20: Example of Swiss-cheese features observed by THEMIS (I01162002) at 86.5° S, 285° E, and L_s 345°. Brightness here is provided by an underlying MOC narrow-angle image (E05/02715 at L_s 185°), while color represents THEMIS temperatures. Direction to sun applies only to MOC image. The reported temperatures range from 150K to 160K (blue to red). Uncertainties in instrument calibration at such low radiances and atmospheric conditions make the absolute temperatures difficult to retrieve, but temperature differences are reliable. The warmer areas correspond to the floors of the depressions near the walls (moats). These warmer areas, which cannot be CO_2 ice, are concentrated around the sun-facing (south) sides of the depressions.

Swiss-cheese features are ubiquitious throughout the residual cap. We have demonstated two possible ways to produce this distinctive morphology with either an espically clean CO_2 or water ice substrate. Where we have THEMIS observations of sufficient quality they show that it is water ice which underlies these features. We believe it is a safe generalisation that all Swiss-cheese features are underlain by water ice. Confirmation of this will have to wait until the end of the second southern summer of THEMIS observations (see Figure C.1) in early 2004.

3.7 Implications for the solid CO_2 inventory

A central tenet of the *Leighton and Murray* (1966) model is that the atmospheric CO_2 is buffered by a much larger reservoir of solid CO_2. However, a CO_2 residual ice cap with an area of 88,000 km^2, thickness of 10 m, and density of 1.6 g cm^{-3}, would contribute only 0.36 millibar of additional atmospheric pressure if it completely sublimed. This is roughly 5% of the average surface pressure and much less than the seasonal variation. Therefore, unless there is an additional subsurface reservoir, the south residual cap cannot buffer the atmosphere during periods of high obliquity, and the atmospheric CO_2 partial pressure cannot be much larger than its current value.

There may be a substansial subsurface reservoir of CO_2 adsorbed on grains within the regolith. *Fanale and Salvail* (1994) investigated the partitioning of CO_2 between the atmosphere, regolith and polar cap over geologic time, including effects from changing obliquity, atmospheric sputtering, and changing solar luminosity. They found that the quantity of CO_2 adsorbed in the regolith did not change appreciabily with time, due to competing effects of higher temperatures (which reduces the adsorbtive capacity of the regolith) and higher atmospheric pressures (which tend to increase its adsorbtive capacity). The insignifance of the polar reservoir places a strict limit on how much the atmospheric can increase without using adsorbed CO_2. This may mean that the adsorbed regolith plays a more important role than previously appreciated. In light of this new constraint these calculations will have to be redone before any definitive statements on the role of the adsorbed CO_2 in the regolith can

be made.

3.8 Population statistics of Swiss-cheese features

To deduce some short-term historical information about the residual cap, results of this modeling were applied to a population of Swiss-cheese features. We choose a study region (indicated on Figure 3.21) of 400 km^2 located close to the highest elevation on the residual cap. In many areas of the residual cap the Swiss-cheese features have entirely coalesced and removed all the intervening flat upper surfaces. In contrast, the Swiss-cheese features located in our study area have areas of undisturbed surface between depressions so their sizes can be measured (see Figure 3.22). In this regard this subset of the total Swiss-cheese feature population is unique. None of the features in this area show evidence of moats and all are similar in appearance to the archytype shown in Figure 3.1.

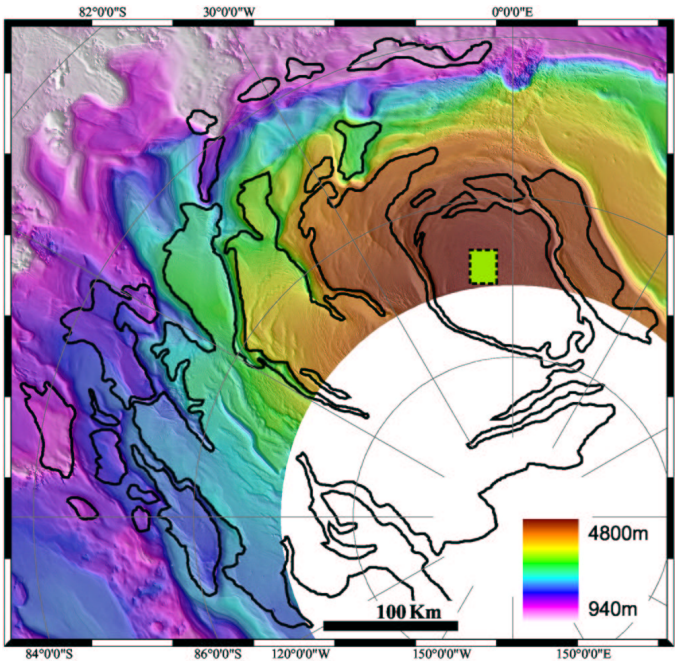

Figure 3.21: Shaded topographic map from MOLA of the southern residual cap (outlined in black (*Kolb et al.*, 2003)). Data poleward of 87° S (white areas) is very sparse and not shown here. The region of interest discussed in this work is outlined by the dashed square near 87° S 355° E.

We combined 17 MOC narrow-angle images together to cover 375 km^2 (94%

of the region outlined in Figure 3.21). The resolution of these frames ranged from 1.4 to 12 meters per pixel. Swiss-cheese features were measured by marking line segments on the images to represent their diameters or, if significantly non-circular, their longest axis (see Figure 3.1). Only features with greater than 270° of intact azimuth were measured. Groups of features that had merged into amorphous shapes were not recorded. Center position and effective diameter were extracted from the line segments for analysis. Figure 3.22(c) shows a typical scene within our study area containing both isolated and merged depressions. We also measured the preferred pointing direction by drawing line segments from the cusp on the poleward facing wall (see Figure 3.1) through the center of the depression. In general this was harder to measure since the cusps are only visible in the higher resolution images and many depressions are too circular to confidently identify the cusp position. For these reasons the number of features that have measured azimuths is much less than the number that have measured sizes.

We measured the azimuths of 370 features within the study area (see Figure 3.22(a)). As can be seen qualitatively in Figure 3.22(c), the cusps are predominantly on the poleward facing walls. The mean orientation is almost exactly south (0.17° off) and the standard deviation is $\approx 17°$. The north-south alignment of the symmetry axis of these features argues strongly for an evolution connected directly to insolation. Since we are not exactly at the pole, the solar elevation decreases while the Sun is in the south of the sky. South-facing slopes therefore receive less sunlight and lose less mass than other walls of the depression. As the walls expand outward, the material on the south-facing wall is left behind and forms a cusp.

In total we measured the sizes of 1263 features, which we identified as Swiss-cheese features. The histogram of sizes is sharply peaked (see Figure 3.22(b)) with a mean diameter of 217 m and standard deviation of 35m. The narrow nature of the size distribution can also be seen qualitatively in Figure 3.22(c).

Wall retreat rates ranging from 0.5-2.5 m/yr are possible with different subsurface albedo conditions (see scction 3.5). The sensitivity of the expansion rate to the albedo of the subsurface material introduces a large degree of uncertainty in trying to date

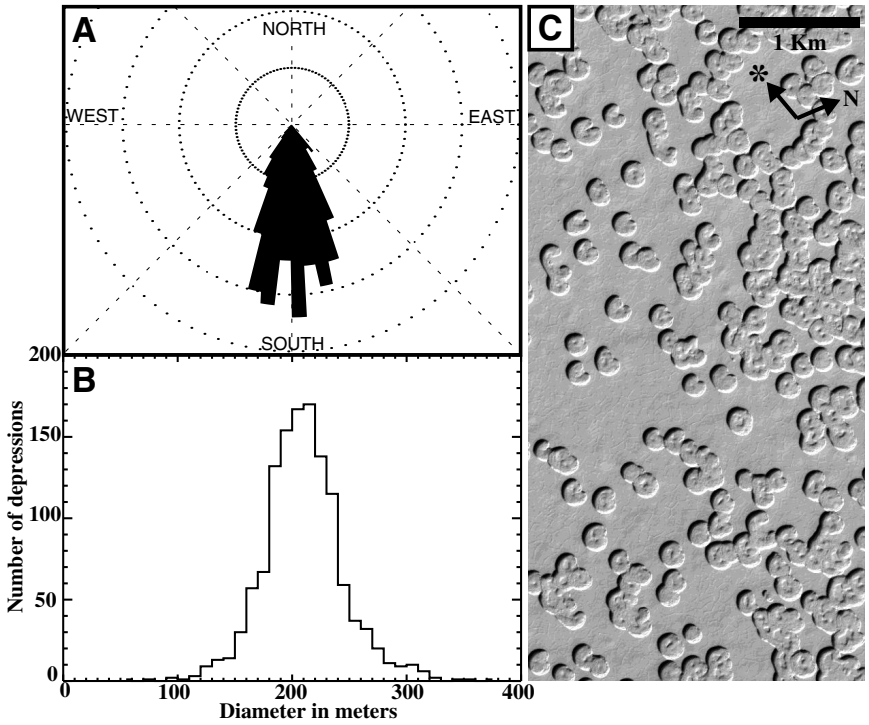

Figure 3.22: A) Rose diagram of Swiss-cheese feature orientations. The total number of features measured was 370, the mean azimuth from the cusp to the center was within 0.2° of south and the standard deviation was ≈ 17°. Concentric circles indicate number in increments of 10. B) Histogram of diameters of identifiable Swiss-cheese features. The total number of features measured is 1263, the mean size was 217m and the standard deviation was 35m. C) Many Swiss-cheese features destroying the upper 8 m thick layer in a sample view of our study area. Sub-frame of MOC narrow-angle image M07/04167, taken at 86.8° S, 355° E, and L_s 211°.

these features. Differing concentrations of dust and other impurities within the CO_2 ice from area to area could result in differing expansion rates so Swiss-cheese features of the same age in different locations may not be of equal size and vice versa. We will assume that the relationship between albedo and depth is consistent over our region of interest (20 km $\times$ 20 km), i.e., that dust co-deposited with the CO_2 slab was uniformly distributed. This seems reasonable, as this region is small and mostly flat with no large-scale obstacles to preferentially concentrate atmospheric deposition. Any variations in ice albedo would serve to create a wider spread of observed sizes.

Using the mean diameter of the population (217m) and the range of expansion rates quoted above we find the age of this population could range anywhere from 43 to 217 Martian years (or 81-408 terrestrial years). Interestingly since the range of sizes is narrow the range of ages is also narrow. The absence of smaller and larger depressions indicates that there was a finite period (which has since ended) where new Swiss-cheese features on this part of the residual cap were initiated. We can attempt to estimate the duration of this Swiss-cheese feature formation period from the width of this distribution. We can choose the inter-quartile scale (40m in this case) to represent the width of the distribution. This range of sizes represents a spread in starting times of 8 to 40 Martian years (15 to 75 terrestrial years), which again depends on the expansion rate.

The large spreads in the mean population age and length of the formation period are largely due to the large range of possible expansion rates. These uncertainties are correlated though; we can say that the length of time over which these features were forming is about 18% of the mean age of the population.

Shallow bowls are also found in this location (See Figure 3.1) and may be currently forming Swiss-cheese features. However, no intermediate cases between the shallow bowls and the fully formed flat-floored pits are observed. It may be that we seeing the genesis of another Swiss-cheese features population after an apparent hiatus in new feature formation of at least several decades. However the lack of intermediate cases means that it is difficult to conclusively identify these shallow bowls as Swiss-cheese feature precursors.

3.9 Implications for environmental variability

The narrow distribution of ages for the population of Swiss-cheese features examined in our region of interest indicates that they all began forming close together in time compared with their overall lifetimes. The lack of smaller and larger features in the size distribution indicates that conditions suitable for the initiation of these features existed for some finite period of time, before and after which no new features formed. The switching mechanism between forming and non-forming periods is uncertain; these timescales are too short to be associated with orbital change and the atmosphere itself has very little memory even on annual timescales (*Liu et al.*, 2003). One possibility is perhaps the slow redistribution of dust on a regional or even planet wide scale into preferred areas, which changes the albedo pattern with respect to the (by comparison) invariable elevation pattern. Changing the distribution of warm areas on the surface could possibly switch the climate and circulation patterns into some other mode leading to differing conditions on the residual cap and a resetting of dust to its original configuration. Averaged over Martian millennia this behavior could be considered to be steady state.

In our modeling we have tuned the albedo of flat surfaces to return to the same elevation at the end of each year. If this condition were relaxed, then CO_2 ice could acuminate on flat surfaces. CO_2 could be effectively redistributed from within the Swiss-cheese features to flat areas elsewhere on the residual cap in this way.

The raised islands and moats within the larger Swiss-cheese features present other problems. Once water ice is exposed at the surface it becomes very hard to cover it again with enough CO_2 to last the whole year without changing the environmental conditions (*Jakosky and Haberle*, 1990). One possible explanation is that the larger depressions initially formed in a similar way to the smaller depressions. Some environmental change allowed a few meters of CO_2 and dust to settle in their centers. Recent (a few Martian decades to centuries ago) environmental change in the opposite sense could make exposed water ice remain exposed. If the walls were retreating throughout these periods (perhaps at varying rates), then the retreat since the last

environmental change would leave a moat of exposed water ice. Figure 3.23 illustrates this possible history.

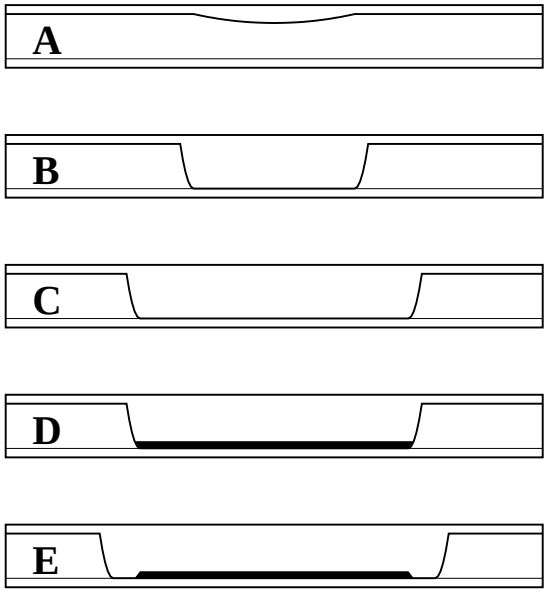

Figure 3.23: Possible formation scenario for the larger Swiss-cheese features and their associated moats shown in cross-sectional view. The depression grows initially like the smaller ones we have modeled (A-C). Growth stops due to some climatic perturbation and the depression begins to infill with a CO_2 ice and dust mixture (D). Finally after an unknown period of time the climate reverts to its previous condition and the walls begin to move outward again, leaving the recent central deposit as an island surrounded by a moat. The widths of the moats and their present day expansion rate indicate this last event occurred a few Martian decades ago.

Alternatively moats may just be a property of large Swiss-cheese features where the center no longer feels any appreciable radiative effect from the walls. In this picture exposed water ice on flat surfaces would currently be prone to being covered by year-round CO_2 but the extra radiation reflected from the walls of the depression could create a small zone where the opposite is true.

3.10 Acknowledgements

This work was made possible by funding from the Mars data analysis and Mars fundamental research programs. Thanks to the MOLA team (especially Greg Neumann) for such great access to their data and Ken Tanaka and Eric Kolb who provided the

outline of the residual cap. Thanks to Norbert Schorghofer for prompting the size measurements and providing comments.

Chapter 4

Evidence of deformation at the margin of the south polar layered deposits

4.1 Abstract

Recent topography measurements confirm that the layered deposits in both hemispheres are several kilometers thick. Although the internal temperature and basement topography of the ice sheets are uncertain, it seems likely that flow is occurring today at rates of millimeters to centimeters per year with enhanced flow rates during periods of higher obliquities. In this work I examine geomorphologic indicators of flow processes at the edge of the southern layered deposits. Indications of multiple episodes of previous flow are seen. However, much evidence of brittle processes such as faulting, slumping and landsliding is also present. This leads to the conclusion that at present flow of the layered deposits is incapable of relieving the gravitationally generated stresses within the ice sheet. It appears that although periods of flow occur, we are likely not within one of those periods at present.

[1]Material in this chapter is the subject of ongoing research and will be submitted as Byrne, S., **Deformation at the margin of the south polar layered deposits**, *Journal of Geophysical Research*, 2003.

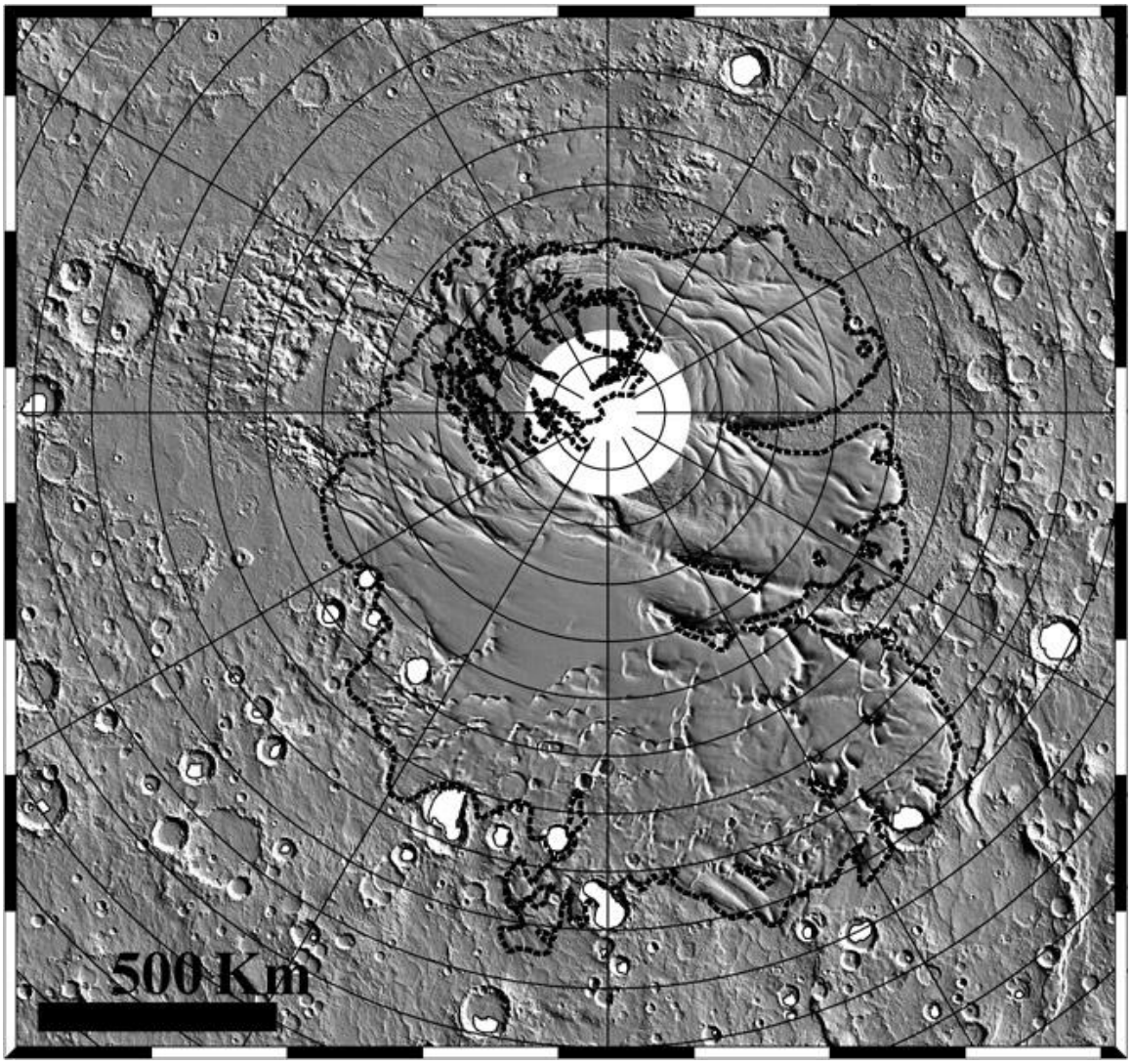

Figure 4.1: MOLA derived shaded relief map of the south polar region. Grid lines every 2° latitude and 30° longitude, shading from upper right. White areas indicate mapped locations of mounds within craters interpreted to be layered deposit outliers. White circle within 87°S represents no data, black dashed line represents the mapped boundary (*Tanaka and Scott*, 1987) of the layered deposits.

4.2 Introduction

The Martian layered deposits have long been thought to be mostly water ice with varying admixtures of dust leading to the differing albedos and mechanical properties of the layers (*Murray et al.*, 1972; *Cutts*, 1973b). They have previously been mapped as a distinct unit based on their banded visual appearance (*Tanaka and Scott*, 1987). Topography data from the Mars Orbiter Laser Altimeter (MOLA) (*Smith et al.*, 1999) have confirmed these deposits to be several kilometers thick and broadly dome shaped, similar in at least that respect to the Greenland ice sheet on Earth.

The degree to which the present layered deposits behave like terrestrial ice sheets is unknown (*Clifford et al.*, 2000). The possibility of flow has been discussed for the northern polar layered deposits by many authors (*Budd et al.*, 1986; *Fisher*, 1993, 2000; *Fisher et al.*, 2002; *Greve*, 2000; *Greve et al.*, 2003; *Nye*, 2000) and for the southern deposits by *Head* (2001). Conversely brittle fracture and sublimation have been proposed to dominate over flow by others (*Ivanov and Muhleman*, 2000; *Murray et al.*, 2001).

In this work, features at the edge of the southern layered deposits are examined for evidence both for and against flow. Section 4.3 details the evidence for flow. Contradictory evidence of brittle processes is detailed in Section 4.4 after which I conclude and outline what future direction this work will take. The material in this chapter is work in progress and its continuation will be a focus of my postdoctoral studies.

4.3 Evidence of ice flow

A series of craters close to the mapped edge of the south polar layered deposits contain large mounds (see Figure 4.1). These mounds appear to be outliers of layered deposit material in MOC narrow-angle images; some have previously been mapped as such (*Tanaka and Scott*, 1987) on the basis of Viking imagery. There is a tendency for these deposits to lie against the equatorward facing (south) sides of the craters in which

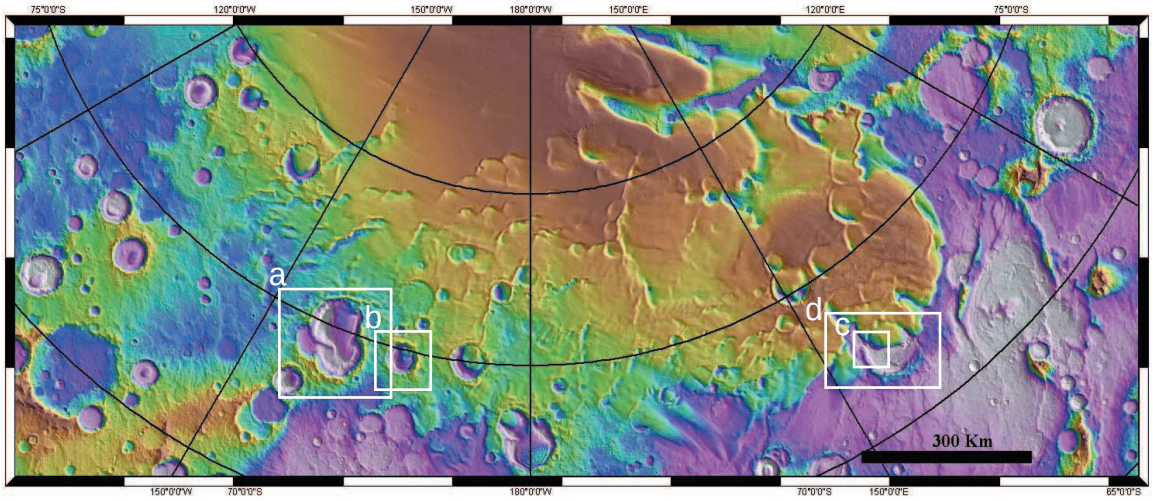

Figure 4.2: Context figure showing the northern edge of the south polar layered deposits with location of subsequent figures indicated. The Ultimi lobe is the region between longitudes of 130°E and 150°E. The regions shown in subsequent figures are indicated by the white boxes.

they reside which indicates they are probably currently eroding due to sublimation. Many of these mounds show geomorphic evidence of flow at some point during their history some of which is discussed below.

4.3.1 Compressional ridges

A common occurrence where these mounds are in contact with a crater wall are ridges at the edge of the deposit (see Figure 4.3). I interpret these ridges as being due to compression of the ice mass as it flowed into the side of the crater. It is possible that this form of compression could also occur from the ice being pushed uphill by the pressure of the mound upstream. I interpret the present day separation between the crater wall and postulated terminus to be due to subsequent retreat of the ice by sublimation. Many of these mounds have dunefields superposed on them, care must be taken that large dune formations are not interpreted as ridges within the ice body. MOC narrow-angle imagery provides the distinguishing data.

The history of the feature depicted in Figure 4.3 is possibly very complex. The expected initial formation mechanism for polar layered deposits is atmospheric de-

position of water ice with varying amounts of dust being co-deposited. This process would be expected to operate equally well inside two neighbouring craters. However in Figure 4.3 we see what appears to be flow of material from the southern (top) crater to an adjoining northern (bottom) crater. This implies that the northern crater has either been emptied of, or was never filled with, layered deposit material. There is no reason why one of these craters would have layered deposits form in situ and the other would not or why one crater would lose its layered deposits while the neighboring crater did not. The layered deposits therefore must have advanced equatorward into the southern crater. The roughness of the bedrock terrain to the east, west, and north may indicate that the layered deposits did not advance completely over these craters.

4.3.2 Superposed mounds

Many of these mounds appear to be multiple superposed ice masses (see Figure 4.4). It has been argued in the past that the southern layered deposits have advanced and retreated (*Head*, 2001). This is further evidence to that effect, each superposed lobe of material can be interpreted as being the result of the main ice sheet advancing over the previous lobes. Periodic glaciation is common on the Earth and could occur on Mars due to layered deposit formation enhanced by obliquity variations as has been suggested by many in the past (most recently *Greve et al.* (2003)). A similar structure of superposed mounds can be seen in the crater depicted in Figure 4.3.

4.3.3 Terminal moraines

Terminal-moraine-like features point to both lateral advancement of ice masses and to more recent retreat. The evidence for the existence of these features is weaker than other indicators discussed above because they are in general harder to locate (see Figure 4.5) and presumably are easier to destroy due to their small scale.

Advance of the ice sheet is not necessarily due to flow in this location. The arcuate breaks in slope seen at the edge of the layered deposits in Figure 4.5 suggests that

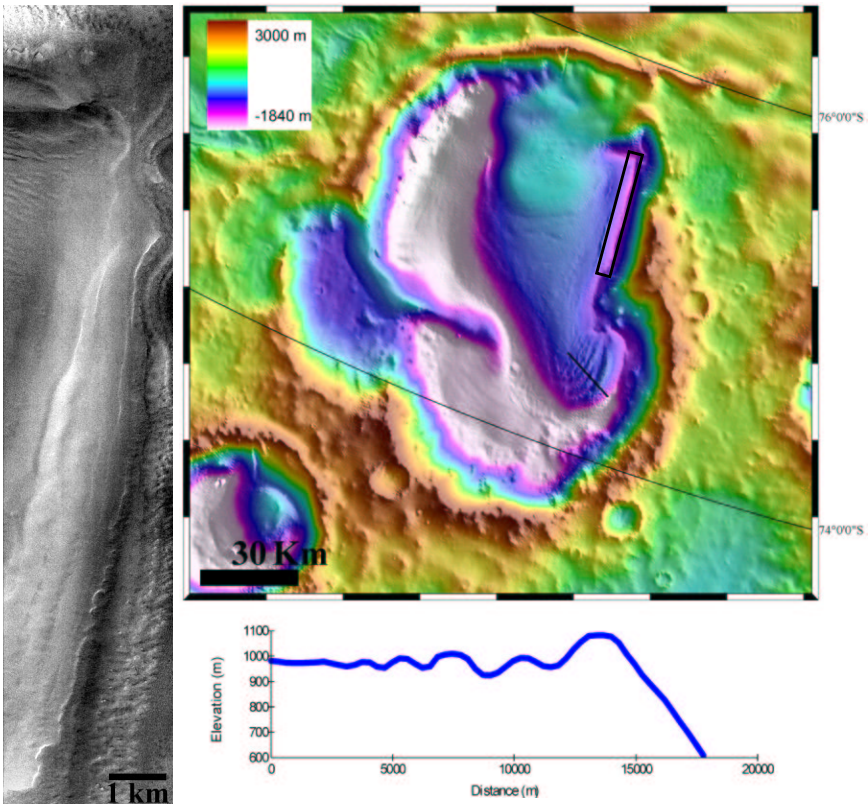

Figure 4.3: Right panel shows MOLA topography (shading from the upper right) of a glacier-like feature within two craters. The black line near the interpreted terminus (below and right of center) represents the position of the plotted topographic profile. A series of ridges is visible near the edge of this feature. Location of this frame marked as 'a' in Figure 4.2. The black rectangle shows the location of the MOC narrow angle frame in the left panel (E16/00609, illumination from the lower right). The MOC image shows the layered deposit nature of this outlier.

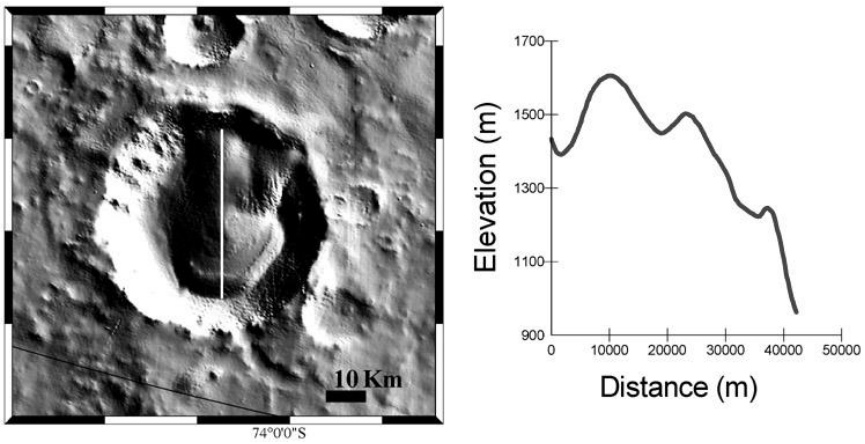

Figure 4.4: MOLA shaded relief of crater containing superposed mounds. White line indicates position of plotted topography profile (top to bottom on Figure is left to right on plot). A single ridge at the edge of the deposit is also visible here. Location of this frame marked as 'b' in Figure 4.2.

slumping has taken place (see Section 4.4.1). It is possible that advancement of the ice sheet in this location is due to this slumping rather than true flow or basal sliding.

4.4 Evidence contrary to flow

Several locations at the layered deposit boundary in the Ultimi lobe region (shown in figures 4.2 and 4.6) exhibit ample evidence of brittle processes (*Murray et al.*, 2001). Offset faulted layers, landslides, and large scale slumping in this area indicate that flow is not currently fast enough to accommodate the driving stresses which cause these features.

4.4.1 Large-scale slumping

The linear slope breaks which parallel the edge of the layered deposits and the the scalloped appearance of the bounding scarp to the east, seen in Figure 4.6, indicate large scale slumping of the layered deposits in this area. Detailed profiles are plotted

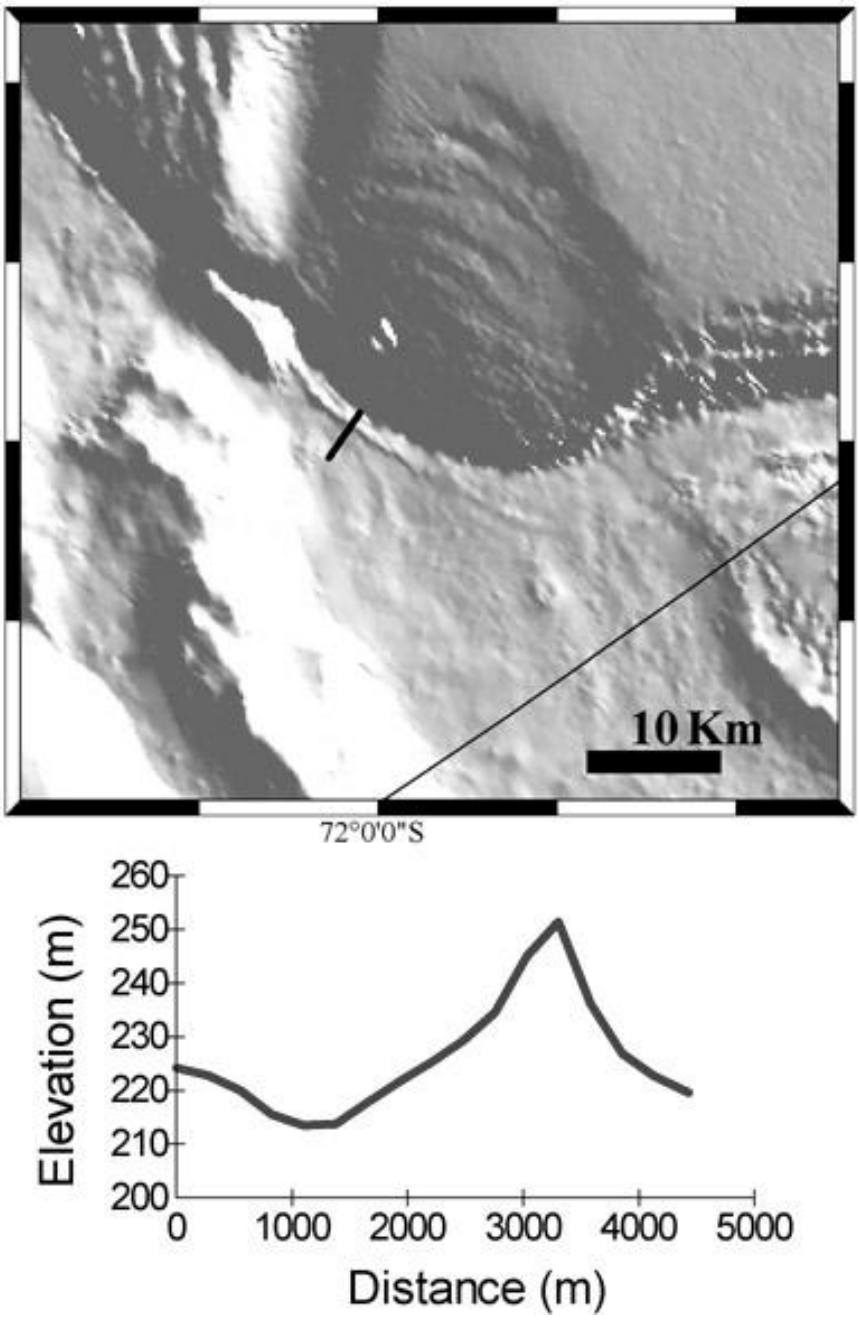

Figure 4.5: MOLA shaded relief near 72°S 145°E. Small moraine like structures are evident in the vicinity of possible flow structures. Black line segment represents the position of plotted profile. Location of this frame marked as 'c' in Figure 4.2.

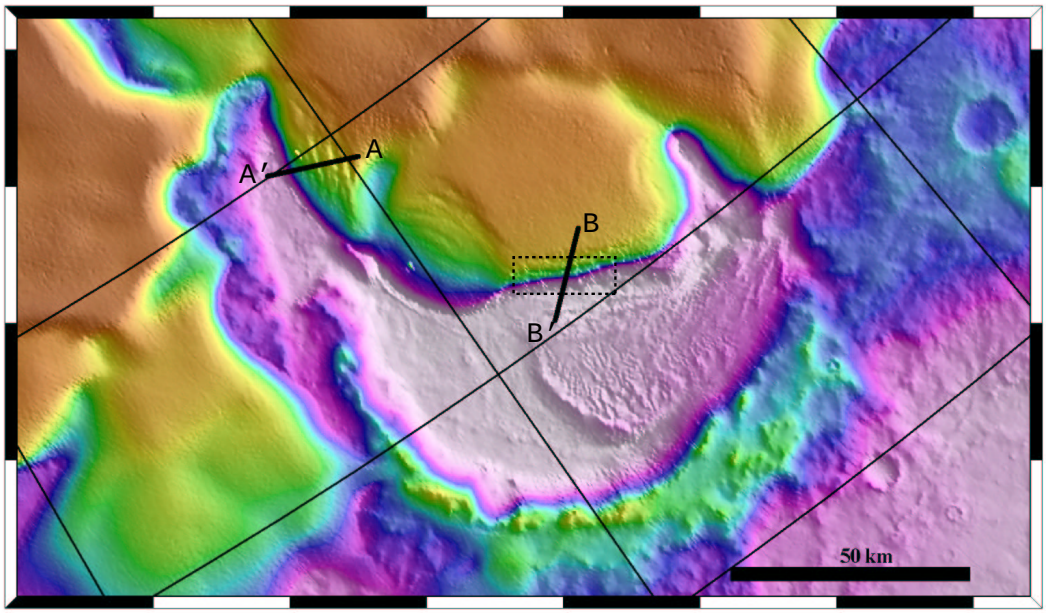

Figure 4.6: Shaded MOLA topography of the northern edge of the Ultimi lobe. The scalloped appearance of the scarp at AA' indicates large-scale slumping. Topography and slope profiles along the line segments AA' and BB' are shown in Figure 4.8. The dashed box indicates the location of the mosaic shown in Figure 4.9. Location of this frame marked as 'd' in Figure 4.2.

in Figure 4.8. Peaks in the along-profile slope indicate the location of these possible slumps.

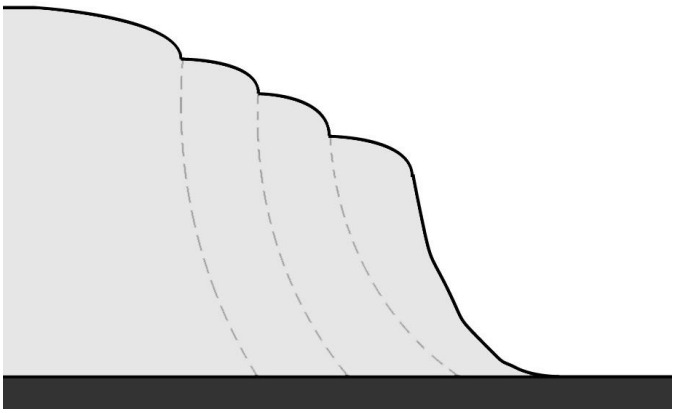

Figure 4.7: Schematic sketch of my interpretation of the situation at the scarp edge (topography shown in Figure 4.8). The breaks in slope as interpreted to be due to rotational slumps along normal faults (shown as dashed lines.

4.4.2 Landsliding

Slope failure is a common occurrence on the Ultimi lobe bounding scarp. Maximum downhill slopes along this scarp exceed 40°, which is well above the angle of repose. Landsliding is not observed at the edge of the south polar layered deposits in other locations (although it is suspected in parts of the north polar layered deposits (*Byrne and Murray*, 2002)). However in general slopes are not as steep in other locations, so there is no reason to suspect that these landslides indicate that the layered deposits themselves in this region are somehow unusual. A break in slope at the bottom of the scarp indicates the presence of mounds of talus.

4.4.3 Brittle faulting

Sections of disturbed layering are common around the edge and near the base of the layered deposits in the longitude range 110°E to 160°E. Figure 4.10 shows some of the more striking examples. The stresses which led to these brittle breaks were most likely gravitationally generated within the ice-sheet; subglacial tectonism cannot be

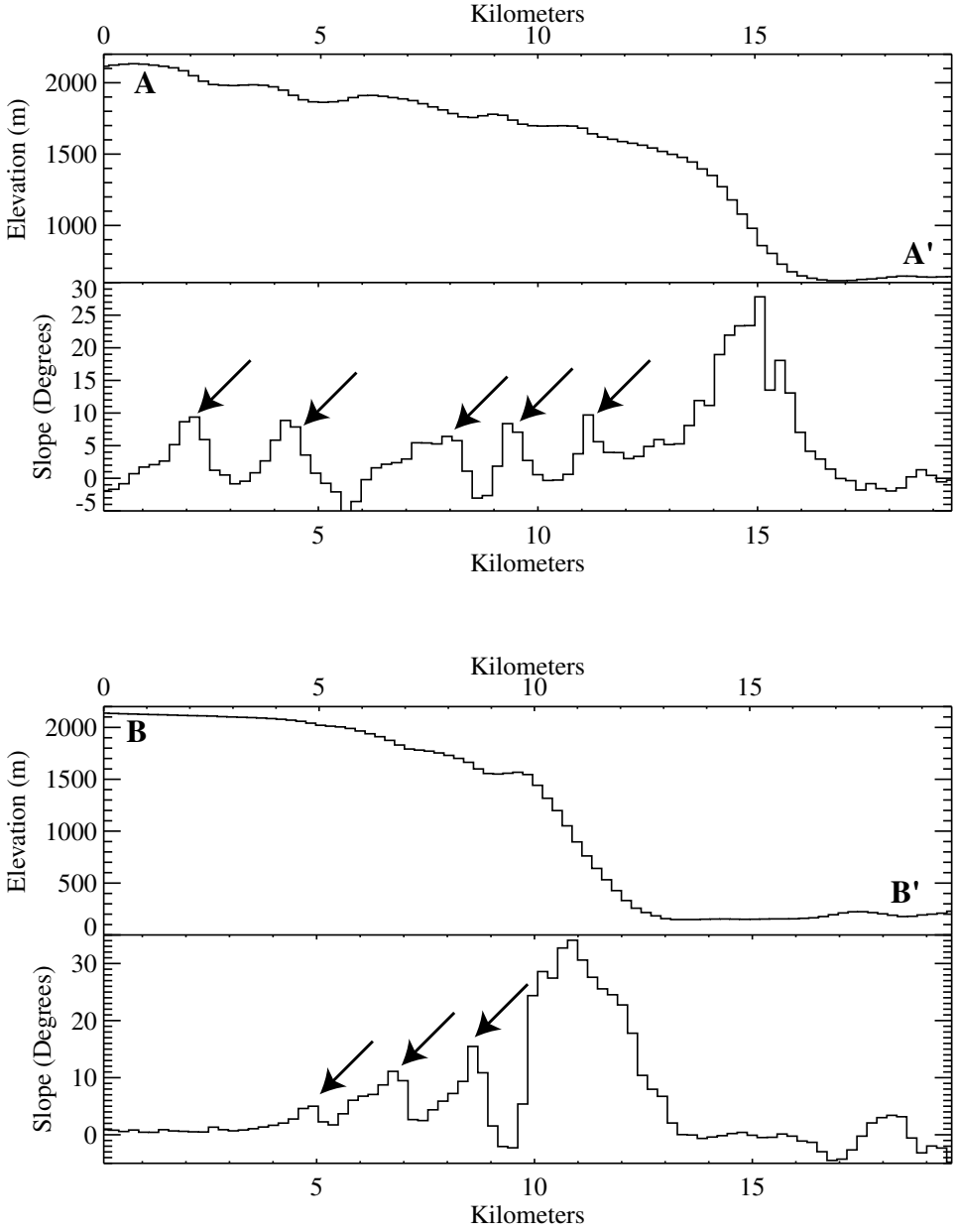

Figure 4.8: Profiles of elevation (and derived along-profile slopes) from differing positions at the edge of the southern layered deposits in the Ultimi lobe region. Figure 4.6 shows the location where these data were taken. Peaks in the slope plots (shown by arrows) indicate where slumping due to normal faults may have occurred.

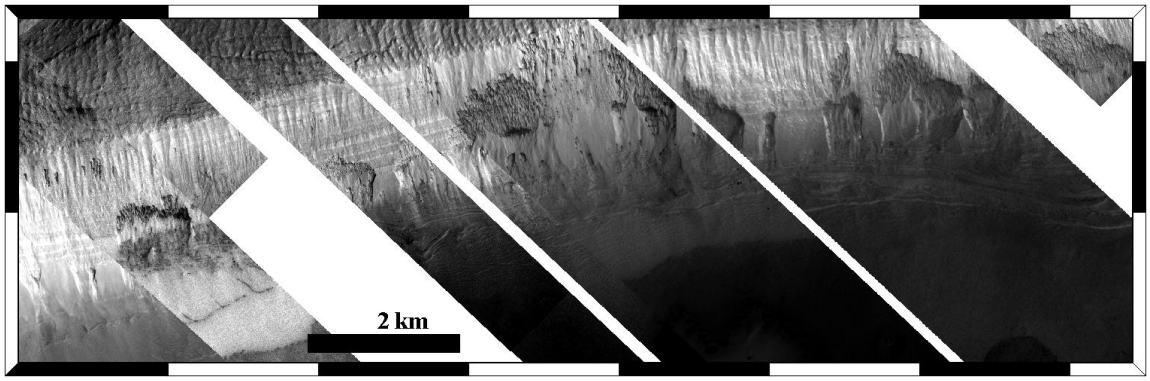

Figure 4.9: Landsliding at the polar layered deposit boundary is common in this area. Position of this mosaic is indicated on Figure 4.6 as the dashed box. MOC narrow-angle images are M02/01989, M03/02048, M03/07394, M13/00247, M15/01482, E06/01790, and E12/01131.

ruled out but because these faults are not continued onto the neighboring bedrock. Thus I consider it unlikely that it is the bedrock that has faulted. In either case any flow processes operating were too slow to accommodate these stresses.

At the time these faults occurred, the ice sheet may have been much more extensive. Erosion via sublimation, wind, and mass wasting may have moved the bounding scarp back to a position where these faults are now exposed.

4.5 Conclusions and future direction

In many locations there are ice-rich mounds which seem to be in a state of sublimation-based retreat and yet display evidence of earlier flow. In other nearby areas there is ample evidence of brittle processes such as faulting and slope failure on different scales. These two disparate observations can be reconciled by postulating alternating episodes of glacial advance and sublimation-based retreat. Modeling of flow in the over many obliquty changes for the north polar cap (*Greve et al.*, 2003) indicates that we are currently in a 'slow' period for deformation by flow.

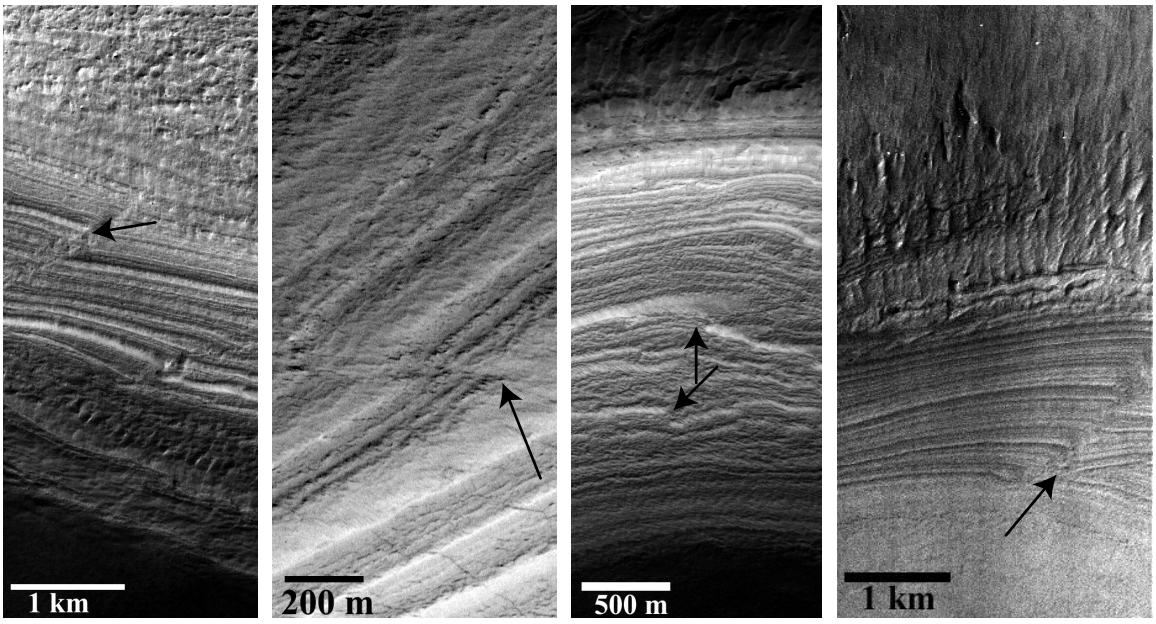

Figure 4.10: Examples of brittle processes on the bounding scarp of the south polar layered deposits. Arrows highlight offset layers indicating that faulting has taken place. Images are from left to right M04/02455 (73.4°S, 147°E, L_s 192°), M10/03514 (73.1°S, 135°E, L_s 273°), M15/02058 (73.4°S, 134°E, L_s 360°) and E09/01926 (73.9°S, 133°E, L_s 259°). Illumination is from the bottom right in each case and the downhill direction is from top to bottom (except in second from left).

The large quantities of water ice discovered within the mid-latitude regolith (*Boynton et al.*, 2002) and the snow layer proposed (*Christensen*, 2003) as an explanation for the gully phenomena in the middle latitudes could represent the present location of water ice which in glacial periods would be transported poleward by the atmosphere and accumulate again as fresh layered deposits. If the polar layered deposits were to wax and wane in thickness, then glacial activity at its margins would also respond to the increased pressure and driving force of the thicker ice sheet. Retreat via sublimation is likely operating to some extent at all times but may be periodically overtaken by this glacial activity.

The intention of this chapter is to outline evidence of episodes where flow was both possible and prohibited. The ability of ice to flow and the rate at which it does so is extremely sensitive to the temperature distribution within the ice sheet. The evidence supporting both flow and brittle processes indicates that the south polar layered deposits have alternated between these two regimes. Changes in polar climate due to obliquity variations is the most likely cause.

In the future, I will model the stress and temperature distribution within the ice sheet and investigate the range of flow rates over different obliquity conditions. I will also quantify the sublimation expected from the equatorward facing slopes during this same time period and use the separation between the current ice sheet and possible moraines to date the last episode of ice advance. The crater identification work carried out by *Koutnik et al.* (2002) on craters >1 km in size indicates the surface age of the central part of the southern layered deposits is 30-100 Myr. This is many obliquity cycles and also likely includes many chaotic changes in mean obliquity.

During that work we also found that crater shapes did not systematically deviate from the circular forms expected. A much younger surface age ($\approx 10^5$ years) was suggested by the small craters (<500m diameter) which is consistent with a resurfacing event $\approx 10^5$ years ago which was effective enough to remove all previous craters in the small size range but leave the larger craters (>1 km diameter) intact. However one would expect that movement of the ice would affect the larger craters more than the smaller ones. Flow may not be expected to alter the overall characteristics of the

polar layered deposits as a whole, however it is possibly very important to the history of its margins.

Chapter 5

Conclusions

5.1 Overview and accomplishments of this work

Scientific investigation can be divided into stages; gathering data, extracting useful knowledge from the data, and using this newfound knowledge to form hypotheses which can be tested with new data. In this way one gains a better understanding of that which is being investigating.

The MGS dataset is truly enormous, being already larger than all other planetary missions combined. Only its surface has been scratched in the last few years and it will be decades before its usefulness will be exhausted. In the meantime, however, there are more missions and instruments (most immediately Mars Odyssey) which will add to the (still expanding) MGS dataset. Thus, a major challenge is to be able to extract useful knowledge about the Martian polar regions from the overwhelming (and expanding) volume of information we now have. The geographic information system that I have developed during my studies here at Caltech serves that purpose. Undoubtedly, many important innovations in data visualization will occur in the coming years but the tools I have developed here should last for the foreseeable future and have already been widely employed by researchers here.

Useful knowledge about the Martian polar regions is increasing but so far there have been no new paradigms to explain layered deposit formation. Thus the original question about the polar layered deposits, i.e., what is the history that is recorded in the layering?, is still relevant. The original model envisioned thirty years ago

considered the layered deposits to be a mix of atmospherically deposited dust and ice with deposition switching from one hemisphere to another leading to correlated layering in the northern and southern deposits. While it is still expected that the layered deposits are dusty ice, we now know that the originally envisioned metronome type effect where deposition would switch periodically from hemisphere to hemisphere was overly simplistic. The MGS data have confirmed that the layered deposits in each hemisphere have had very different histories and have likely undergone differing processes at different stages. So we lack a 'big picture' explanation through which we can interpret the enormous amount of data now being returned. A long-term goal of Mars polar research is to create such an explanation and have it be consistent with all new data.

The work I have completed in graduate school has gone some way towards gaining an understanding of how these polar deposits have been shaped by different process over different timescales. In this thesis I have examined processes operating in the Martian polar regions on timescales ranging from $\approx 10^2$ to $\approx 10^7$ Martian years.

Chapter 2 dealt with the discovery of a distinct division within the stratigraphy of the north polar layered deposits. The nature of the lower unit was determined to be primarily sand based which differs radically from that of the overlying dust-ice mixture. If there was indeed a time in which the icy north polar cap was absent and a large Sahara-scale sand deposit existed, this leads to new insight into the variability of the polar environment. Obliquity variations have been expected to lead to the layering seen in the polar deposits. However even extreme obliquity excursions would seem incapable of totally removing the entire northern cap due to the formation of a protective sublimation lag (*Hofstadter and Murray*, 1990; *Mischna et al.*, 2003). Dating this unconformity is difficult because the time needed to form the 2.5 km of layered deposits which overlie this sand rich unit is uncertain. *Laskar et al.* (2002) have estimated a deposition rate of 0.05 cm yr^{-1}, which (assuming a constant deposition rate) would imply a time period of 5 Myr to deposit the section. However their analysis only applied to the upper 10% of the layered deposits. I consider a more likely hypothesis that the unconformity between these two units is

related to something more significant in Mars' history such as an extreme short-term environmental change brought on by the last major volcanic episode. It is also a possibility that the layered deposits are a recent phenomena and did not exist at all before a few million years ago although the derived 30-100 Myr surface age of the southern deposits (*Koutnik et al.*, 2002) argue against that.

Alternatively, it is possible (although very unlikely) that the north polar ice cap present before this one was composed of exceptionally clean water ice. Pure water ice would not acquire a protective lag deposit during sublimation and for extreme obliquities ($\geq 45^{\circ}$) the cap could be subliming at rates of $\approx$20 cm yr^{-1} (*Mischna et al.*, 2003). If so the cap would have a lifetime of only 12,500 yrs.

Whatever the mechanism by which any putative early north polar cap was removed, an important issue arises of where that water went during this time period. It is possible that the water was concentrated at lower latitudes filling craters and is responsible for the apparent sedimentary exposures reported by *Malin and Edgett* (2000). It is unlikely to have been transported to the south polar region as each pole receives roughly the same amount of insolation during a Martian year and volcanic activity as extreme as that proposed would probably have a global impact, effecting both poles equally.

Chapter 3 dealt with the modeling of a new and unexpected process, the erosion of the southern residual CO_2 cap by expanding flat floored pits. In this work we accomplished two major things. We placed an upper limit on the size of the solid CO_2 reservoir which rendered it insignificant even compared to the present atmosphere. We now know the atmosphere contains at least 20 times more CO_2 than the solid cap. This places an important constraint on the climactic history of the planet. The other accomplishment that came from modeling these flat floored pits is the recognition of a distinct population of these features which were all initiated close together in time. Some sort of environmental change, which we speculate may be related to changing surface albedo patterns, occurred on the order of Martian centuries ago to commence the growth of these features. Geomorphologic interpretations of a different class of these features possibly indicate that this environmental change has happened more

than once. This is the first recognition of environmental variability on Mars that is not related to either variation in orbital parameters or short-term (< 1 year) dust activity.

Chapter 4 explored the possibility of a changing polar environment which causes flow processes at the margin of the layered deposits to start and stop repeatedly. These changes are probably coupled to variations in orbital parameters. This work is still continuing. I intend to model the stress and temperature distribution within the ice sheet over different obliquity conditions to try and quantify the timescales involved.

5.2 Present shortcomings and future opportunities of Martian polar science

After more than three decades of observations it still is not clear what we can learn from the polar layered deposits. Every book, article, conference abstract or thesis (including this one) which deals with this subject starts with a statement that the layered deposits contain a record of the environmental history of Mars and that this record is proving *'difficult'* to understand. A detailed record of previous environments is there, that much is certain. Returning to the idea of the steps toward scientific progress (getting the data, extracting the useful knowledge, and forming and testing hypotheses), we have definitely passed the first step of amassing voluminous quantities of data. One can easily see how this will be turned into useful knowledge over the coming years and how people will form new conjectures from this knowledge. However, the step from there to understanding and retrieving the environmental history contained within the layered deposits seems elusive.

There is a limit as to how far remote sensing can enable one to make new discoveries, although that limit has not yet been tested (or even discovered). At some point however we will need *in situ* measurements on Mars to make any more progress. The failed Mars polar lander would have gone some way towards providing those data for

the south polar layered deposits, although only at the very surface. Using the layering present in the Greenland ice sheet as an analogy, there is little that Greenland ice can tell us about Earth's history without actually going there and retrieving an ice core for analysis. The same is ultimately true of the Martian ice sheets.

Having said that there are several major questions which are possibly answerable in the near-term using existing or soon to be acquired data.

- Rates of flow of the layered deposits, present and past.
- Structure of internal layering and basement topography.
- Possibility of basal melting, present and past.
- Are the polar deposits still accumulating today?
- How do changes in obliquity affect the the accumulation of layered deposits?

Progress on all of these issues can be expected in the next five years. The elusive holy grail which everybody continues to pursue, i.e., retrieving detailed history from the layered deposits, will likely have to wait considerably longer than that.

5.3 Application of future data to these issues

It would be useful (before drowning in a sea of bits) to outline in advance how these future instruments will contribute to the research topics discussed in this thesis. Several promising instruments are due to fly within the next few weeks (Mars Express) and more within a few years (Mars Reconnaissance Orbiter).

The High Resolution Stereo Camera (HRSC) will provide planet-wide stereo color coverage at 10-30 m/pixel. Combined with MOLA topography this will describe the shape of the layered deposits in an unprecedented level of detail. Stratigraphic studies will benefit greatly from a topography dataset that has a resolution similar to the images in which strata are being mapped.

The MARSIS instrument is a subsurface sounding radar and will provide the first active sounding of the Martian subsurface. This is especially important for the layered

deposits. Detection of the shape of internal layering will be an important diagnostic of whether flow processes are occurring. And the extraction of the subsurface topography of the ice caps will greatly help constrain models of the flow history.

Mars Express is due to launch on June 2, 2003. Mars Reconnaissance Orbiter will be launched in 2005 and, like Mars Express, will contain a stereo color camera (HiRISE) and a subsurface radar sounder (SHARAD). HiRISE will provide resolutions of 10's of centimeters for small areas and so is a good complement to the European HRSC. In addition a landed mission to the Martian polar regions is under consideration for the 2007 scout mission opportunity.

Of course the success of future missions is not assured (as evidenced by the consecutive failures in 1999 of Mars Climate Orbiter, Mars Polar Lander, and both Deep Space 2 microprobes). However, even if all these future missions blow up on the launch pad there are more than enough data to keep Mars polar scientists busy for a long time to come just pursuing the research issues outlined in the previous section.

Appendix A

Data processing

A.1 A Geographic Information System (GIS) for Mars

After a year of the Mars Global Surveyor mapping mission, data was being reported in three different datums (*Davies et al.*, 1992, 1996; *Seidelmann et al.*, 2002), in multiple projections and in almost every format imaginable. This made comparison between different instruments and even different missions very difficult. These problems were especially bad at the time of the landing site selection of the Mars Polar Lander. At that time I began work here at Caltech to translate all the polar data into a common coordinate system and projection and apply well-delevoped terrestrial GIS techniques. Similar efforts were underway for other regions of the planet at the USGS, Flagstaff.

I chose to use the ellipsoidal form of the polar stereographic projection (*Snyder*, 1987) with the IAU1994 datum (*Davies et al.*, 1996). This datum was the most recent at the time but has since been undated (*Seidelmann et al.*, 2002). As this will hopefully be the last update for some time, and I am in the process of converting all data to comply with this new system.

Once all data have been projected into this coordinate system all longitude and latitude information was forgotten. From that point onward all coordinates were in meters with the north/south pole at the origin. Polar stereographic is conformal and perspective but not equal-area or equidistant.

A.2 Interpolating gridded products

The MGS spacecraft has a polar orbit with all instruments being co-aligned and nadir viewing. This means that the data are taken in strips which are mostly north-south but which are east-west at the polar regions. The repeated coverage at the poles means that a high density of individual measurements are present in these areas some of which are somewhat redundant as they overlap. Often the most efficient way to look at large quantities of such data was to make gridded products. This has been done in many cases, most usually for MOLA elevations and TES albedos and temperatures. The procedure in each case is the same and follows the method of *Neumann et al.* (2001), who generated interpolated MOLA products. Longitudes and latitudes were converted to cartesian position within our projected coordinate system. The gridded product was constructed by fitting a continuous curvature surface with adjustable tension (usually set to 0.25) to all of the available points. Preprocessing of the data using a blockmedian filter helped reduce the volume of points to be fit and prevent short-scale aliasing problems. The generic mapping tools (*Wessel and Smith*, 1998) were used for the surface generation.

In the case of the MOLA DEM's some data was excluded based upon the large magnitude of the crossover correction applied (which indicates poor positioning). Data taken while the spacecraft was looking off nadir were also excluded (with the exception of data falling between latitudes of 87° and 90°) since this data is inherently less accurately positioned. After generating the surface some MOLA tracks that were poorly positioned showed up by either ploughing an obvious furrow through the surface or tearing up an equally obvious ridge. These tracks were manually identified and the surface regenerated without them.

Two things were considered when choosing a cell size for the final gridded product. At least 50% of the cells had to contain real data as opposed to having a value created by the interpolation scheme. In addition the cell size cannot be smaller than the resolution of the observation, e.g. the resolution of TES is ≈3 km so there is little point creating a surface where the cell size is 1 Km as it will not provide greater

accuracy.

A.3 Using MOLA to register MOC images

The latitude and longitude of each MOLA point have been adjusted based on a track crossover analysis (*Neumann et al.*, 2001). This process makes MOLA data the most accurately located data on the planet's surface. MOLA points acquired simultaneously with a MOC narrow angle image can also be located within the image using spacecraft time and information on the co-alignment of the narrow angle CCD and MOLA boresight. Using this information it is possible to adjust the reported positions of MOC narrow angle images so that MOLA points within the image coincide with their proper positions on the surface of the planet. The new coordinates of the MOC image are superior to those obtained from normal spacecraft orbital information since they also now include the MOLA crossover correction.

I project individual MOC narrow angle images using a first-order polynomial to match source and destination pixel locations. Since this warping is first order, it includes translation, an independent scaling in x and y, and a rotational term. There is also a nonlinear term which makes the transformation non-affine, but this term is usually insignificant compared to the others. One complication is that because all the MOLA points fall on the same column of the image there is no control on the sample resolution (although the line resolution is well determined). Sample resolution is calculated from range measurements combined with knowledge of the instantaneous field of view and summing mode of the camera. I wrote the software to perform the data correlation, coordinate conversions and geometric warping of the images in Interactive Data Language (IDL). The USGS software package (ISIS) was used to radiometrically calibrate the images.

In this way MOC images can be placed relative to each other and to their surroundings in an accurate self-consistent way. Where narrow-angle images overlap, the mutual offset is commonly observed to be a few tens of meters. In contrast, using spacecraft pointing to position images in the traditional way results in errors of order

a kilometer.

Although this technique represents a significant improvement, it cannot be applied successfully to all images. MOC images are heavily compressed before transmission to Earth. Although this compression is effective, it is sensitive to transmission errors. If a single pixel is incorrectly transmitted, it renders many 10's of image lines uncompressable. These uncompressed lines often show up as garbage, but also are often simply dropped from the image. This is unfortunate because the spacecraft time of each line is calculated by counting up the number of lines and combining it with the line exposure duration. If lines are entirely missing, then this method of calculating the time of each line will fail and it will not be possible to correlate the image with the MOLA dataset.

MOLA unfortunately failed in June of 2001 so that MOC images after the E05 mapping phase (see Appendix C) are positioned significantly less accurately than their earlier counterparts. For most areas on the planet this is not serious; image locations can be corrected by hand. However, in the polar regions the imaging density is much higher and it is not feasible to manually register thousands of MOC narrow angle images.

Appendix B

Swiss-cheese feature modeling description

B.1 Radiation balance inside a depression composed of annular rings

Swiss-cheese features in our model are represented by a series of concentric annular rings. Here we give formulas for computing the radiation budget of one of these annular rings. These rings maintain the same inner and outer radii but can independently change in height in response to sublimation or condensation of CO_2 ice. The height difference between the inner and outer radii of a ring governs what slope a surface element on the ring has. This model is cylindrically symmetric with the sun assumed to be circling at the same elevation throughout the day. This assumption is valid at the pole. The depression expands by incorporating more rings at its outer edge.

Since the shape of the depression evolves with time, the formulas must be valid for depressions of arbitrary cross section (profile of depth vs. radius). The formulas handle thermal emission, absorption, and scattering to all orders for both short wave and long wave radiation. We assume that every facet (we use the term facet to mean a small planar section of these annular rings) can receive radiation from every other facet, so the depression must be concave upward. This assumption was checked during the evolution of the depression shape and was found to be valid. The basic method for treating scattering by Lambert surfaces follows *Vasavada et al.* (1999), who used

techniques from thermal engineering and computer graphics (*Siegel and Howell*, 1981; *Goral et al.*, 1984).

B.1.1 Scattering of radiation from one facet to another

Consider two planar facets with arbitrary area, orientation and distance as shown on Figure B.1. The areas of facet 1 and 2 are denoted by A_1 and A_2, respectively.

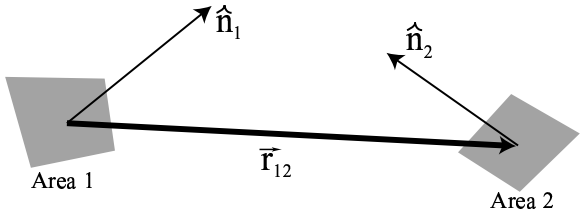

Figure B.1:

The solid angle of facet 1 as seen from facet 2 (see Figure B.1) is given by $\frac{A_1 \hat{n}_1 . \hat{r}_{12}}{|\vec{r}_{12}^2|}$

The collecting area of facet 2 is given by $-A_2 \hat{n}_2 . \hat{r}_{12}$

The flux leaving facet 1 is F_1, an intensity of F_1/π assuming a lambert surface.

The Flux on facet 2 from facet 1 is therefore:

$$\frac{A_1 A_2 F_1}{\pi |\vec{r}_{12}^2|} (\hat{n}_1 . \hat{r}_{12})(-\hat{n}_2 . \hat{r}_{12}) \tag{B.1}$$

or

$$\frac{A_1 A_2 F_1}{\pi (|\vec{r}_{12}^2|)^2} (\hat{n}_1 . \vec{r}_{12})(-\hat{n}_2 . \vec{r}_{12}) \tag{B.2}$$

B.1.2 Scattering of radiation from one annular ring to another

Consider first radiation scattered from one point to another (described in Figure B.2) using the relations derived in Section B.1.1.

$$\hat{n}_2 = \cos\theta_2 \hat{k} - \sin\theta_2 \hat{i} \tag{B.3}$$

$$\hat{n}_1 = \cos\theta_1 \hat{k} - \sin\theta_1 (cos\phi \hat{i} + sin\phi \hat{j}) \tag{B.4}$$

$$\vec{r}_{12} = -h\hat{k} - (r_1 \cos\phi - r_2)\hat{i} - r_1 \sin\phi \hat{j} \tag{B.5}$$

where θ_1 and θ_2 are the angles that the normal of facet 1 and 2 make to the vertical.

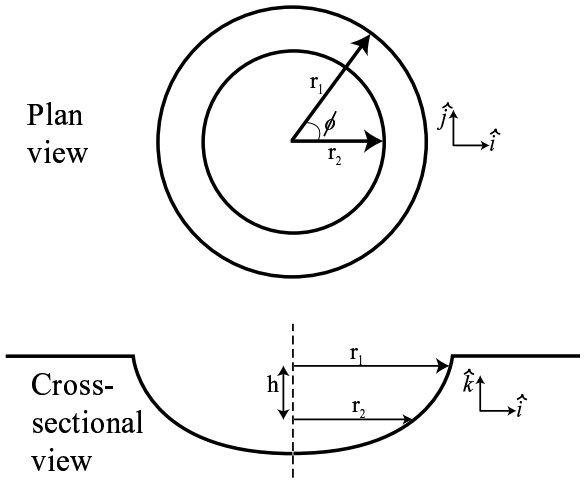

Figure B.2:

$$\hat{n}_1 . \vec{r}_{12} = -h\cos\theta_1 + r_1 \sin\theta_1 - r_2 \sin\theta_1 \cos\phi \tag{B.6}$$

$$-\hat{n}_2 . \vec{r}_{12} = h\cos\theta_2 + r_2 \sin\theta_2 - r_1 \sin\theta_2 \cos\phi \tag{B.7}$$

$$|\vec{r}_{12}|^2 = h^2 + r_1^2 + r_2^2 - 2r_1 r_2 \cos\phi \tag{B.8}$$

Now consider an annular ring of facets. Bearing in mind that $\delta A_1 = \delta l_1 r_1 \delta\phi$ where δl_1 is the width of ring 1, we integrate ϕ from $0 \rightarrow 2\pi$ to add up the contribution from each part of ring 1. The Flux from annular ring 1 onto an element of annular ring 2 is:

$$\mathcal{F} = \frac{F_1 A_2}{\pi} \int_0^{2\pi} \frac{(-h\cos\theta_1 + r_1 \sin\theta_1 - r_2 \sin\theta_1 \cos\phi)}{(h^2 + r_1^2 + r_2^2 - 2r_1 r_2 \cos\phi)^2} \times (h\cos\theta_2 + r_2 \sin\theta_2 - r_1 \sin\theta_2 \cos\phi)\delta l_1 r_1 \delta\phi \tag{B.9}$$

We can make some convienent substitutions:

$$a = -h\cos\theta_1 + r_1 \sin\theta_1$$
$$b = \tfrac{1}{2} r_2 \sin\theta_1$$
$$c = h\cos\theta_2 + r_2 \sin\theta_2$$
$$d = \tfrac{1}{2} r_1 \sin\theta_2$$
$$f = h^2 + r_1^2 + r_2^2$$
$$g = r_1 r_2$$
$$k = \sqrt{f^2 - 4g^2}$$

So $\mathcal{F}$ becomes

$$\mathcal{F} = \frac{F_1 A_2 \delta l_1 r_1}{\pi} \int_0^{2\pi} \frac{(a - 2b\sin\phi)(c - 2d\cos\phi)}{(f - 2g\cos\phi)^2} \delta\phi \tag{B.10}$$

or

$$\mathcal{F} = \frac{F_1 A_2 A_1}{\pi} \frac{1}{2\pi} \int_0^{2\pi} \frac{(a - 2b\sin\phi)(c - 2d\cos\phi)}{(f - 2g\cos\phi)^2} \delta\phi \tag{B.11}$$

The above integral can be solved using the residue theorm; first we make the substitution:

$$z = \exp i\phi$$
$$\cos\phi = \tfrac{1}{2}(z + \tfrac{1}{z})$$
$$\delta\phi = \tfrac{\delta z}{iz}$$

The limits of the original integral are $0 \rightarrow 2\pi$ so this integral in now a closed unit circle in the complex plane.

$$\mathcal{F} = \frac{F_1 A_2 A_1}{\pi} \frac{1}{2\pi i} \oint \frac{(a - b(z + \frac{1}{z}))(c - d(z + \frac{1}{z}))}{(f - g(z + \frac{1}{z}))^2} \frac{\delta z}{z} \tag{B.12}$$

Rearranging this equation we see that

$$\mathcal{F} = \frac{F_1 A_2 A_1}{\pi} \frac{1}{2\pi i} \oint \frac{(a - b(z + \frac{1}{z}))(c - d(z + \frac{1}{z}))}{\left(z - \frac{f}{2g} - \sqrt{\frac{f^2}{4g^2} - 1}\right)^2 \left(z - \frac{f}{2g} + \sqrt{\frac{f^2}{4g^2} - 1}\right)^2} \frac{z \delta z}{g^2} \tag{B.13}$$

OR

$$\mathcal{F} = \frac{F_1 A_2 A_1}{\pi} \frac{1}{2\pi i} \oint \frac{(az - b(z^2 + 1))(cz - d(z^2 + 1))(fz - g(z^2 + 1))^{-2}}{z} \delta z \tag{B.14}$$

It can be seen from these two froms that there are three poles:

$$z_0 = 0 \tag{B.15}$$

$$z_+ = \frac{f}{2g} + \sqrt{\frac{f^2}{4g^2} - 1} \tag{B.16}$$

$$z_- = \frac{f}{2g} - \sqrt{\frac{f^2}{4g^2} - 1} \tag{B.17}$$

Since f and g are real positive numbers we can see that $|z_+| \geq 1$ and conversely $|z_-| \leq 1$ so z_+ is outside the unit circle and we do not include it in the residue theorm solution of the above integral. The solution to the integral is $2\pi i(R_0 + R_-)$

$$\mathcal{F} = \frac{F_1}{\pi} A_2 A_1 (R_0 + R_-) \tag{B.18}$$

To calculate R_0 we evaluate z times the integrand in Equation B.14 and set $z = 0$:

$$R_0 = (-b)(-d)(-g)^{-2} = \frac{bd}{g^2} \tag{B.19}$$

Calculating R_- is more complicated because the pole appears in squared form in the denominator. To calculate R_- we do the following. First we rewrite Equation B.13 as:

$$\mathcal{F} = \frac{F_1 A_2 A_1}{\pi} \frac{1}{2\pi i} \oint \frac{q(z)}{(z - z_-)^2} \delta z \tag{B.20}$$

where

$$q(z) = \frac{(a - b(z + \frac{1}{z}))(c - d(z + \frac{1}{z}))}{(z - z_+)^2} \frac{z}{g^2} \tag{B.21}$$

The residue can be seen to be $R_- = \frac{\delta q}{\delta z}|_{z_-}$

$$R_- = \frac{-b(1 - \frac{1}{z_-^2})(c - \frac{df}{g})z_- - b(1 - \frac{1}{z_-^2})(a - \frac{bf}{g})z_- + (a - \frac{bf}{g})(c - \frac{df}{g})(1 - \frac{2z_-}{z_- - z_+})}{g^2 \frac{k^2}{g^2}} \tag{B.22}$$

$$R_- = \frac{(z_- + \frac{1}{z_-})(bc + ad - \frac{2bdf}{g}) + (a - \frac{bf}{g})(c - \frac{df}{g})(1 + \frac{2gz_-}{k})}{k^2} \tag{B.23}$$

$$R_- = \frac{\frac{f}{g}(bc + ad - \frac{2bdf}{g}) + (a - \frac{bf}{g})(c - \frac{df}{g})(\frac{f}{k})}{k^2} \tag{B.24}$$

So the final answer is

$$\mathcal{F} = \frac{F_1}{\pi} A_2 A_1 \left(\frac{bd}{g^2} + \frac{\frac{f}{g}(bc + ad - \frac{2bdf}{g}) + (a - \frac{bf}{g})(c - \frac{df}{g})(\frac{f}{k})}{k^2} \right) \tag{B.25}$$

We can write $\mathcal{R}$ for each pair of annular rings in a matrix $\mathcal{R}_{ij}$ where $\mathcal{R}_{ij} = \mathcal{R}_{ji}$.

$$\mathcal{F} = \frac{F_1}{\pi} A_i A_j \mathcal{R}_{ij} \tag{B.26}$$

If we know the flux leaving all the annular bands we can use this matrix to calculate how much of that energy lands on our facet of interest. The practicalities of this procedure are discussed in the next subsection.

B.1.3 Calculating the energy balance of an annular band

For thermal radiation the flux (F_i) leaving each square meter of the ith band can be calculated by combining its thermal emmission and reflected thermal radiation which was incident from the other bands.

$$F_i = \varepsilon\sigma T_i^4 + (1-\varepsilon_i)\sum_{j=1}^{n}\frac{F_j}{\pi}A_j\mathcal{R}_{ij} \tag{B.27}$$

$$-\varepsilon\sigma T_i^4 = \sum_{j=1}^{n}\left(\frac{(1-\varepsilon_i)A_j\mathcal{R}_{ij}}{\pi} - \delta_{ij}\right)F_j \tag{B.28}$$

This creates a set of linear simultaneous equations which can be written in matrix form. Given a list of temperatures $T_{1\ldots n}$, we can invert this n×n matrix (where n is the number of facets) to solve for flux (F_j) leaving each annular band.

The energy balance of the visible radiation works in an analogous way. Let S_i be the power per unit area incident on the ith band. Let D_i be the direct sunlight incident on the band, averaged over a day. This depends on the solar zenith angle and the geometry of the depression, in particular the height and radius of the ith band relative to the height and radius of the depression rim. There are three possibilities: a facet on the band is in sunlight throughout the day; it is in shadow throughout the day; or it alternates between sunlight and shadow during the day. For the latter case we compute the daily average insolation. The equation for S_i is then

$$S_i = D_i + \sum_{j=1}^{n}\frac{S_j}{\pi}\mathcal{W}_j A_j\mathcal{R}_{ij} \tag{B.29}$$

$$-D_i = \sum_{j=1}^{n}\left(\frac{\mathcal{W}_j A_j\mathcal{R}_{ij}}{\pi} - \delta_{ij}\right)S_j \tag{B.30}$$

where $\mathcal{W}_j$ is the albedo of the jth band. Again this constitutes a set of simultaneous equations for S_j, which can be written in matrix form. We can combine these two formulae to find the radiative heating of one square meter on the ith band.

$$H_i = (1-\mathcal{W}_i)S_i - \varepsilon\sigma T_i^4 + \varepsilon_i\sum_{j=1}^{n}\frac{F_j}{\pi}A_j\mathcal{R}_{ij} \tag{B.31}$$

B.2 Response to energy balance: Conduction and sublimation

Given the radiative heating (H_i) on an annular band, we can march the system forward by one time step. If the band is bare water ice, we solve the one-dimensional diffusion equation for the new temperature distribution within the ice, given the old temperature distribution and the heat flux at the surface (H_i). Lateral heat diffusion within exposed water ice is neglected. The new value of the surface temperature goes into the radiative calculation at the next time step.

If the band has CO_2 frost on top of water ice, we solve for the change in mass of the CO_2 frost, given the latent heat of CO_2, the radiative heat flux at the top, and the conductive heat flux coming up from the water ice underneath. At the same time we solve the one-dimensional diffusion equation for the new temperature distribution within the water ice, given the old temperature distribution and the prescribed temperature at the upper boundary, which in this case is the CO_2 frost temperature. With the new temperature distribution within the water ice, we can compute the new heat flux conducted into the CO_2 above, and we are ready for the next time step.

It can happen that the mass of CO_2 drops below zero or the temperature at the surface of the water ice drops below the CO_2 frost point. In the former, case we set the CO_2 mass to zero and treat the band as an uncovered water ice band on the next time step. In the latter case, we set the temperature at the top of the water ice to the CO_2 frost temperature. Then we add up the deficit of temperature (below the frost point) in the upper layers of the water ice, convert it to a heat content (energy per unit area), and add the equivalent amount of CO_2 frost based on the latent heat of vaporization. On the next time step we treat the band as a layer of CO_2 on top of water ice. If the water ice has never been bare, its temperature will be equal to that of the CO_2 on top. If the water ice has been bare, we follow its temperature evolution under the influence of the varying conditions at its upper boundary.

B.3 Following depression geometry

Since the depression is represented by finite elements which have a fixed width, it can only expand or contract by changing the number of elements in its interior. Here we describe how the model handles the geometry where the depression surface intersects the surrounding flat upper surface and the interior flat water ice layer.

The level of the surrounding upper surface (which is always CO_2) is tracked by a simple radiative model. There is no conduction to keep track of here. The amplitude of the annual surface level changes were ≈ 1.4m. The albedo and emissivity were set so that this flat surface returned to the same elevation at the same time each year.

B.3.1 The outer edge

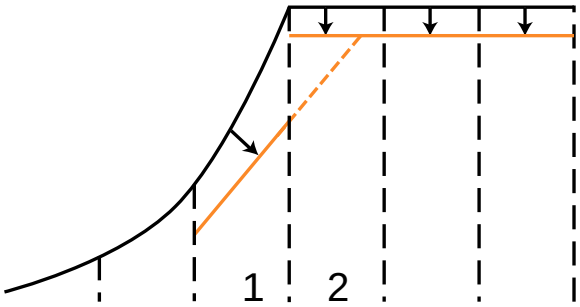

Figure B.3:

The position of the intersection of the depression rim with the flat surface was calculated by extrapolating the outermost facet (see Figure B.3). Here the facet labeled 1 is the outermost facet within the depression, and the facet labeled 2 is controlled by the behavior of the flat surface. Sublimation inside the depression is exceeding sublimation from the flat surface so facet 1 drops below facet 2. The dashed line shows the extrapolated new position of the depression rim. More than 50% of facet 2 is now within the depression so we absorb this facet into the depression on the next timestep.

B.3.2 The inner edge

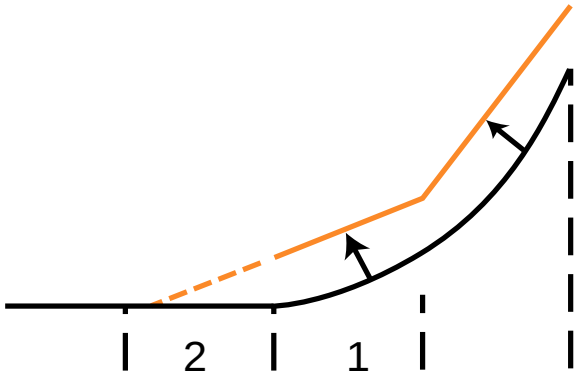

Figure B.4:

The situation with the inner edge is analogous to the outer edge. In Figure B.4 we see frost accumulating on the CO_2 walls (facet 1) but not on the water-ice floor (facet 2). The new inner edge of the wall is computed by extrapolation (dashed line). Each facet must be entirely frost covered or frost free for the purposes of this model. If the new edge incorporates more that 50% of a previously frost free facet then that facet is considered to be fully frosted and the new inner edge has moved by one integer facet.

Appendix C

Data timeline

After the Viking and Mariner missions of the 1970's, there was a long hiatus of about two decades before another spacecraft successfully entered orbit around Mars. Mars Global surveyor entered orbit on September 12, 1997, and started the process of areobraking to circularize its orbit. Problems with a weakened solar panel were encountered, which slowed the aerobraking process. During the areobraking period some data was acquired (marked as Aerobraking I on figure C.1), aerobraking was paused on two occasions to collect scientific data (marked as SPO I and SPO II on figure C.1). The orbit was circularized and the spacecraft entered the mapping phases of its mission in March 1999. The final mapping orbit was a 400 km altitude near polar (93° inclination) circular orbit. After a complete Martian year of mapping the spacecraft had completed its primary mission. On January 31, 2001, Mars global surveyor entered its extended mission and has just completed a second Martian year of observations. During the mission the MOC and TES continued working, the MOLA instrument failed in June 2001.

Mars Odyssey entered Mars orbit on October 24, 2001. In this case aerobraking went smoothly and the spacecraft entered its mapping orbit (which is basically the same as that of Mars Global Surveyor) in February 2002. All instruments with the exception of the MARIE radiation experiment are operational and the spacecraft is returning data continuously.

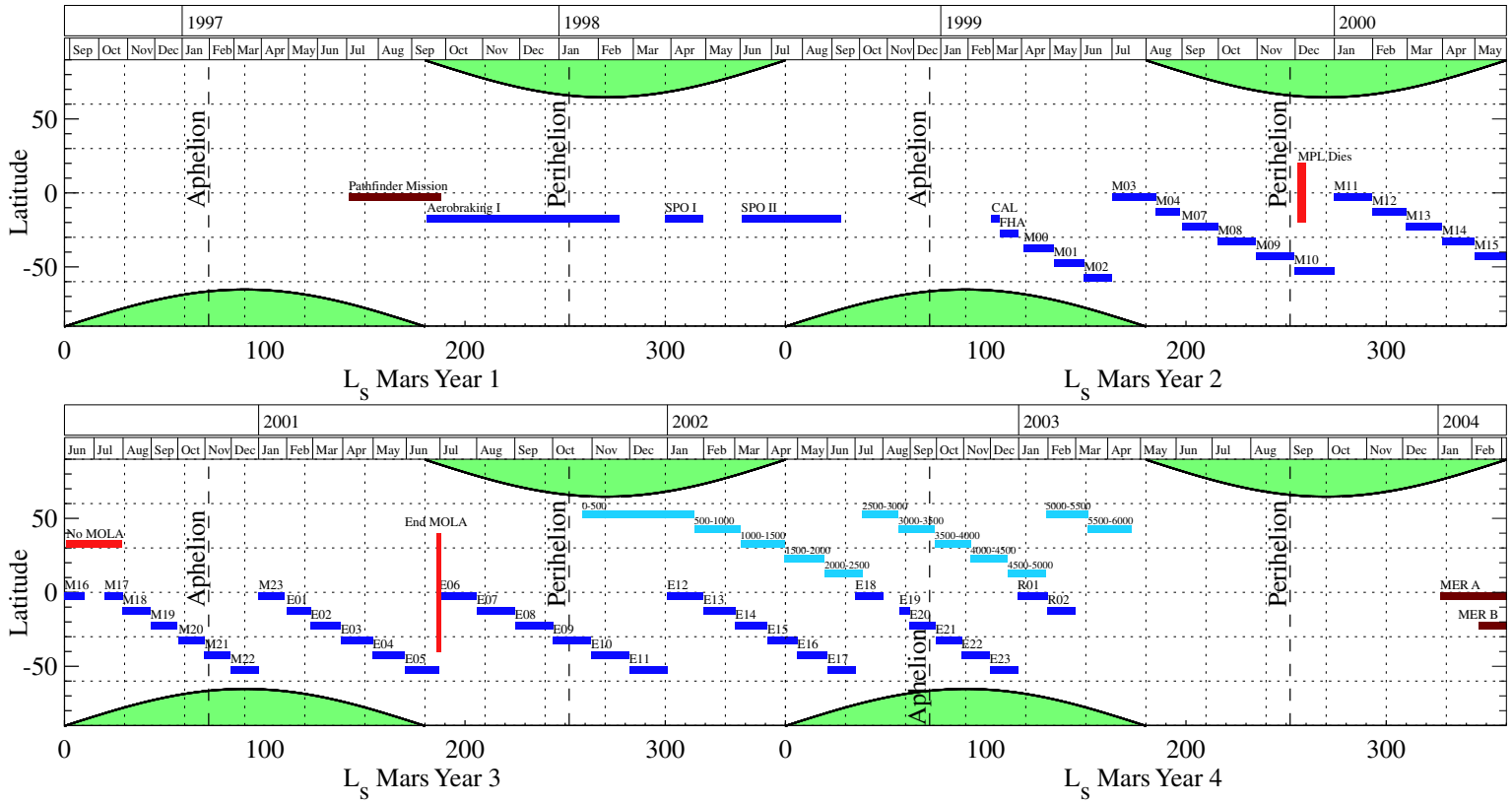

Figure C.1: Conversion chart from Earth date to Martian season (L_s) for four Mars years. Martian season is linear on this plot. Due to the eccentricity of the Martian orbit time is not linear and passes 'quicker' at Mars aphelion than perihelion. The green areas indicate areas of permanent darkness. Light and dark blue rectangles show data acquisition periods for different missions. Significant events are also indicated on the plot.

Bibliography

Aharonson, O., M. T. Zuber, and D. H. Rothman, Statistics of Mars' topography from the Mars Orbiter Laser Altimeter: Slopes, correlations, and physical models, *Journal of Geophysical Research*, *106*, 23,723–23,736, 2001.

Albee, A. L., F. D. Palluconi, and R. E. Arvidson, Mars Global Surveyor Mission: Overview and status, *Science*, *279*, 1671–1672, 1998.

Albee, A. L., R. E. Arvidson, F. Palluconi, and T. Thorpe, Overview of the Mars Global Surveyor mission, *Journal of Geophysical Research*, *106*, 23,291–23,316, 2001.

Baker, V. R., and D. J. Milton, Erosion by catastrophic floods on Mars and Earth, *Icarus*, *23*, 27–41, 1974.

Barker, E. S., R. A. Schorn, A. Woszczyk, R. G. Tull, and S. J. Little, Mars: Detection of atmospheric water vapor during the southern hemisphere spring and summer season, *Science*, *170*, 1308–1310, 1970.

Benito, G., F. Mediavilla, M. Fernandez, A. Marquez, J. Martinez, and F. Anguita, Chasma Boreale, Mars: A sapping and outflow channel with a tectono-thermal origin, *Icarus*, *129*, 528–538, 1997.

Blasius, K. R., J. A. Cutts, and A. D. Howard, Topography and stratigraphy of Martian polar layered deposits, *Icarus*, *50*, 140–160, 1982.

Boynton, W. V., et al., Distribution of hydrogen in the near surface of Mars: Evidence for subsurface ice deposits, *Science*, *297*, 81–85, 2002.

Breed, C. S., M. J. Grolier, and J. F. McCauley, Morphology and distribution of common 'sand' dunes on Mars - Comparison with the earth, *Journal of Geophysical Research*, *84*, 8183–8204, 1979.

Budd, W. F., D. Jenssen, J. H. I. Leach, I. N. Smith, and U. Radok, The north polar cap of Mars as a steady-state system, *Polarforschung*, *56*, 43–63, 1986.

Byrne, S., and B. C. Murray, North polar stratigraphy and the paleo-erg of Mars, in *Journal of Geophysical Research (Planets), Volume 107, Issue E6, pp. 11-1, CiteID 5044, DOI 10.1029/2001JE001615*, pp. 11–1, 2002.

Christensen, P. R., Formation of recent martian gullies through melting of extensive water-rich snow deposits, *Nature*, *422*, 45–48, 2003.

Christensen, P. R., et al., Thermal Emission Spectrometer experiment - Mars Observer mission, *Journal of Geophysical Research*, *97*, 7719–7734, 1992.

Christensen, P. R., et al., Mars Global Surveyor Thermal Emission Spectrometer experiment: Investigation description and surface science results, *Journal of Geophysical Research*, *106*, 23,823–23,872, 2001.

Christensen, P. R., et al., The Thermal Emission Imaging System (THEMIS) for the Mars 2001 Odyssey Mission, *Space Science Reviews*, 2003, *Submitted*.

Clifford, S., Chasma boreale (85°N, 0°W): Remnant of a martian jökulhlaup?, *Bull. Am. Astron. Soc.*, *12*, 678, 1980.

Clifford, S. M., Polar basal melting on Mars, *Journal of Geophysical Research*, *92*, 9135–9152, 1987.

Clifford, S. M., et al., The state and future of Mars polar science and exploration, *Icarus*, *144*, 210–242, 2000.

Cutts, J., Wind erosion in martian polar regions, *Journal of Geophysical Research*, *78*, 4211–4221, 1973a.

Cutts, J., Nature and origin of layered deposits of martian polar regions, *Journal of Geophysical Research*, *78*, 4231–4249, 1973b.

Cutts, J. A., and B. H. Lewis, Models of climate cycles recorded in Martian polar layered deposits, *Icarus*, *50*, 216–244, 1982.

Cutts, J. A., K. R. Blasius, G. A. Briggs, M. H. Carr, H. Masursky, and R. Greeley, North polar region of Mars - Imaging results from Viking 2, *Science*, *194*, 1329–1337, 1976.

Cutts, J. A., K. R. Blasius, and W. J. Roberts, Evolution of Martian polar landscapes - Interplay of long-term variations in perennial ice cover and dust storm intensity, *Journal of Geophysical Research*, *84*, 2975–2994, 1979.

Davies, M. E., V. K. Abalakin, A. Brahic, M. Bursa, B. H. Chovitz, J. H. Lieske, P. K. Seidelmann, A. T. Sinclair, and I. S. Tiuflin, Report of the IAU/IAG/COSPAR Working Group on Cartographic Coordinates and Rotational Elements of the Planets and Satellites - 1991, *Celestial Mechanics and Dynamical Astronomy*, *53*, 377–397, 1992.

Davies, M. E., et al., Report of the IAU/IAG/COSPAR Working Group on Cartographic Coordinates and Rotational Elements of the Planets and Satellites: 1994, *Celestial Mechanics and Dynamical Astronomy*, *63*, 127–148, 1996.

Dial, A. L. J., Geologic Map of the Mare Boreum area of Mars, 1984, U.S. Geol. Surv. Misc. Invest. Ser., Map I-1640.

Durham, W. B., S. H. Kirby, and L. A. Stern, Steady-state flow of solid CO_2: Preliminary results, *Geophysical Research Letters*, *26*, 3493–3496, 1999.

Edgett, K. S., and M. C. Malin, The Martian North Polar Cap: Sedimentary Aspects, in *Second International Conference on Mars Polar Science and Exploration*, pp. 32–33, 2000.

Fanale, F. P., and J. R. Salvail, Quasi-periodic atmosphere-regolith-cap CO_2 redistribution in the martian past, *Icarus*, *111*, 305–316, 1994.

Fenton, L. K., and K. E. Herkenhoff, Topography and stratigraphy of the northern Martian polar layered deposits using photoclinometry, stereogrammetry, and MOLA altimetry, *Icarus*, *147*, 433–443, 2000.

Fishbaugh, K. E., and J. W. Head, North polar region of Mars: Topography of circumpolar deposits from Mars Orbiter Laser Altimeter (MOLA) data and evidence for asymmetric retreat of the polar cap, *Journal of Geophysical Research*, *105*, 22,455–22,486, 2000.

Fisher, D. A., If Martian ice caps flow — Ablation mechanisms and appearance, *Icarus*, *105*, 501–511, 1993.

Fisher, D. A., Internal Layers in an "Accublation" Ice Cap: A Test for Flow, *Icarus*, *144*, 289–294, 2000.

Fisher, D. A., D. P. Winebrenner, and H. Stern, Lineations on the "white" accumulation areas of the residual northern ice cap of Mars: Their relation to the "accublation" and ice flow hypothesis, *Icarus*, *159*, 39–52, 2002.

Goral, C. M., K. E. Torrance, D. P. Greenberg, and B. B., Modeling the interaction of light between diffuse surfaces, *Computer Graphics*, *18*, 213–222, 1984.

Greeley, R., Silt-clay aggregates on Mars, *Journal of Geophysical Research*, *84*, 6248–6254, 1979.

Greeley, R., N. Lancaster, S. Lee, and P. C. Thomas, Martian aeolian processes, sediments, and features, in *Mars*, edited by H. H. Kieffer, B. M. Jakosky, C. W. Snyder, and M. S. Matthews, pp. 730–766, Univ. of Arizona Press, 1992.

Greve, R., Waxing and waning of the perennial north polar H_2O ice cap of Mars over obliquity cycles, *Icarus*, *144*, 419–431, 2000.

Greve, R., V. Klemann, and D. Wolf, Ice flow and isostasy of the north polar cap of Mars, *Planetary and Space Science*, *51*, 193–204, 2003.

Head, J. W., Mars: Evidence for geologically recent advance of the south polar cap, *Journal of Geophysical Research*, *106*, 10,075–10,087, 2001.

Head, J. W., and S. Pratt, Extensive Hesperian-aged south polar ice sheet on Mars: Evidence for massive melting and retreat, and lateral flow and ponding of meltwater, *Journal of Geophysical Research*, *106*, 12,275–12,300, 2001.

Herkenhoff, K. E., Geology, Composition, Age and Stratigraphy of the Polar Layered Deposits on Mars, in *First International Conference on Mars Polar Science and Exploration*, pp. 18–+, 1998.

Herkenhoff, K. E., and R. L. Kirk, Topography and Stratigraphy of the Polar Layered Deposits on Mars, in *Second International Conference on Mars Polar Science and Exploration*, pp. 74–75, 2000.

Herkenhoff, K. E., and B. C. Murray, Color and albedo of the south polar layered deposits on Mars, *Journal of Geophysical Research*, *95*, 1343–1358, 1990a.

Herkenhoff, K. E., and B. C. Murray, High-resolution topography and albedo of the South Polar layered deposits on Mars, *Journal of Geophysical Research*, *95*, 14,511–14,529, 1990b.

Herkenhoff, K. E., and J. J. Plaut, Surface Ages and Resurfacing Rates of the Polar Layered Deposits on Mars, *Icarus*, *144*, 243–253, 2000.

Herkenhoff, K. E., and A. R. Vasavada, Dark material in the polar layered deposits and dunes on Mars, *Journal of Geophysical Research*, *104*, 16,487–16,500, 1999.

Hofstadter, M. D., and B. C. Murray, Ice sublimation and rheology — Implications for the Martian polar layered deposits, *Icarus*, *84*, 352–361, 1990.

Howard, A. D., The role of eolian processes in forming surface features of the Martian polar layered deposits, *Icarus*, *144*, 267–288, 2000.

Howard, A. D., J. A. Cutts, and K. R. Blasius, Stratigraphic relationships within Martian polar CAP deposits, *Icarus*, *50*, 161–215, 1982.

Ingersoll, A. P., The case against permanent CO_2 frost caps, *Journal of Geophysical Research*, *79*, 3403–3410, 1974.

Ingersoll, A. P., T. Svitek, and B. C. Murray, Stability of polar frosts in spherical bowl-shaped craters on the moon, Mercury, and Mars, *Icarus*, *100*, 40–47, 1992.

Ivanov, A. B., and D. O. Muhleman, The role of sublimation for the formation of the northern ice cap: Results from the Mars Orbiter Laser Altimeter, *Icarus*, *144*, 436–448, 2000.

Jakosky, B. M., and R. M. Haberle, Year-to-year instability of the Mars south polar cap, *Journal of Geophysical Research*, *95*, 1359–1365, 1990.

James, P. B., H. H. Kieffer, and D. A. Paige, The seasonal cycle of carbon dioxide on Mars, in *Mars*, edited by H. H. Kieffer, B. M. Jakosky, C. W. Snyder, and M. S. Matthews, pp. 934–968, Univ. of Arizona Press, 1992.

Johnson, C. L., S. C. Solomon, J. W. Head, R. J. Phillips, D. E. Smith, and M. T. Zuber, Lithospheric loading by the northern polar cap on Mars, *Icarus*, *144*, 313–328, 2000.

Kieffer, H. H., Mars south polar spring and summer temperatures — A residual CO2 frost, *Journal of Geophysical Research*, *84*, 8263–8288, 1979.

Kieffer, H. H., T. Z. Martin, S. C. Chase, E. D. Miner, and F. D. Palluconi, Martian north pole summer temperatures — Dirty water ice, *Science*, *194*, 1341–1344, 1976.

Kieffer, H. H., T. N. Titus, K. F. Mullins, and P. R. Christensen, Mars south polar spring and summer behavior observed by TES: Seasonal cap evolution controlled by frost grain size, *Journal of Geophysical Research*, *105*, 9653–9700, 2000.

Kolb, E. J., and K. L. Tanaka, Geologic history of the polar regions of Mars based on Mars Global Surveyor data. II. Amazonian period, *Icarus*, *154*, 22–39, 2001.

Kolb, E. J., K. L. Tanaka, and J. A. Skinner, A New Mapping Approach for Highland Materials in the South Polar Region of Mars, in *Lunar and Planetary Institute Conference Abstracts*, pp. 2105–+, 2003.

Koutnik, M., S. Byrne, and B. Murray, South Polar Layered Deposits of Mars: The cratering record, in *Journal of Geophysical Research (Planets), Volume 107, Issue E11, pp. 10-1, CiteID 5100, DOI 10.1029/2001JE001805*, pp. 10–1, 2002.

Lancaster, N., and R. Greeley, Sediment volume in the north polar sand seas of Mars, *Journal of Geophysical Research*, *95*, 10,921–10,927, 1990.

Laskar, J., B. Levrard, and J. F. Mustard, Orbital forcing of the martian polar layered deposits, *Nature*, *419*, 375–377, 2002.

Leighton, R. R., and B. C. Murray, Behavior of carbon dioxide and other volatiles on Mars, *Science*, *153*, 136–144, 1966.

Lemoine, F. G., D. E. Smith, D. D. Rowlands, M. T. Zuber, G. A. Neumann, D. S. Chinn, and D. E. Pavlis, An improved solution of the gravity field of Mars (GMM-2B) from Mars Global Surveyor, *Journal of Geophysical Research*, *106*, 23,359–23,376, 2001.

Liu, J., M. I. Richardson, and R. J. Wilson, An assessment of the global, seasonal, and interannual spacecraft record of Martian climate in the thermal infrared, *Journal of Geophysical Research*, 2003, *In press.*

Malin, M. C., and K. S. Edgett, Sedimentary rocks of early Mars, *Science*, *290*, 1927–1937, 2000.

Malin, M. C., and K. S. Edgett, Mars Global Surveyor Mars Orbiter Camera: Interplanetary cruise through primary mission, *Journal of Geophysical Research*, *106*, 23,429–23,570, 2001.

Malin, M. C., G. E. Danielson, A. P. Ingersoll, H. Masursky, J. Veverka, M. A. Ravine,

and T. A. Soulanille, Mars Observer Camera, *Journal of Geophysical Research*, *97*, 7699–7718, 1992.

Malin, M. C., M. A. Caplinger, and S. D. Davis, Observational evidence for an active surface reservoir of solid carbon dioxide on Mars, *Science*, *294*, 2146–2148, 2001.

Mischna, M. C., M. I. Richardson, R. J. Wilson, and D. J. McCleese, orbital forcing of martian water and CO2 cycles: A general circulation model study with simplified volatile schemes, *Journal of Geophysical Research*, 2003, *In press.*

Murray, B., M. Koutnik, S. Byrne, L. Soderblom, K. Herkenhoff, and K. L. Tanaka, Preliminary geological assessment of the northern edge of Ultimi Lobe, Mars south polar layered deposits, *Icarus*, *154*, 80–97, 2001.

Murray, B. C., and M. C. Malin, Polar volatiles on Mars — Theory verus observation, *Science*, *182*, 437–443, 1973.

Murray, B. C., L. A. Soderblom, J. A. Cutts, R. P. Sharp, D. J. Milton, and R. B. Leighton, Geological framework of the south polar region of Mars, *Icarus*, *17*, 328–345, 1972.

Neumann, G. A., D. D. Rowlands, F. G. Lemoine, D. E. Smith, and M. T. Zuber, Crossover analysis of Mars Orbiter Laser Altimeter data, *Journal of Geophysical Research*, *106*, 23,753–23,768, 2001.

Nye, J., A flow model for the polar caps of mars, *J. Glaciology*, *46*, 438–444, 2000.

Nye, J. F., W. B. Durham, P. M. Schenk, and J. M. Moore, The instability of a south polar cap on Mars composed of carbon dioxide, *Icarus*, *144*, 449–455, 2000.

Paige, D. A., The annual heat balance of the Martian polar caps from Viking observations, Ph.D. thesis, California Institute of Technology, 1985.

Paige, D. A., and K. D. Keegan, Thermal and albedo mapping of the polar regions of Mars using Viking thermal mapper observations: 2. South polar region, *Journal of Geophysical Research*, *99*, 25,993–26,013, 1994.

Paige, D. A., J. E. Bachman, and K. D. Keegan, Thermal and albedo mapping of the polar regions of Mars using Viking thermal mapper observations: 1. North polar region, *Journal of Geophysical Research*, *99*, 25,959–25,991, 1994.

Pathare, A. V., D. A. Paige, and E. P. Turtle, Viscous relaxation of craters within the Martian polar layered deposits, *Icarus*, 2003, *Submitted*.

Piqueux, S., S. Byrne, and M. I. Richardson, The sublimation of Mars southern CO_2 ice cap and the formation of 'spiders', *Journal of Geophysical Research*, 2003, *In press*.

Plaut, J. J., R. Kahn, E. A. Guinness, and R. E. Arvidson, Accumulation of sedimentary debris in the south polar region of Mars and implications for climate history, *Icarus*, *76*, 357–377, 1988.

Saunders, R. S., and D. T. Blewett, Dunes in the north polar region of Mars - Their possible formation from low-density sedimentary aggregates, *Astronomicheskii Vestnik*, *21*, 181–188, 1987.

Saunders, R. S., T. J. Parker, J. B. Stephens, E. G. Laue, and F. P. Fanale, Transformation of polar ice sublimate residue into Martian circumpolar sand, in *Planetary Geology and Geophysics Program Report*, pp. 300–302, 1985.

Saunders, R. S., F. P. Fanale, T. J. Parker, J. B. Stephens, and S. Sutton, Properties of filamentary sublimation residues from dispersions of clay in ice, *Icarus*, *66*, 94–104, 1986.

Seidelmann, P. K., et al., Report of the IAU/IAG Working Group on Cartographic Coordinates and Rotational Elements of the Planets and Satellites: 2000, *Celestial Mechanics and Dynamical Astronomy*, *82*, 83–111, 2002.

Sharp, R. P., B. C. Murray, R. B. Leighton, L. A. Soderblom, and J. A. Cutts, The surface of Mars 4: South polar cap, *Journal of Geophysical Research*, *76*, 357, 1972.

Siegel, R., and J. R. Howell, *Thermal radiation heat transfer*, Series in Thermal and Fluids Engineering, New York: McGraw-Hill, 1981, 2nd ed., 1981.

Smith, D. E., M. T. Zuber, and G. A. Neumann, Seasonal variations of snow depth on Mars, *Science*, *294*, 2141–2146, 2001a.

Smith, D. E., et al., Topography of the northern hemisphere of Mars from the Mars Orbiter Laser Altimeter, *Science*, *279*, 1686–1692, 1998.

Smith, D. E., et al., The global topography of Mars and implications for surface evolution, *Science*, *284*, 1495–1503, 1999.

Smith, D. E., et al., Mars Orbiter Laser Altimeter: Experiment summary after the first year of global mapping of Mars, *Journal of Geophysical Research*, *106*, 23,689–23,722, 2001b.

Snyder, J. P., Map Projections — A Working Manual, 1987, U.S. Geological Survey Professional Paper 1395.

Squyres, S. W., The evolution of dust deposits in the Martian north polar region, *Icarus*, *40*, 244–261, 1979.

Tanaka, K. L., and E. J. Kolb, Geologic history of the polar regions of Mars based on Mars Global Surveyor Data. I. Noachian and hesperian periods, *Icarus*, *154*, 3–21, 2001.

Tanaka, K. L., and D. Scott, Geologic Map of the Polar Regions of Mars, 1987, U.S. Geol. Surv. Misc. Invest. Ser., Map I-1802-C.

Thomas, P., Present wind activity on Mars - Relation to large latitudinally zoned sediment deposits, *Journal of Geophysical Research*, *87*, 9999–10,008, 1982.

Thomas, P., and C. Weitz, Sand dune materials and polar layered deposits on Mars, *Icarus*, *81*, 185–215, 1989.

Thomas, P. C., and P. J. Gierasch, Polar margin dunes and winds on Mars, *Journal of Geophysical Research*, *100*, 5397–5406, 1995.

Thomas, P. C., S. W. Squyres, K. E. Herkenhoff, A. Howard, and B. C. Murray, Polar deposits of Mars, in *Mars*, edited by H. H. Kieffer, B. M. Jakosky, C. W. Snyder, and M. S. Matthews, pp. 767–795, Univ. of Arizona Press, 1992.

Thomas, P. C., et al., North-south geological differences between the residual polar caps on Mars, *Nature*, *404*, 161–164, 2000.

Toon, O. B., J. B. Pollack, W. Ward, J. A. Burns, and K. Bilski, The astronomical theory of climatic change on Mars, *Icarus*, *44*, 552–607, 1980.

Touma, J., and J. Wisdom, The chaotic obliquity of Mars, *Science*, *259*, 1294–1297, 1993.

Tsoar, H., R. Greeley, and A. R. Peterfreund, Mars - The north polar sand sea and related wind patterns, *Journal of Geophysical Research*, *84*, 8167–8180, 1979.

Tyler, G. L., G. Balmino, D. P. Hinson, W. L. Sjogren, D. E. Smith, R. A. Simpson, S. W. Asmar, P. Priest, and J. D. Twicken, Radio science observations with Mars Global Surveyor: Orbit insertion through one Mars year in mapping orbit, *Journal of Geophysical Research*, *106*, 23,327–23,348, 2001.

Vasavada, A. R., D. A. Paige, and S. E. Wood, Near-surface temperatures on Mercury and the Moon and the stability of polar ice deposits, *Icarus*, *141*, 179–193, 1999.

Vasavada, A. R., J. Williams, D. A. Paige, K. E. Herkenhoff, N. T. Bridges, R. Greeley, B. C. Murray, D. S. Bass, and K. S. McBride, Surface properties of Mars' polar layered deposits and polar landing sites, *Journal of Geophysical Research*, *105*, 6961–6970, 2000.

Ward, A. W., and K. B. Doyle, Speculation on Martian north polar wind circulation and the resultant orientations of polar sand dunes, *Icarus*, *55*, 420–431, 1983.

Ward, W. R., Large-scale variations in obliquity of Mars, *Science*, *181*, 260–262, 1973.

Ward, W. R., and D. J. Rudy, Resonant obliquity of Mars?, *Icarus*, *94*, 160–164, 1991.

Wessel, P., and W. H. F. Smith, New improved version of generic mapping tools released, *Eos Trans. AGU*, *79*, 579, 1998.

Zuber, M. T., D. E. Smith, S. C. Solomon, D. O. Muhleman, J. W. Head, J. B. Garvin, J. B. Abshire, and J. L. Bufton, The Mars Observer laser altimeter investigation, *Journal of Geophysical Research*, *97*, 7781–7797, 1992.

Zuber, M. T., et al., Observations of the north polar region of Mars from the Mars Orbiter Laser Altimeter, *Science*, *282*, 2053–2060, 1998.